Ph.D. Dissertation

Doctoral Program in Korea Maritime and Ocean University

Time-optimal trajectory and robust adaptive control for hybrid underwater glider

하이브리드 수중 글라이더 시스템의 최적시간 궤적 및 강인 적응 제어

Ngoc-Duc Nguyen

Supervisor: Prof. Hyeung-Sik Choi

Department of Mechanical Engineering

Graduate School of Korea Maritime and Ocean University

August 2019

본 논문을 NGOC-DUC NGUYEN 의 공학박사 학위논문으로 인준함.

위원장: 공학박사 유삼상 (인)

위 원: 공학박사 최형식 (인)

위 원: 공학박사 김준영 (인)

위 원: 공학박사 이성욱 (인)

위 원: 공학박사 조용성 (인)

2019 년 07 월

한국해양대학교 대학원

Time-optimal trajectory and robust adaptive control for hybrid underwater glider system

Ngoc-Duc Nguyen

Department of Mechanical Engineering

Graduate School of Korea Maritime and Ocean University

Abstract

The undersea environment is generally still a mystery for the human race, although it has been with us for a long time. To explore under the sea, the underwater glider is the efficient equipment capable of sustainable operation for several months. For faster and longer duration performance, a new design of underwater glider (UG) shaping ray type is proposed. To have the shortest settling time, a new design of time-optimal trajectory (TOT) for controlling the states of the ray-type hybrid underwater glider (RHUG) is proposed. And for the stable flight control, a robust adaptive controller is designed for the RHUG with unknown parameters and environmental disturbances.

The heading dynamics of the RHUG is presented with linear and quadratic damping. A closed form solution of the heading dynamics is realized for designing the time-optimal trajectory. The conventional and super-twisting sliding mode control will be constructed for tracking this trajectory. The tracking performance considering the disturbance effect will be discussed in simulations. For identification of unknown parameters of the system, the adaptive control is designed and implemented by the heading experiment.

The RHUG uses the net buoyancy force for gliding under the water, so the depth control is essential. In this dissertation, a robust control algorithm with TOT will be carried out for the heaving motion using a hybrid actuation of the buoyancy engine and the propeller. The net buoyancy force with a constant rate is generated by the buoyancy engine for both descending and ascending motion. And the second actuator for the depth control is the propeller with quick response in producing thrusting force. To apply the robust control with TOT, the control input is designed for the buoyancy engine and thruster individually. And finally, the robust control with TOT using the buoyancy engine and thruster is simulated with consideration of external disturbances.

When the RHUG is the underactuated system, a robust adaptive control is designed for the RHUG dynamics based on Lyapunov's direct method using the backstepping and sliding mode control techniques. The performance of this controller is simulated for gliding motion and depth control with unknown parameters and bounded disturbances.

KEYWORDS: time-optimal trajectory, robust adaptive control, hybrid underwater glider, backstepping, sliding mode control

Contents

List of Tables

List of Figures

Chapter 1. Introduction

1.1. Hybrid underwater glider

Our current ocean data is not enough for humankind to understand the main resource of the world. It might be true to say that people understand other planets better than their own ocean. Due to the lack of equipment for monitoring the ocean, scientists cannot access all of the ocean information. And it is dangerous for divers to collect the data under the sea. Nowadays, there are many underwater vehicles developed for collecting the information of the most nutritious resource, the blue ocean, for maintaining the development of the human race on earth. Among many kinds of underwater vehicles, the hybrid underwater glider is the most useful method to collect the ocean data efficiently. This vehicle uses its net buoyancy force for gliding under the water. This vertical force can be converted to the horizontal motion thanks to its wings or body shape. Also, some propellers can be used to help them quickly coordinate to other positions or avoid collisions or obstacles. The net buoyancy force can be produced by the buoyancy engine with very small energy. Therefore, the hybrid underwater glider can stay in the sea for many months to observe the ocean. If there are the numerous fleets of underwater gliders to work on our ocean, there is no doubt that our knowledge about the resource underneath the sea surface will increase dramatically.

Over two decades of development, the underwater glider (UG) has become popular and reliable for oceanographic activities due to its low-cost and

enduring operation. However, to use it in the strong current region, it is obvious that the UG needs stronger actuation such as propellers. And in the case of depth control, the steady state error and non-zero pitch angle are major barriers for the UG to track the desired depth. The reason for this phenomenon is explained by the inaccurate trim and ballasting condition in [1]. Therefore, to overcome those problems, the hybrid underwater glider (HUG) is an alternative method for the mission of depth control with strong disturbances.

The first commercial gliders were developed and named SLOCUM in [2] after Joshua Slocum, the first man to travel around the world alone, and Spray in [3] after the boat Joshua Slocum used to sail around the globe. These UGs can glide with 0.2-0.3m/s speed and cover the range of 6,000km and 40,000km for Spray and SLOCUM (thermal buoyancy propulsion version) respectively. With outstanding performance in the sea trials, there were many studies of this system, and many improvements were carried out in various aspects of modeling, control design, navigation, and guidance. The general studies of components inside the UG with comprehensive results were reported in [4]. The underwater acoustic glider is presented in [5] with the acoustic sensor for the anti-submarine and mine-countermeasure warfare. The new power system was designed in [6] and experimentally proved that the heat quality was improved for the thermal UG system. The low-cost and light-weight UG was described named Fòlaga in [7] for the coastal oceanographic mission. Another application of the virtual mooring system using a UG was proposed in [8]. The miniature UG called ALEX was developed in [9] to realize the high-performance maneuverability, and its motion simulations in diving motion corresponded well with the data from the experiment tank. In [10], it presented the development of the shallow

water UG and the system identification, which was used to obtain the control system model. The low-power propeller system was integrated into the 200m SLOCUM electric glider in [11] to perform the horizontal flight and increase the overall speed of the previous glider. To improve the flight control, the numerical study of hydrodynamic behavior and the flight mechanics was carried out in [12]. In [13], details of the mechanical and electric design of a coastal UG were discussed for testing planning algorithms and control development. The report of the first successful autonomous mission of a 177km journey was shown in [14] using Littoral Glider from Alaska Native Technology LLC. In [15], the Newtonian approach was used to model a hybrid-driven glider, and the hydrodynamics were estimated using Strip theory and the CFD method. In [16] and [17], the design of a hybrid underwater glider called ZJU-HUG was presented with a rotatable thruster for an underwater docking mission. In [18], the effect of different wing layout to hydrodynamics performance of a hybrid underwater glider was analyzed using the design of experiments and CFD method. An adaptive identification method for online identification of UG was developed in [19]. A new buoyancy engine design with the combination of compressed air and liquid fluid to increase gliding speed of UGs was presented in [20]. A small civilian UG with a high lift to drag ratio and hydrodynamic optimization was studied in [21]. In [22], the high-speed underwater glider with 2.5knots gliding speed was developed with a battery mass-shifter for pitching and yawing control. The subsea payload delivery for underwater constructions using UGs was presented, and the hydrodynamic effect of two types of wings was analyzed in [23]. In [24], a design of controllable wings for hybrid underwater glider was presented to improve the underwater flight performance. An open-source highly maneuverable and low-cost miniature UG was developed and showed the small turning radius in [25]. The mathematical model of UG using the

N4SID identification method was studied in [26] and [27]. In [28], an application of Takagi-Sugeno fuzzy logic modeling for UG to reduce the computational effort was implemented. The design of coastal UG was presented, and the study of the most important parameters to design the variable buoyancy system was carried out in [29].

In this dissertation, a new hull design of ray-type hybrid underwater glider (RHUG) will be presented with the stingray shape. With this new design, the space for sensor payloads and batteries is increased dramatically. And, to increase the net buoyancy force, a new design of dual-buoyancy engine is presented.

1.2. Time-optimal trajectory

Every system has a certain limit of control inputs such as the maximum thrust in the propellers or the maximum net buoyancy force in the buoyancy engines. Based on these constraints, the time-optimal trajectory can be formulated for underwater vehicles. In [30], the singular extremals of the underwater vehicle system for the time-optimal problem was studied. And later, the design of a time-efficient trajectory with constant thrust arcs was developed and successfully implemented into the underwater vehicle in [31]. But with this algorithm, considerable computational time was seen in the practical implementation. In [32], a numerical method for minimum time heading control for UG was presented in the known and time-varying flow fields. The closed-form solution for time-optimal trajectory was developed in [33] for the depth dynamic of the underwater vehicle using propeller propulsion.

In this dissertation, a novel time-optimal trajectory will be presented for the heading dynamic of the RHUG system. Also, the time-optimal trajectory will

be studied for the depth control using the buoyancy-driven propulsion in the RHUG system. And then, the experiment of the TOT concept for heading control will be carried out using thrusters.

1.3. Nonlinear control design

The underwater glider system is a highly nonlinear system with many uncertainties from inaccurate parameters and environmental disturbances. Thus, the development of an advanced controller to be robust to the parametric uncertainties and external disturbances is necessary. In [34], to derive the nonlinear control laws for the moving mass actuator, the stability of a steady underwater vehicle motion using potential shaping feedback was studied. A nonlinear robust adaptive control was developed in [35] for an under-actuated ship to follow the desired path in spite of external disturbances. In [36], a nonlinear robust adaptive control was designed for a 6-DOF model of AUVs with only four actuators to follow the pre-defined path at the desired speed despite external disturbances. A Lyapunov candidate was proposed in [37] to prove the stability of steady gliding motion of hydrodynamic force such as the UG system. In [38], a robust nonlinear controller was proposed to asymptotically drive the AUV dynamic onto the desired path at a constant forward speed. In [39], a predictive controller was developed for attitude control of SLOCUM glider. The pitch control performance of a UG was validated in [40] by a towing tank and sea test. The simulation results of nonlinear adaptive control with the actuator saturation and parametric uncertainties for 6DOF AUV model was developed in [41]. An adaptive fuzzy controller for heading control of a UG was simulated in [42]. The heading control experiment of a UG for virtual mooring application was presented in [43]. A study of a model predictive control to compensate for the drift of UG due to external disturbance was developed in [44]. In [45],

a pitching control experiment was conducted using phase-lead compensator resulting in the improvement in the pitch performance. An energy optimal depth controller design for long-range HUG was studied and experimentally tested in [46]. In [47], backstepping integral sliding mode control was developed and showed many merits in the reduction of chattering problem, steady-state error, and control effort. A super-twisting sliding mode control was presented in [48] and provided chattering-free performance under the existence of disturbances. A new approach for pitch control was studied in [49] using model compensation based on the active disturbance rejection control (ADRC). And a self-searching optimal ADRC for pitch control was proposed in [50] with good adaptive performance and energy-efficient control effort. In [51], the combination of reinforcement learning and ADRC was proposed and provided high-precision and high-adaptive control ability in simulation results. An adaptive fuzzy incremental PID and an anti-windup compensator were presented in [52] with the verification on the Petrel-II 200 glider in the sea trials.

In this dissertation, a robust adaptive control using back-stepping technique is designed for a hybrid underwater glider in a vertical plane with the presence of disturbances induced by ocean currents and waves. The internal moving mass is considered as the first control input with the provided mass-shifter model. And thruster force is another output of this controller for keeping the constant speed in the cruise mode. Saw-tooth gliding motion and depth control is simulated using the developed platform parameters. In this HUG system, there are two inputs for controlling the vertical dynamics. Thus, this system is the under-actuated system with two inputs in the 3-DOF model. Therefore, this finding is different from other controllers above, and it has

reliable performance. The proof of dynamics stability will be given using Lyapunov's direct method.

The following contents will be organized as below.

Chapter 2: The 6-DOF dynamics of the hybrid underwater glider will be presented, and all control inputs are modeled using the developed platform design.

Chapter 3: The time-optimal trajectory design for heading dynamics will be formulated, and the combination between TOT trajectory and two different nonlinear robust controllers will be presented.

Chapter 4: The TOT trajectory is also formulated for the application of depth control using buoyancy engines and thrusters for the HUG system. A closed-form solution for the heave dynamics will be showed and validated by computer simulation.

Chapter 5: An implementation of adaptive control for heading dynamics with TOT trajectory will be presented.

Chapter 6: A robust adaptive control for the vertical plane of HUG will be organized here. All control design processes will be discussed and proved in this chapter. And simulation results of gliding motion and depth control will be presented.

Chapter 7: The novelty of this thesis will be emphasized here.

Chapter 2. Dynamics of RHUG

2.1 Dynamics of underwater vehicles

The 6-DOF equations of motion of a fully submerged underwater vehicle, whose body axes coincide with the principal axes of inertia, can be written as Eq. (1) as presented in [53].

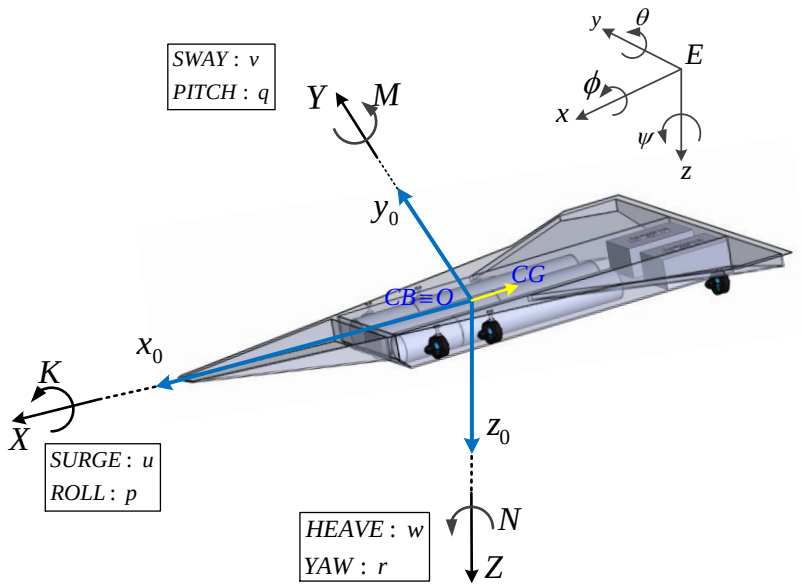

Fig. 1 Coordinate system of Ray-type hybrid underwater glider

$$\begin{aligned} \dot{\eta} &= Jv \\ M\dot{v}+C(v)v+D(v)v+g(\eta) &= \tau+\tau_e \end{aligned} \tag{1}$$

where $\eta = [x\ y\ z\ \phi\ \theta\ \psi]^T$ is the position and orientation of the vehicle in inertial frame $Exyz$ in Fig. 1; $v = [u\ v\ w\ p\ q\ r\ ]^T$ is the translation and

angular velocity in body-fixed frame $Ox_0y_0z_0$ in Fig. 1; $M = M_{RB} + M_A$ is the inertia matrix; M_{RB} is the rigid body inertia matrix; M_A is the added mass inertia matrix ; $C(\nu) = C_{RB}(\nu) + C_A(\nu)$ is the Coriolis and centripetal matrix; C_{RB} is the rigid body Coriolis and centripetal matrix; C_A is the hydrodynamic Coriolis and centripetal matrix; $D(\nu)$ is hydrodynamic damping matrix; $g(\eta)$ is the gravitational matrix; τ is the control input; τ_e is the disturbance forces and moments from ocean currents and waves.

For the detailed system, the motion equation of 6-DOF dynamics can be shown as Eq. (2) as presented in [53].

$$\begin{aligned}
&m\left[\dot{u} - vr + wq - x_g(q^2 + r^2) + y_g(pq - \dot{r}) + z_g(pr + \dot{q})\right] = X \\
&m\left[\dot{v} - wp + ur - y_g(r^2 + p^2) + z_g(qr - \dot{p}) + x_g(qp + \dot{r})\right] = Y \\
&m\left[\dot{w} - wq + vp - z_g(p^2 + q^2) + x_g(rp - \dot{q}) + y_g(rq + \dot{p})\right] = Z \\
&I_x\dot{p} + \left(I_z - I_y\right)qr + m[y_g(\dot{w} - uq + vp) - z_g(\dot{v} - wp + ur)] = K \\
&I_y\dot{q} + (I_x - I_z)rp + m[z_g(\dot{u} - vr + wq) - x_g(\dot{w} - uq + vp)] = M \\
&I_z\dot{r} + \left(I_y - I_x\right)pq + m[x_g(\dot{v} - wp + ur) - y_g(\dot{u} - vr + wq)] = N
\end{aligned} \tag{2}$$

Here, u, v, w are linear velocities of origin O in the body-fixed frame; p, q, r are angular velocity in the body-fixed frame; ϕ, θ, ψ are Euler angles in the earth-fixed frame; x_g, y_g, z_g are the position of the center of gravity (CG in Fig. 1) in the moving frame $Ox_0y_0z_0$; X, Y, Z are the forces acting on the vehicle in the body-fixed frame; K, M, N are the moments acting on the vehicle in the body-fixed frame. And the kinematic system can be driven by Euler angles through the Jacobian matrix in (3).

$$
\begin{aligned}
\dot{x} &= uc\psi c\theta + v(c\psi s\theta s\phi - s\psi c\phi) + w(s\psi s\phi + c\psi c\phi s\theta) \\
\dot{y} &= us\psi c\theta + v(c\psi c\phi - s\phi s\theta s\psi) + w(s\theta s\psi c\phi - c\psi s\phi) \\
\dot{z} &= -us\theta + vc\theta s\phi + wc\theta c\phi \\
\dot{\phi} &= p + qs\phi t\theta + rc\phi t\theta \\
\dot{\theta} &= qc\phi - rs\phi \\
\dot{\psi} &= q\frac{s\phi}{c\theta} + r\frac{c\phi}{c\theta}
\end{aligned}
\tag{3}
$$

where $ci \coloneqq \cos(i)$; $si \coloneqq \sin(i)$; $ti \coloneqq \tan(i)$.

The external force and moment vector contains three components as described here, $[X, Y, Z, K, M, N]^T = \tau_H + \tau + \tau_e$. The hydrodynamics forces and moments, τ_H, can be estimates as (4) using Eq. (2.114) in [53]. The control input τ is generated by thrusters, moving mass and buoyancy engines. Finally, the environmental input τ_e is the disturbances from ocean currents and waves which can be formulated by the sinusoid function.

$$\tau_H = -M_A\dot{\nu} - C_A(\nu)\nu - D(\nu)\nu - g(\eta) \tag{4}$$

For underwater vehicle application, the added mass matrix M_A and hydrodynamic Coriolis and centripetal matrix C_A can be described by using Eq. (2.129) and (2.130) in [53] as Eq. (5) and (6).

$$M_A = -diag\{X_{\dot{u}}, Y_{\dot{v}}, Z_{\dot{w}}, K_{\dot{p}}, M_{\dot{q}}, N_{\dot{r}}\} \tag{5}$$

$$C_A = \begin{bmatrix} 0 & 0 & 0 & 0 & -Z_{\dot{w}}w & Y_{\dot{v}}v \\ 0 & 0 & 0 & Z_{\dot{w}}w & 0 & -X_{\dot{u}}u \\ 0 & 0 & 0 & -Y_{\dot{v}}v & X_{\dot{u}}u & 0 \\ 0 & -Z_{\dot{w}}w & Y_{\dot{v}}v & 0 & -N_{\dot{r}}r & M_{\dot{q}}q \\ Z_{\dot{w}}w & 0 & -X_{\dot{u}}u & N_{\dot{r}}r & 0 & -K_{\dot{p}}p \\ -Y_{\dot{v}}v & X_{\dot{u}}u & 0 & -M_{\dot{q}}q & K_{\dot{p}}p & 0 \end{bmatrix} \quad (6)$$

The hydrodynamic damping matrix $D(v)$ is estimated by neglecting the high-order terms. Therefore, this matrix can be formulated by the linear and quadratic form as (7).

$$\begin{aligned} D(v) = &-diag\{X_u, Y_v, Z_w, K_p, M_q, N_r\} \\ &-diag\{X_{u|u|}|u|, Y_{v|v|}|v|, Z_{w|w|}|w|, K_{p|p|}|p|, M_{q|q|}|q|, N_{r|r|}|r|\} \end{aligned} \quad (7)$$

The restoring force and moment matrix $g(\eta)$ can be illustrated by Eq. (2.168) in [53] as shown in (8).

$$g(\eta) = \begin{bmatrix} (W-B)s\theta \\ -(W-B)c\theta s\phi \\ -(W-B)c\theta c\phi \\ -(y_gW - y_bB)c\theta c\phi + (z_gW - z_bB)c\theta s\phi \\ (z_gW - z_bB)s\theta + (x_gW - x_bB)c\theta c\phi \\ -(x_gW - x_bB)c\theta s\phi - (y_gW - y_bB)s\theta \end{bmatrix} \quad (8)$$

2.2 Design of RHUG platform

2.2.1 Hull design

The hull of RHUG contains four shells and one sheet, as shown in Fig. 2. The sheet has a thickness of 10mm and supports the whole system. The other four shells have a thickness of 5mm. The hardware container is used to support three-cylinder hulls and batteries. And three shells of buoyancy foam

will be installed at the nose and the wings of the vehicle as Fig. 2. The final design of the hull is manufactured and weighted, as shown in Fig. 3.

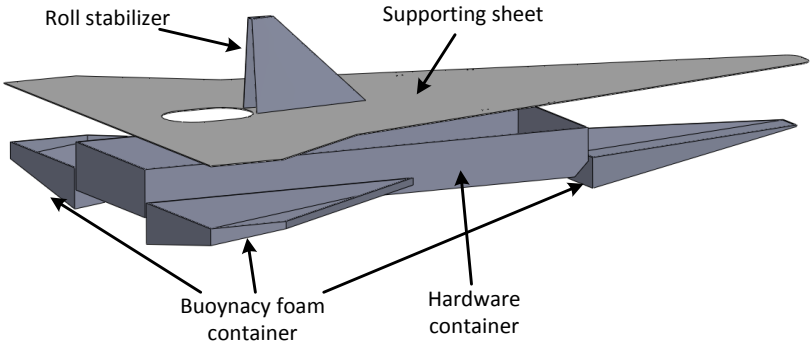

Fig. 2 Design of the hull structure

(a) Front view

(b) Back view

(c) Top view

(d) Side view

Fig. 3 The final version of the hull design

2.2.2 Buoyancy engine and mass-shifter

Inside the hardware container in Fig. 2, there are three cylinders and one battery. In Fig. 4, the middle hull contains a mass-shifter and the control system. In the mass-shifter mechanism, the position of the moving mass is controlled by the DC motor. Two hulls on the side are the buoyancy engines and are distinguished by the left buoyancy engine and the right buoyancy

engine. The piston position can be controlled by the BLDC motor, as shown in Fig. 4. The three hulls and battery are connected by three SubConn cables for waterproof purpose.

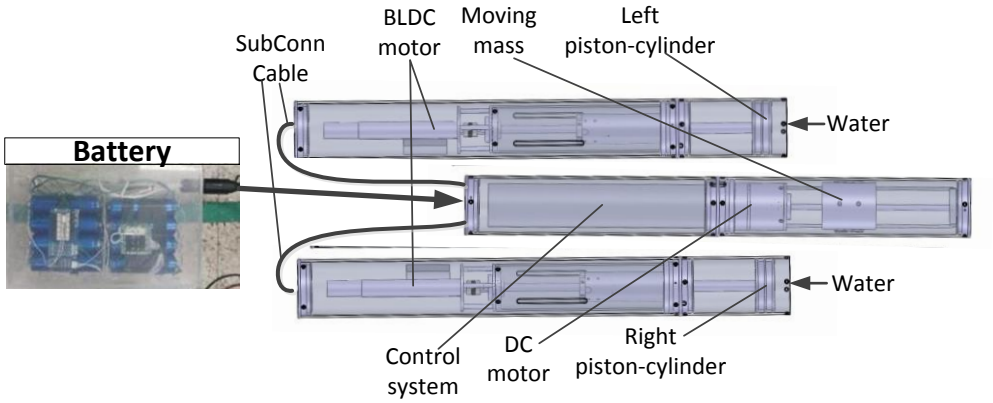

Fig. 4 Buoyancy engine and mass-shifter design

2.2.3 Battery

One pack of batteries has 16 cells contained in the acrylic box in Fig. 5. There are two boards of protection circuit management (PCM) for safety discharging and recharging. After checking the function of the battery, the acrylic box will be filled with the Epoxy liquid for waterproof protection.

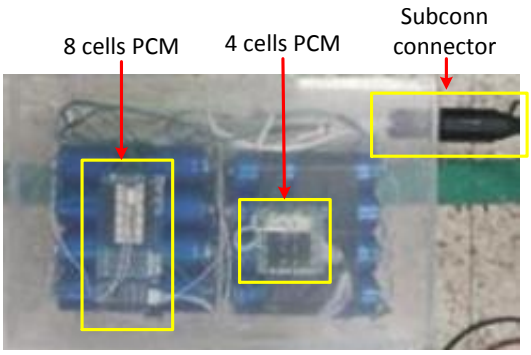

Fig. 5 Battery design

2.2.4 Sensors

For gliding and depth control, RHUG should have at least the depth measurement, earth-fixed orientations, heading angle, body-fixed accelerations, body-fixed angular rates and earth-fixed positions in the sea surface. So the three sensors below will be essential for controlling RHUG.

2.2.4.1 Pressure sensor

The pressure range of the depth sensor is chosen from 0 bar to 10 bar (up to 100m) and shown in Fig. 6. This pressure sensor is an analog type, so it has no communication noise. And the frequency of this sensor is depended on the frequency of the analog module of the microcontroller unit (MCU). And in this project, the frequency of reading the depth sensor is set at 100Hz. The error of this depth sensor at the reference condition is 0.5% of the span or 0.5m.

Fig. 6 Pressure transmitter ECO-1

2.2.4.2 AHRS

Fig. 7 XSENS MTi IMU

The XSENS inertial measurement unit (IMU) is the attitude and heading reference system. It contains three kinds of sensors such as accelerometers, gyroscopes, and magnetometers for three-dimensional orientations, accelerations, turning rates, and magnetic field. In this platform, XSENS MTi will be used for orientations, angular rates, and accelerations measurement, as shown in Fig. 7. And the main feature of this AHRS is organized in Table 1.

Table 1 Attitude and heading characteristics of XSENS IMU

Parameter	Value
Static accuracy (roll/pitch)	<0.5 deg
Static accuracy (heading)	<1 deg
Dynamic accuracy	2 deg RMS
Digital interface	RS-232
Dynamic range (pitch)	±90 deg
Dynamic range (roll/heading)	±180 deg
Bias stability (turning rate)	20 deg/h
Bias stability (acceleration)	0.02m/s^2

2.2.4.3 GPS

Fig. 8 ASCEN GPS receiver

The longitude and latitude position of the vehicle will be measured with a GPS sensor, as shown in Fig. 8. And details of this GPS sensor can be seen in Table 2. With this GPS, the position of the vehicle in the form of longitude and latitude will be updated every second. And this low update rate is suitable for RHUG because most of their operating time is under the water and GPS position is required only on the surface for path planning. The operator will use its position for determination of the next desired heading.

Table 2 GPS description

Parameter	Description
GPS solution	MTK MT3339
Position accuracy	3.0m
Velocity accuracy	0.1m/s
Acceleration accuracy	$0.1m/s^2$
Digital interface	UART
Update rate	1Hz
Altitude	Maximum 18,000m
Velocity	Maximum 515m/s
Acceleration	Maximum 4G

2.2.5 Assembly

The main components of the RHUG platform are shown in Fig. 9. This vehicle has two thrusters in the starboard and two thrusters in the stern of the platform. There are three pressure hulls inside the platform. The hulls on the side are buoyancy engines, called a dual-buoyancy engine located on the left and right side, as shown in Fig. 9. The center hull contains the mass-shifter and control system. And the design can carry two packs of battery with the size of 300x200x150mm.

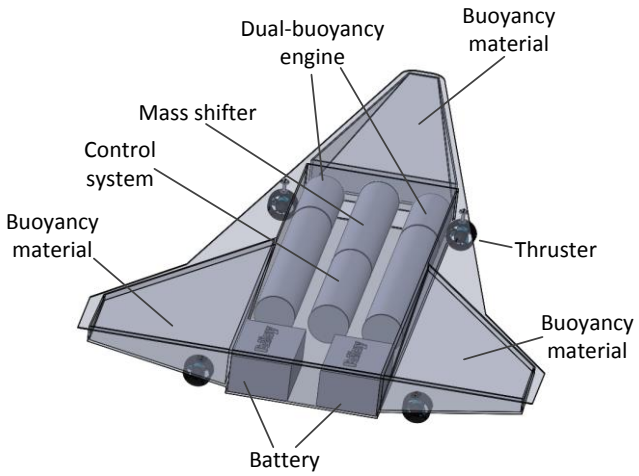

Fig. 9 System configuration

2.3 Dynamics of RHUG

In this design of RHUG as described above, the sway and roll dynamics do not have any actuators. For now, the stability of the roll motion is dependent on the vertical passive stabilizer in Fig. 2, because the main goal of this design is for proving the operation of the gliding motion with the new hull design. Therefore, the sway and roll dynamics will be neglected in this RHUG modeling. And the whole dynamics of underwater vehicles are adapted for the RHUG by dividing it into two dynamics. The first dynamics are surge-heave-pitch motion or vertical dynamics in Exz. And the second dynamics is yaw motion, which is used for heading control, as shown in Fig. 10. The reason for this separation is that the coupling terms between surge, heave and pitch motions cannot be neglected in the gliding motion of RHUG. And another reason is that the hydrodynamic coefficients could be found easily in surge-heave-pitch dynamics through the simple vertical drift test in CFD simulation. Therefore, the dynamics of RHUG will be presented in terms of vertical motion and heading motion individually.

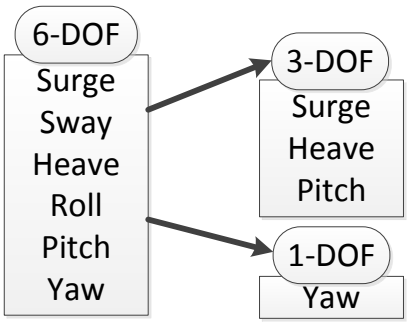

Fig. 10 Modeling concept

By reducing the 6-DOF dynamics system, the vertical system, which is important for gliding motion, will be described in (9).

$$
\begin{aligned}
\dot{x} &= u\cos\theta + w\sin\theta \\
\dot{z} &= -u\sin\theta + w\cos\theta \\
\dot{\theta} &= q \\
(m - X_{\dot{u}})\dot{u} &= -mz_g\dot{q} + mx_g q^2 - mwq + Z_{\dot{w}}wq + X_{uu}u^2 + X_{ww}w^2 \\
&\quad + X_{uw}uw - (W - B)\sin\theta + \tau_w\sin\theta + \tau_u + \tau_{eu} \\
(m - Z_{\dot{w}})\dot{w} &= \left(mx_g + Z_{\dot{q}}\right)\dot{q} + mz_g q^2 + muq - X_{\dot{u}}uq + Z_{uu}u^2 \\
&\quad + Z_{uw}uw + Z_{ww}w^2 + Z_{www}w^3 + (W - B)\cos\theta \\
&\quad + \tau_w\cos\theta + \tau_{ew} \\
\left(I_{yy} - M_{\dot{q}}\right)\dot{q} &= -mz_g\dot{u} + \left(mx_g - M_{\dot{w}}\right)\dot{w} - mz_g qw - Z_{\dot{w}}wu \\
&\quad - Z_{\dot{q}}qu + X_{\dot{u}}uw + M_{uu}u^2 + M_{uw}uw + M_{ww}w^2 \\
&\quad + M_{www}w^3 - \left(z_g W - z_b B\right)\sin\theta - \left(x_g - x_b B\right)\cos\theta \\
&\quad + \tau_q + \tau_{eq}
\end{aligned}
\tag{9}
$$

Here, $X_{\dot{u}}$, $Z_{\dot{w}}$, $Z_{\dot{q}}$, $M_{\dot{w}}$ and $M_{\dot{q}}$ are the added mass coefficients; X_{uu}, X_{uw}, X_{ww} are the hydrodynamic coefficients in the surge dynamics; Z_{uu}, Z_{uw}, Z_{ww}, Z_{www} are the hydrodynamic coefficients in the heaving motion; M_{uu}, M_{uw}, M_{ww}, M_{www} are the hydrodynamic coefficients in the pitching motion; W and B are the weight and buoyancy force in the neutral buoyancy condition; x_g and z_g are coordinates of gravity center in the body-fixed frame; x_b and z_b are coordinates of buoyancy center in the body-fixed frame; m and I_{yy} are the vehicle mass and the y-axis moment of inertia; τ_w is the net buoyancy force from the buoyancy engine; τ_q is the control moment from the mass-shifter; τ_u is the thruster force; τ_{eu}, τ_{ew} and τ_{eq} are the environmental force and moments in the body-fixed frame. Therefore, there are only two control inputs which are τ_u for speed control and τ_q for pitch control.

The heading dynamics is essential for any underwater vehicles, especially underwater gliders. This dynamics will be used to design the heading controller. In this design, there are four thrusters for heading control. The heading dynamics of RHUG can be decoupled from 6-DOF dynamics by neglecting other states, as shown in Eq. (10). Here, $N_{\dot{r}}$ is the added mass coefficient; N_r is the linear damping coefficient; $N_{|r|r}$ is the quadratic damping coefficient; τ_r is the moment produced by four thrusters; d is the external disturbance.

$$\begin{gathered} \dot{\psi} = r \\ (I_{zz} - N_{\dot{r}})\dot{r} = N_r r + N_{|r|r}|r|r + \tau_r + d \end{gathered} \tag{10}$$

2.4 Hydrodynamic coefficients

The planar motion mechanism (PMM) test for the hydrodynamic coefficients is very expensive. Therefore, to obtain the hydrodynamic coefficients of this new hull design, the result of the CFD method is presented.

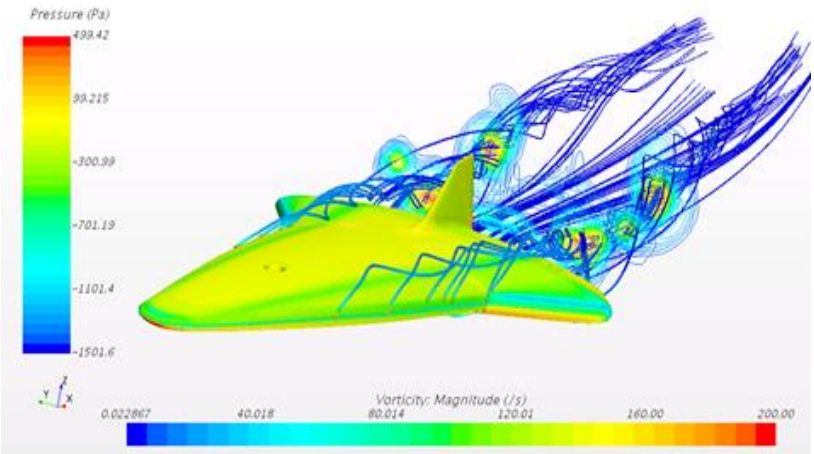

Fig. 11 Vertical static drift test for varying pitch angle

The vertical drift test of the RHUG hull at different pitch angle range from $-15°$ to $15°$ is performed in Fig. 11 and the resistant forces in X and Z axes through the CFD analysis are shown in Fig. 12 and Fig. 13, respectively.

The color spectrum of the RHUG hull surface represents the vertical force acting on the hull. The line contour around the hull is the fluid flow in the vertical drift test. From the CFD simulation, the vortex shedding occurred at the left and right wing ends of the hull. The analytical result of the force acting on the X and Z axes of the body-fixed frame is shown in Fig. 12 and Fig. 13, respectively. And the dimensionless hydrodynamic coefficients from the CFD results are shown in Table 3.

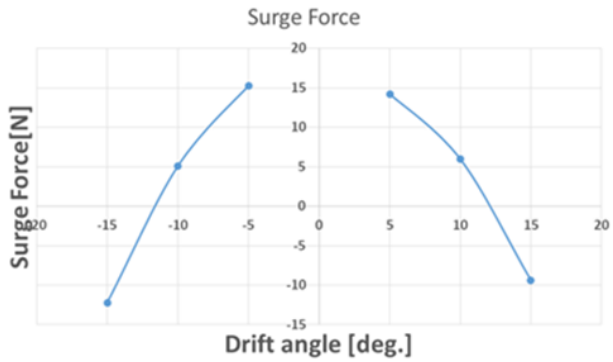

Fig. 12 Vertical static drift calculation result for surge motion

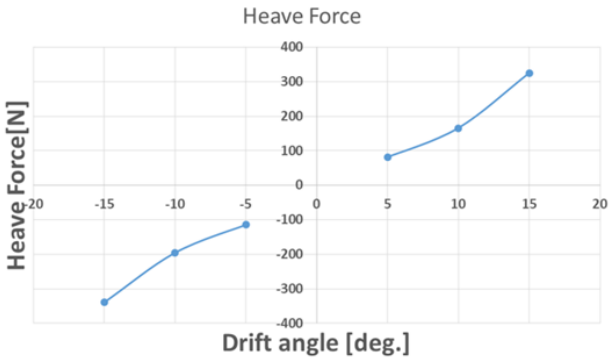

Fig. 13 Vertical static drift calculation result for heave motion

Table 3 Dimensionless hydrodynamics coefficients (CFD method)

Parameter	Value	Parameter	Value	Parameter	Value
$X_{\dot{u}}$	-0.03	$Z_{\dot{w}}$	-0.011836	$M_{\dot{w}}$	-0.022352
X_{uu}	-0.0063	$Z_{\dot{q}}$	-0.004774	$M_{\dot{q}}$	-0.003823
X_{uw}	0.1485	Z_{uu}	-0.0052	M_{uu}	-0.0018
X_{ww}	0.0013	Z_{uw}	-0.3204	M_{uw}	0.0117
		Z_{ww}	0.0356	M_{ww}	-0.0173
		Z_{www}	-1.623	M_{www}	0.6989

2.5 Thruster modeling

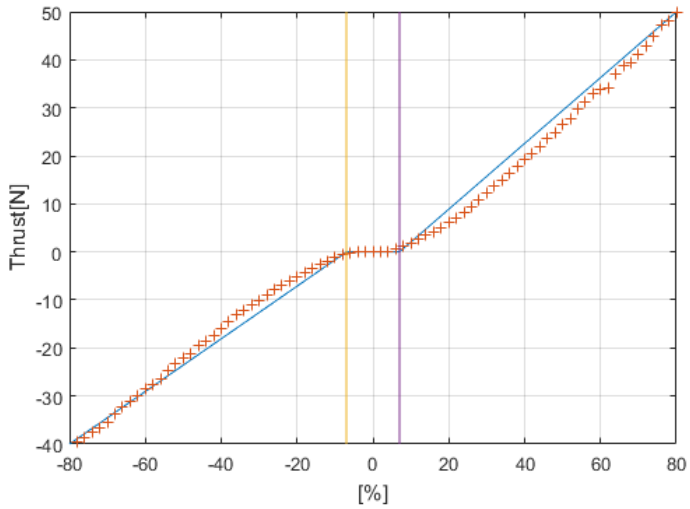

Fig. 14 Thruster force vs. percentage input

$$T_i = \begin{cases} 0.68u_t - 4.795 & 7 < u_t \leq 80 \\ 0.54u_t + 3.836 & -80 \leq u_t < -7 \\ 0 & -7 \leq u_t \leq 7 \end{cases} \quad (11)$$

The thrusters in this platform are T200 thrusters. The experimental data can be obtained from this site https://www.bluerobotics.com/. In Fig. 14, the thrust force τ_u ranges from -40N to 50N with the input signal u_t from -80% to 80%. This relationship can be illustrated as the set of equations in (11). The control force and moment can be calculated from thruster force by Eq.

(12) and (13). Here, τ_u is the surge control input for speed control in the body-fixed frame; τ_r is the yaw moment acting on the vehicle in the body-fixed frame; T_1 and T_2 are the forces of thrusters in the starboard; T_3 and T_4 are the forces of thrusters in the stern; d_1 is the distance of two thrusters in the starboard; d_2 is the distance of two thrusters in the stern.

$$\tau_u = T_1 + T_2 + T_3 + T_4 \tag{12}$$

$$\tau_r = (T_1 + T_2)\frac{d_1}{2} + (T_3 + T_4)\frac{d_2}{2} \tag{13}$$

2.6 Buoyancy engine modeling

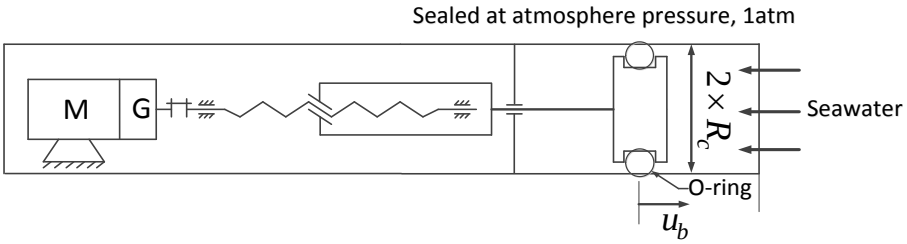

Fig. 15 Buoyancy engine diagram

$$\tau_w = u_b \pi R_c^2 \rho g \tag{14}$$

$$x_b = \frac{\pi R_c^2 u_b (X_p + \frac{u_b}{2})}{\pi R_c^2 u_b + V_{nb}} \tag{15}$$

In this RHUG system, the buoyancy engine will let the water in or out by moving a piston along the cylinder, as shown in Fig. 15. During this process, the volume of air in this vehicle will decrease or increase depending on the position of the piston. If the weight and buoyancy forces are equal in the neutral condition, this glider can sink when its volume is reduced and float toward the water surface when it increases its volume. To specify the force

that this buoyancy engine can produce, the length of the piston travel and the radius of the cylinder should be defined. Then, the net buoyancy force is equal to the seawater weight of the compressed air volume, and it is shown in (14). Here, in Fig. 15, u_b is the position of the piston; R_c is the radius of the cylinder; ρ is the density of seawater; g is the gravitational acceleration. During the operation of the buoyancy engine, the center of buoyancy is shifted along the Ox_0 axis by Eq. (15). Here, X_p is the position of pistion in the neutral position along the Ox_0 axis in the body-fixed frame; V_{nb} is the volume of the vehicle in the neutral condition of the buoyancy engine.

2.7 Mass-shifter modeling

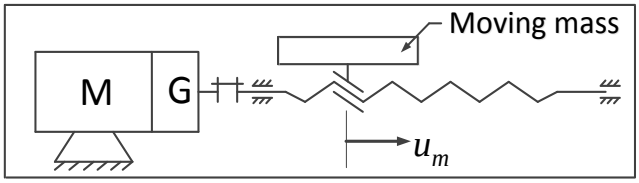

Fig. 16 Mass shifter diagram

$$x_g = \frac{m_{stat}x_{stat} + m_m u_m}{m} \approx \frac{m_m}{m} u_m \tag{16}$$

$$\tau_q = W x_g \approx W \frac{m_m}{m} u_m \tag{17}$$

$$I_{yy} = I_{ny} + m_m u_m^2 sgn(u_m) \tag{18}$$

The movable mass in Fig. 16 can be translated along the Ox_0 axis so the center of gravity in this axis x_g can be defined as (16). Here, $m_{stat} = m - m_m$ is the static mass; m_m is the weight of the movable mass; u_m is the position of the moving mass; x_{stat} is the position of the static mass and it is

assumed to be very small because the fact is that the origin of the body-fixed frame is located near to the center of gravity. Then, x_g can be replaced by $\frac{m_m}{m} u_m$ in (17). The moment produced by the mass-shifter can be computed by the product of the net buoyancy force and the location of the center of gravity in the Ox_0 axis, as shown in (17). In addition, the moment of inertia is also changed due to the translation of moving mass following to (18). Here, I_{ny} is the moment of inertia about the Oy_0 axis in the neutral condition of moving mass.

Chapter 3. Time-optimal trajectory with actuator saturation for heading control

3.1 Time-optimal trajectory

The performance of underwater vehicles is dependent on the hydrodynamic coefficients and the actuating force with energy limit. The time-optimal trajectory is a set of the desired position, velocity, and acceleration, and it is directly related with the maximum and minimum control input. If the vehicle tracks the TOT trajectory, the shortest arrival time of this motion control will be obtained within the input limit.

3.2 Heading motion

The decoupled yaw dynamics of the underwater glider can be written as Eq. (19).

$$\begin{aligned} \dot{\psi} &= r \\ (I_{zz} - N_{\dot{r}})\dot{r} &= N_r r + N_{|r|r}|r|r + u + d \end{aligned} \tag{19}$$

where r is the yaw rate; ψ is the heading angle; I_{zz} is the moment of inertia about Oz_0 axis; $N_{\dot{r}}$ is the added mass coefficient; N_r and $N_{|r|r}$ are the linear and quadratic damping coefficients respectively; u is the torque of thrusters; and d is the external disturbance induced by currents and waves. And then it can be rewritten in the simpler form as (20). Here, $a = \frac{N_{|r|r}}{I_{zz}-N_{\dot{r}}}$; $b = \frac{N_r}{I_{zz}-N_{\dot{r}}}$; $\alpha = I_{zz} - N_{\dot{r}}$; $c = \frac{u}{\alpha}$; $d_h = \frac{d}{\alpha}$.

For the time-optimal problem, the disturbance is not used for designing TOT trajectory and then Eq. (21) is used instead of (20).

$$\dot{r} = ar + b|r|r + c + d_h \tag{20}$$

$$\dot{r} = ar + b|r|r + c \tag{21}$$

3.3 Analytic solution of heading dynamic equation

The concept of the time-optimal trajectory is that if the solution of the given dynamics is formulated as the function of time for the certain control input, then that solution is the output of the dynamics with that control input. So, if the control input is kept at the maximum and minimum value for the acceleration and deceleration time, then the closed-form of time-function of the given dynamics is the fastest trajectory or time-optimal trajectory.

In this application, the heading dynamics is derived in this section. The state of this dynamics or the output of this system is r, the trajectory of this system is r_d. In the RHUG heading dynamic, u is the resulting moment from thrusters, the maximum moment is u_{max} and the minimum moment is u_{min}, as shown in Fig. 17. For the sake of simplicity, the control input u will be addressed through the scaled control input c, the maximum scaled input is $c_1 = \frac{u_{max}}{\alpha}$ and the minimum scaled input is $c_2 = \frac{u_{min}}{\alpha}$.

Here, ψ_0 is the initial value of angle; ψ_3 is the desired value of angle; r_1^* is the maximum angular velocity with the maximum input; t_1^* is the time when the maximum angular velocity is achieved; ψ_1^* is the angle at t_1^*; and $\Delta\psi_3^*$ is the angular distance from t_2 to t_3. With the given desired angle ψ_3 and the initial angle ψ_0, in one heading dynamics, other parameters of the TOT trajectory will be solved in the following.

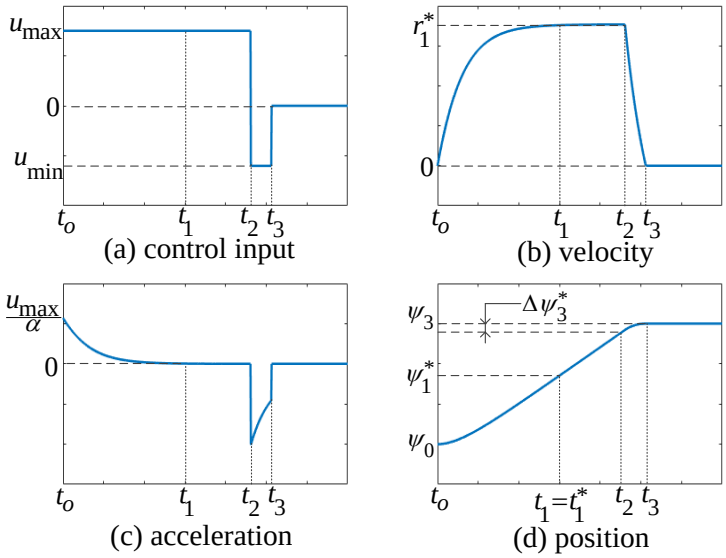

Fig. 17 Time-optimal trajectory profile

The TOT trajectory will be divided into three segments as acceleration from t_0 to t_1, constant velocity from t_1 to t_2, and deceleration from t_2 to t_3, as shown in Fig. 17. From t_0 to t_1, the vehicle will be controlled using the maximum moment of u_{max} and it will derive the yaw rate to the critical value r_1^*. Due to the growth of hydrodynamic moment, the acceleration will decrease to zero and the angular velocity will be constant from t_1 to t_2 in Fig. 17. When the gap between the desired angle and the actual angle is equal to $\Delta\psi_3^*$, the minimum input will be applied to bring both velocity and acceleration to zero. Therefore, once the parameters of heading dynamics are known, this trajectory can be used to maneuver the heading angle with minimum time consumption.

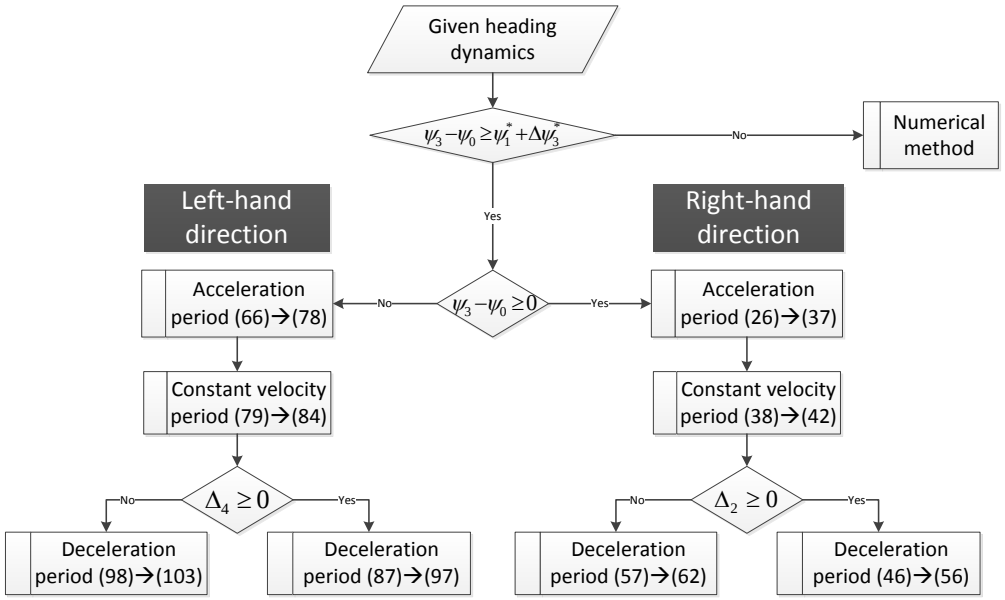

Fig. 18 Solution checking map

In this dissertation, the closed-form solution is found under the condition of $\psi_3 - \psi_0 \geq \psi_1^* + \Delta\psi_3^*$ (first condition). In other words, the constant velocity segment always exists.

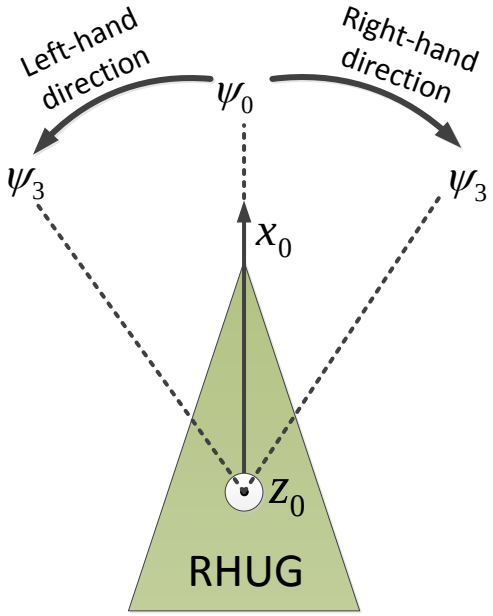

Fig. 19 Positive and negative domains in TOT for heading control

Table 4 Definition of TOT trajectory in heading dynamics

Parameter	Description
First segment	Acceleration period
Second segment	Constant velocity period
Third segment	Deceleration period
r_{d1}	The first segment of angular velocity trajectory
r_{d2}	The second segment of angular velocity trajectory
r_{d3}	The third segment of angular velocity trajectory
ψ_{d1}	The first segment of angle trajectory
ψ_{d2}	The second segment of angle trajectory
ψ_{d3}	The third segment of angle trajectory
$\dot{r}_{\mathrm{d1}}$	The first segment of angular acceleration trajectory
$\dot{r}_{\mathrm{d2}}$	The second segment of angular acceleration trajectory
$\dot{r}_{\mathrm{d3}}$	The third segment of angular acceleration trajectory

In Fig. 18, if the first condition is satisfied, the solution of the heading dynamics can be divided into left-hand and right-hand directions due to the absolute function in the hydrodynamic term. The right-hand direction means that the vehicle will rotate in the clockwise direction with positive angle. And the left-hand direction is for the counter-clockwise direction with negative angle, as illustrated in Fig. 19. And variables and definitions of TOT for heading dynamics are shown in Table 4.

3.3.1 Right-hand direction

In this subsection, it is assumed that the value of r_d is positive, so the trajectory solution will satisfy the dynamics as described in (22). And this dynamic can be solved easily using the integral form of (23).

$$\dot{r}_d = ar_d^2 + br_d + c \tag{22}$$

$$\int_{t_0}^{t} \frac{dr_d}{ar_d^2 + br_d + c} = t + C_1 \tag{23}$$

In this dissertation, the TOT trajectory is formulated under the first condition. And the process of solving the TOT profile is similar for right-hand and left-hand directions. The closed-form solution in each direction is divided into two solutions due to the positive and negative determinant Δ_2 (for right-hand direction) or Δ_4 (for left-hand direction), as shown in Fig. 18.

3.3.1.1 Acceleration period

$$\int_{t_0}^{t_1} \frac{dr_{d1}}{ar_{d1}^2 + br_{d1} + c_1} = t + C_1 \tag{24}$$

$$\Delta_1 = b^2 - 4ac_1 > 0 \ (a < 0, b < 0 \ and \ c_1 = \frac{u_{max}}{\alpha} > 0) \tag{25}$$

From the integral equation of (24), the determinant of the denominator is expressed as (25). It shows that there are two roots x_1 and x_2 for the denominator of $ar_{d1}^2 + br_{d1} + c_1$ as shown in (27), (28) and (29). Due to the conditions of heading dynamics in (25), the relating equation of x_1 and x_2 is shown in (30). These properties will be used to reduce the complexity of the next formulas.

$$\int_{t_0}^{t_1} \frac{dr_{d1}}{a(r_{d1} - x_1)(r_{d1} - x_2)} = t + C_1 \tag{26}$$

$$\begin{cases} x_1 + x_2 = \dfrac{-b}{a} < 0 \\ x_1 x_2 = \dfrac{c_1}{a} < 0 \end{cases} \tag{27}$$

$$x_1 = \frac{-b + \sqrt{\Delta_1}}{2a} > 0 \tag{28}$$

$$x_2 = \frac{-b - \sqrt{\Delta_1}}{2a} < 0 \tag{29}$$

$$|x_2| > |x_1| \tag{30}$$

By finding the root of the denominator, the equation (31) can be derived from (24). And the solution of r_{d1} can be obtained easily as (32) with the initial conditions of (33) and (34).

$$\frac{1}{a(x_1 - x_2)} ln\left(\frac{x_1 - x_2}{r_{d1} - x_2} - 1\right) = t + C_1 \tag{31}$$

$$r_{d1} = (x_1 - x_2)\frac{1}{e^{a(x_1 - x_2)(t + C_1)} + 1} + x_2 \tag{32}$$

$$r_0 = r_{d1}(t_0) \tag{33}$$

$$C_1 = \frac{1}{a(x_1 - x_2)} ln\left(\frac{x_1 - x_2}{r_0 - x_2} - 1\right) - t_0 \tag{34}$$

When the angular velocity trajectory is found as the function of time, the angle and angular acceleration trajectory can be obtained using the time integral and derivative. The angle trajectory can be formulated as (35) with the boundary condition as (36), and the angular acceleration trajectory can be obtained as (37).

$$\psi_{d1} = -\frac{1}{a} ln\left(e^{a(x_1 - x_2)(t + C_1)} + 1\right) + x_2 t + C_2 \tag{35}$$

$$C_2 = \psi_2 + \frac{1}{a} ln\left(e^{a(x_1 - x_2)(t + C_1)} + 1\right) - x_2 t_0 \tag{36}$$

$$\dot{r}_{d1} = -a(x_1 - x_2)^2 \frac{e^{a(x_1-x_2)(t+C_1)}}{(e^{a(x_1-x_2)(t+C_1)} + 1)^2} \tag{37}$$

3.3.1.2 Constant velocity period

This subsection is for solving the same equation of dynamics as the previous subsection with the condition of zero angular acceleration as described in (38). With this condition, the constant angular velocity r_{d2} will be one of the roots, x_1 or x_2. But this case is for the right-hand direction, so the positive root x_1 is considered as the solution of r_{d2}, as shown in (39), and this root is also the critical value r_1^*.

$$\dot{r}_{d2} = 0 \Leftrightarrow a r_{d2}^2 + b r_{d2} + c_1 = 0 \tag{38}$$

$$r_{d2} = x_1 = r_1^* > 0 \tag{39}$$

The angle trajectory can be obtained as (40) by taking the integral of (39), and the angular acceleration trajectory is zero from t_1 to t_2. The critical value of the angle ψ_1^* is defined as (43), and the critical time t_1^* is obtained as (42). These values are important for finding the value of t_2 and t_3.

$$\psi_{d2} = r_1^* t + C_5 \tag{40}$$

$$\psi_{d2} = r_1^* t + C_5 = \psi_1^* - r_1^* t_1^* \tag{41}$$

$$t_1^* = \frac{1}{a(x_1 - x_2)} ln\left(\frac{x_1 - x_2}{r_1^* - x_2} - 1\right) - C_1 \tag{42}$$

$$\psi_1^* = \psi(t_1^*) \tag{43}$$

3.3.1.3 Deceleration period

The dynamics equation is changed to (44) with the scaled input c_2. In this case, the sign of the determinant Δ_2 is not specified yet, as shown in (45).

$$\int_{t_0}^{t_1} \frac{dr_{d1}}{ar_{d1}^2 + br_{d1} + c_2} = t + C_1 \tag{44}$$

$$\Delta_2 = b^2 - 4ac_2 \quad (a < 0, b < 0 \; and \; c_2 = \frac{u_{min}}{\alpha} < 0) \tag{45}$$

3.3.1.3.1 If $\Delta_2 \geq 0$

In the case of positive determinant Δ_2, there are two roots s_1 and s_2 as shown in (48) and (49) with some properties from (47) to (50).

$$\int_{t_2}^{t_3} \frac{dr_{d3}}{a(r_{d3} - s_1)(r_{d3} - s_2)} = t + C_3 \tag{46}$$

$$\begin{cases} s_1 + s_2 = \dfrac{-b}{a} < 0 \\ s_1 s_2 = \dfrac{c_2}{a} > 0 \end{cases} \tag{47}$$

$$s_1 = \frac{-b + \sqrt{\Delta_2}}{2a} < 0 \tag{48}$$

$$s_2 = \frac{-b - \sqrt{\Delta_2}}{2a} < 0 \tag{49}$$

$$|s_2| > |s_1| \tag{50}$$

The trajectory solution can be solved in the same way as the acceleration segment from (51) to (56). The angular velocity trajectory is the function of time with the initial condition of (52).

$$r_{d3} = (s_2 - s_1)\frac{1}{e^{a(s_1-s_2)(t+C_3)} - 1} + s_2 \tag{51}$$

$$C_3 = \frac{1}{a(s_1 - s_2)} ln\left(\frac{r_1^* - s_1 - 1}{r_1^* - s_2}\right) - t_2 \tag{52}$$

The angle trajectory can be obtained as (53) by taking the integral of (51). The boundary condition for the angle trajectory is defined as (55). It is noted that the desired angle should be equal to the angle trajectory at t_3 as shown in (54).

$$\psi_{d3} = -\frac{1}{a} ln\left|1 - e^{a(s_2-s_1)(t+C_3)}\right| + s_2 t + C_4 \tag{53}$$

$$\psi_{d3}(t_3) = \psi_3 \tag{54}$$

$$C_4 = \psi_3 + \frac{1}{a} ln\left|1 - e^{a(s_2-s_1)(t+C_3)}\right| - s_2 t_3 \tag{55}$$

The angular acceleration trajectory can be derived as (56) without any boundary condition.

$$\dot{r}_{d3} = -a(s_2 - s_1)^2 \frac{e^{a(s_2-s_1)(t+C_3)}}{(e^{a(s_2-s_1)(t+C_3)} - 1)^2} \tag{56}$$

3.3.1.3.1 If $\Delta_2 < 0$

When the determinant Δ_2 is negative, the dynamic equation can be formulated as (57). In this case, the angular velocity trajectory is formed in the tangent function as (58) with the boundary condition as (59).

$$\frac{1}{a}\int_{t_2}^{t_3}\frac{dr_{d3}}{\left(r_{d3}+\frac{b}{2a}\right)^2+\left(\sqrt{\frac{-\Delta_2}{4a^2}}\right)^2}=t+C_3 \tag{57}$$

$$r_{d3}=-\frac{2a}{\sqrt{-\Delta_2}}tan\left(\frac{-\sqrt{-\Delta_2}}{2}(t+C_3)\right)-\frac{b}{2a} \tag{58}$$

$$C_3=-\frac{2}{\sqrt{-\Delta_2}}arctan\left(\frac{-\sqrt{-\Delta_2}\left(r_1^*+\frac{b}{2a}\right)}{2a}\right)-t_2 \tag{59}$$

And then, the angle and angular acceleration trajectory can be obtained as (60) and (62) respectively. The boundary condition of the angle trajectory can be specified in two way as (61) based on t_2 or t_3.

$$\psi_{d3}=\frac{4a}{\Delta_2}ln\left|cos\left(\frac{-\sqrt{-\Delta_2}}{2}(t+C_3)\right)\right|-\frac{b}{2a}t+C_4 \tag{60}$$

$$\begin{aligned}C_4&=\psi_3-\frac{4a}{\Delta_2}ln\left|cos\left(\frac{-\sqrt{-\Delta_2}}{2}(t_3+C_3)\right)\right|+\frac{b}{2a}t_3\\&=\psi_2-\frac{4a}{\Delta_2}ln\left|cos\left(\frac{-\sqrt{-\Delta_2}}{2}(t_2+C_3)\right)\right|+\frac{b}{2a}t_2\end{aligned} \tag{61}$$

$$\dot{r}_{d3}=a\left(1+tan^2\left(\frac{-\sqrt{-\Delta_2}}{2}(t+C_3)\right)\right) \tag{62}$$

3.3.2 Left-hand direction

In the negative domain, the dynamics can be presented as (63) and (64).

$$\dot{r}_d = -ar_d^2 + br_d + c \tag{63}$$

$$\int_{t_0}^{t} \frac{dr_d}{-ar_d^2 + br_d + c} = t + C_1 \tag{64}$$

3.3.2.1 Acceleration period

The control input for this period is the minimum scaled input c_2. The determinant Δ_3 is always positive due to the characteristic of a, b and c_2 as shown in (65). The dynamics of this period can be derived as (66) and (67) with the roots of the denominator as x_1 and x_2. Therefore, the solution is similar with the former subsection in the acceleration period. Only values and conditions of x_1 and x_2 are different to the previous one, as presented from (68) to (71). The summation and multiplication conditions of x_1 and x_2 are formulated in (70) which helps us to define the sign of x_1 and x_2 in (68) and (69).

$$\Delta_3 = b^2 + 4ac_2 > 0 \ (a < 0, b < 0 \ and \ c_2 = \frac{u_{min}}{\alpha} < 0) \tag{65}$$

$$\int_{t_0}^{t_1} \frac{dr_{d1}}{-ar_{d1}^2 + br_{d1} + c_2} = t + C_1 \tag{66}$$

$$\int_{t_0}^{t_1} \frac{dr_{d1}}{-a(r_{d1} - x_1)(r_{d1} - x_2)} = t + C_1 \tag{67}$$

$$x_1 = \frac{b - \sqrt{\Delta_3}}{-2a} < 0 \tag{68}$$

$$x_2 = \frac{b + \sqrt{\Delta_3}}{-2a} > 0 \tag{69}$$

$$\begin{cases} x_1 + x_2 = \dfrac{b}{a} > 0 \\ x_1 x_2 = -\dfrac{c_2}{a} < 0 \end{cases} \tag{70}$$

$$|x_2| \geq |x_1| \tag{71}$$

Eq. (67) can be solved for r_{d1} through Eq. (72) and (73). With the initial condition of angular velocity, the constant C_1 can be calculated as (75).

$$\frac{1}{a(x_2 - x_1)} ln\left(\frac{x_1 - x_2}{r_{d1} - x_2} - 1\right) = t + C_1 \tag{72}$$

$$r_{d1} = (x_1 - x_2)\frac{1}{e^{a(x_2 - x_1)(t + C_1)} + 1} + x_2 \tag{73}$$

$$r_0 = r_{d1}(t_0) \tag{74}$$

$$C_1 = \frac{1}{a(x_2 - x_1)} ln\left(\frac{x_1 - x_2}{r_0 - x_2} - 1\right) - t_0 \tag{75}$$

Similarly, the angle trajectory can be obtained as (76) by taking the integral of the angular velocity trajectory. The constant C_2 in the angle trajectory can be solved using the initial condition, as shown in (77). And then, the acceleration trajectory can be obtained as (78) by taking the derivative of Eq. (73).

$$\psi_{d1} = \frac{1}{a} ln\left(e^{a(x_1 - x_2)(t + C_1)} + 1\right) + x_2 t + C_2 \tag{76}$$

$$C_2 = \psi_0 - \frac{1}{a} ln\left(e^{a(x_1 - x_2)(t_0 + C_1)} + 1\right) - x_2 t_0 \tag{77}$$

$$\dot{r}_{d1} = -a(x_1 - x_2)^2 \frac{e^{a(x_2 - x_1)(t + C_1)}}{(e^{a(x_2 - x_1)(t + C_1)} + 1)^2} \tag{78}$$

3.3.2.2 Constant velocity period

In this period, the angular acceleration is zero, so the angular velocity trajectory can be solved using Eq. (79). In the left-hand direction, the angular velocity should be negative and equal to the roots of Eq. (79). Among the roots of x_1 and x_2, only x_1 is negative, as defined in (68). Therefore, the angular velocity trajectory will be equal to x_1 and this value is also equal to the critical value r_1^*.

$$\dot{r}_{d2} = 0 \Leftrightarrow -a r_{d2}^2 + b r_{d2} + c_2 = 0 \tag{79}$$

$$r_{d2} = x_1 = r_1^* < 0 \tag{80}$$

The angle trajectory can be obtained as Eq. (81) and its constant value C_5 can be calculated as Eq. (82) by some critical values in (80), (83) and (84).

$$\psi_{d2} = r_1^* t + C_5 \tag{81}$$

$$C_5 = \psi_1^* - r_1^* t_1^* \tag{82}$$

$$t_1^* = \frac{1}{a(x_2 - x_1)} ln\left(\frac{x_1 - x_2}{r_1^* - x_2} - 1\right) - C_1 \tag{83}$$

$$\psi_1^* = \psi(t_1^*) \tag{84}$$

3.3.2.3 Deceleration period

Due to the sign of the determinant Δ_4, the solution of dynamics (85) will be divided into two solutions. If Δ_4 is positive, the trajectory solution will follow subsection 3.3.2.3.1. Otherwise, the trajectory solution will be defined in subsection 3.3.2.3.2.

$$\int_{t_0}^{t_1} \frac{dr_{d1}}{-ar_{d1}^2 + br_{d1} + c_1} = t + C_1 \tag{85}$$

$$\Delta_4 = b^2 + 4ac_1 \qquad (a < 0, b < 0 \; and \; c_1 = \frac{u_{max}}{\alpha} > 0) \tag{86}$$

3.3.2.3.1 $\Delta_4 \geq 0$

If the determinant Δ_4 is positive, there are two roots of the denominator in (85) as s_1 and s_2. And the properties of the roots can be organized from (88) to (91). By using these roots, the dynamics can be rewritten as (87), which is a solvable dynamics.

$$\int_{t_2}^{t_3} \frac{dr_{d3}}{-a(r_{d3} - s_1)(r_{d3} - s_2)} = t + C_3 \tag{87}$$

$$\begin{cases} s_1 + s_2 = \dfrac{b}{a} > 0 \\ s_1 s_2 = -\dfrac{c_1}{a} > 0 \end{cases} \tag{88}$$

$$s_1 = \frac{-b - \sqrt{\Delta_2}}{-2a} > 0 \tag{89}$$

$$s_2 = \frac{-b + \sqrt{\Delta_2}}{-2a} > 0 \tag{90}$$

$$|s_2| > |s_1| \tag{91}$$

The solution of angular velocity trajectory can be derived as Eq. (92), which is a function of time. The boundary condition can be solved using Eq. (93).

$$r_{d3} = (s_2 - s_1)\frac{1}{e^{a(s_1 - s_2)(t + C_3)} - 1} + s_2 \tag{92}$$

$$C_3 = \frac{1}{a(s_1 - s_2)} ln\left(\frac{r_1^* - s_1 - 1}{r_1^* - s_2}\right) - t_2 \tag{93}$$

Once the angular velocity trajectory is defined, the angle trajectory can be easily obtained as (94) by taking the integral of Eq. (92). The constant value C_4 is calculated by using the condition of the time t_3. Finally, the angular acceleration trajectory is defined as (97).

$$\psi_{d3} = -\frac{1}{a} ln\left|1 - e^{a(s_2 - s_1)(t + C_3)}\right| + s_2 t + C_4 \tag{94}$$

$$\psi_{d3}(t_3) = \psi_3 \tag{95}$$

$$C_4 = \psi_3 + \frac{1}{a} ln\left|1 - e^{a(s_2 - s_1)(t_3 + C_3)}\right| - s_2 t_3 \tag{96}$$

$$\dot{r}_{d3} = -a(s_2 - s_1)^2 \frac{e^{a(s_2 - s_1)(t + C_3)}}{(e^{a(s_2 - s_1)(t + C_3)} - 1)^2} \tag{97}$$

3.3.2.3.2 $\Delta_4 < 0$

If the determinant Δ_4 is negative, the dynamics in Eq. (85) can be rewritten as (98). And then, the angular velocity trajectory can be obtained as (99) by solving Eq. (98). The constant C_3 can be computed as (100) using the condition of the time t_2.

$$\frac{1}{a}\int_{t_2}^{t_3}\frac{dr_{d3}}{\left(r_{d3}+\frac{b}{2a}\right)^2+\left(\sqrt{\frac{-\Delta_2}{4a^2}}\right)^2}=t+C_3 \tag{98}$$

$$r_{d3}=-\frac{2a}{\sqrt{-\Delta_2}}tan\left(\frac{-\sqrt{-\Delta_2}}{2}(t+C_3)\right)-\frac{b}{2a} \tag{99}$$

$$C_3=-\frac{2}{\sqrt{-\Delta_2}}arctan\left(\frac{-\sqrt{-\Delta_2}\left(r_1^*+\frac{b}{2a}\right)}{2a}\right)-t_2 \tag{100}$$

The angle trajectory can be obtained as Eq. (101) by taking the integral of the angular velocity trajectory. The constant C_4 can be represented in two ways, as described in (102). Finally, the angular acceleration trajectory can be obtained as (103) by taking the derivative of the angular velocity trajectory.

$$\psi_{d3}=\frac{4a}{\Delta_2}ln\left|cos\left(\frac{-\sqrt{-\Delta_2}}{2}(t+C_3)\right)\right|-\frac{b}{2a}t+C_4 \tag{101}$$

$$\begin{aligned}C_4&=\psi_3-\frac{4a}{\Delta_2}ln\left|cos\left(\frac{-\sqrt{-\Delta_2}}{2}(t_3+C_3)\right)\right|+\frac{b}{2a}t_3\\&=\psi_2-\frac{4a}{\Delta_2}ln\left|cos\left(\frac{-\sqrt{-\Delta_2}}{2}(t_2+C_3)\right)\right|+\frac{b}{2a}t_2\end{aligned} \tag{102}$$

$$\dot{r}_{d3}=a\left(1+tan^2\left(\frac{-\sqrt{-\Delta_2}}{2}(t+C_3)\right)\right) \tag{103}$$

3.4 Time-optimal trajectory

This section shows the way to get the TOT profile based on the closed-form solution as presented in the right-hand direction. The constraints for solving the TOT trajectory is declared from (104) to (107).

$$r(t_0) = r_0 \tag{104}$$

$$\psi(t_0) = \psi_0 \tag{105}$$

$$r(t_3) = r_3 \tag{106}$$

$$\psi(t_3) = \psi_3 \tag{107}$$

There are two important variables ψ_1^* and $\Delta\psi_3^*$ which need to be defined before solving for t_1, t_2 and t_3. The condition for using the TOT trajectory is shown in (108).

$$\psi_3 - \psi_0 > \psi_1^* + \Delta\psi_3^* \tag{108}$$

The critical value ψ_1^* can be found using the critical time t_1^* which is easy to obtain through r_1^*, as described in (109), (110) and (111).

$$r_1^* = x_1 \tag{109}$$

$$t_1^* = \frac{1}{a(x_1 - x_2)} ln\left(\frac{x_1 - x_2}{r_1^* - x_2} - 1\right) - C_1 \tag{110}$$

$$\psi_1^* = -\frac{1}{a} ln\left(e^{a(x_1 - x_2)(t_1^* + C_1)} + 1\right) + x_2 t_1^* + C_2 \tag{111}$$

The second critical value $\Delta\psi_3^*$ can be derived from (112) to (115). The term $(t_3 - t_2)$ in (112) can be substituted with the subtraction between (113) and (114). The final formula for $\Delta\psi_3^*$ is expressed as (115).

$$\begin{aligned} &\Delta\psi_3^* = \psi_{d3}(t_3) - \psi_{d2}(t_2) \\ \Leftrightarrow\ &\Delta\psi_3^* = -\frac{1}{a} ln \left| \frac{1 - e^{a(s_2 - s_1)(t_3 + C_3)}}{1 - e^{a(s_2 - s_1)(t_2 + C_3)}} \right| + s_2(t_3 - t_2) \end{aligned} \tag{112}$$

$$\begin{aligned} &r_{d3}(t_3) = r_3 \\ \Leftrightarrow\ &\frac{s_2 - s_1}{e^{a(s_1 - s_2)(t_3 + C_3)} - 1} + s_2 = r_3 \\ \Leftrightarrow\ &t_3 + C_3 = \frac{1}{a(s_1 - s_2)} \ln \left| \frac{r_3 - s_1}{r_3 - s_2} \right| \end{aligned} \tag{113}$$

$$\begin{aligned} &r_{d3}(t_2) = r_1^* \\ \Leftrightarrow\ &\frac{s_2 - s_1}{e^{a(s_1 - s_2)(t_2 + C_3)} - 1} + s_2 = r_1^* \\ \Leftrightarrow\ &t_2 + C_3 = \frac{1}{a(s_1 - s_2)} \ln \left| \frac{r_1^* - s_1}{r_1^* - s_2} \right| \end{aligned} \tag{114}$$

$$\Delta\psi_3^* = -\frac{1}{a} ln \left| \frac{1 - \frac{r_3 - s_2}{r_3 - s_1}}{1 - \frac{r_1^* - s_2}{r_1^* - s_1}} \right| + \frac{s_2}{a(s_1 - s_2)} ln \left| \frac{(r_3 - s_1)(r_1^* - s_2)}{(r_3 - s_2)(r_1^* - s_1)} \right| \tag{115}$$

Then, the profile of TOT trajectory can be easily derived from (116) to (118). Each segment of TOT trajectory can be separated at t_1, t_2 and t_3. The first segment of TOT starts at the time t_0 and ends at the time t_1 using the closed-form solutions of ψ_{d1}, r_{d1} and $\dot{r}_{d1}$. The second segment of TOT from t_1 to t_2 is defined as ψ_{d2}, r_{d2} and $\dot{r}_{d2}$. And finally, the third segment of TOT are ψ_{d3}, r_{d3} and $\dot{r}_{d3}$ from t_2 to t_3.

$$t_1 = t_1^* \tag{116}$$

$$t_2 = t_1 + \frac{\psi_3 - \psi_1^* - \Delta\psi_3^*}{r_1^*} \tag{117}$$

$$t_3 = t_2 + \frac{1}{a(s_1 - s_2)} ln \left| \frac{(r_3 - s_1)(r_1^* - s_2)}{(r_3 - s_2)(r_1^* - s_1)} \right| \tag{118}$$

3.5 Super-twisting sliding mode control

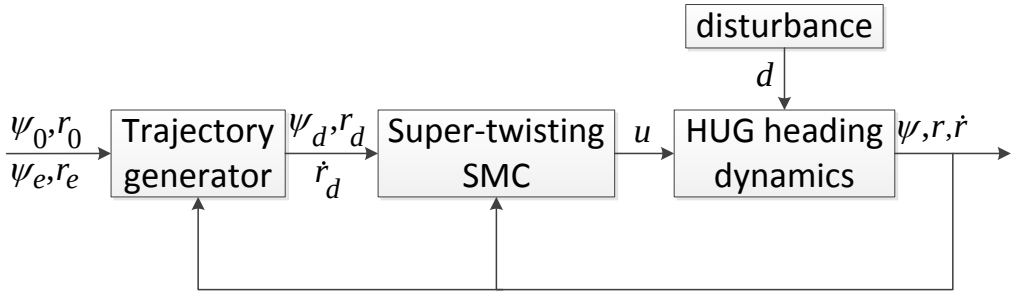

Fig. 20 Heading control scheme with TOT trajectory

The TOT trajectory will feed the desired angle, angular rate, and angular acceleration to the sliding mode controller (SMC) with a higher-order switching law so called as super-twisting sliding mode control (ST-SMC). The steps to design the SMC control is well-known and easy to established from (119) to (129). It is noted that both SMC and ST-SMC control laws are discussed here to compare the chattering problem between two controllers.

$$s = (r - r_d) + \lambda(\psi - \psi_d) \tag{119}$$

$$\dot{s} = (\dot{r} - \dot{r}_d) + \lambda(r - r_d) \tag{120}$$

$$\dot{s} = a|r|r + br - \dot{r}_d + \lambda(r - r_d) + \frac{u}{\alpha} + \frac{d}{\alpha} \tag{121}$$

The sliding surface s can be defined as (119), which is the function of velocity and position error. And the derivative of the sliding surface can be derived as (120). The dynamics now can be integrated into $\dot{s}$ as (121). The control input appeared in the derivative of the sliding surface so the control

law can be derived using the equivalent amount of moment, as shown in (122).

$$u = \hat{\alpha}\left(-\hat{a}|r|r - \hat{b}r + \dot{r}_d - \lambda(r - r_d)\right) + u_{sw} \tag{122}$$

The switching law can be chosen as (123) for SMC or (124) for ST-SMC.

$$u_{sw} = -Ksgn(s) \tag{123}$$

$$u_{sw} = -K_1\sqrt{|s|}sgn(s) - \int_{t_0}^{t} K_2 sgn(s)dt \tag{124}$$

In the sliding mode control, it is popular to choose a Lyapunov function as (125). And the derivative of V can be obtained as the product of the sliding surface and its derivative, as shown in (126).

$$V = \frac{1}{2}s^2 \tag{125}$$

$$\dot{V} = s\dot{s} \tag{126}$$

By making the derivative of V negative definite, the conditions of the control gain K for SMC, and the control gains K_1 and K_2 for ST-SMC can be defined in (127), (128) and (129).

$$K \geq \Omega|\Delta_a|\mathrm{r}|r + \Delta_b r + \eta| + D \tag{127}$$

$$K_1 \geq \frac{\Omega}{\sqrt{|s|}}|\Delta_a|\mathrm{r}|r + \Delta_b r + \eta| \tag{128}$$

$$K_2 \geq \mathrm{D} \tag{129}$$

where, $|\alpha| \leq \Omega$; $|d| \leq D$; $|a - \hat{a}| \leq \Delta_a$; $\left|b - \hat{b}\right| \leq \Delta_b$; $\eta > 0$.

3.6 Computer simulation

To show the effectiveness of the proposed trajectory, three simulations will be conducted in the next subsections. The first simulation will show the TOT trajectory combined with tracking control without any uncertainties. The second simulation will perform sliding mode control with parameter uncertainty and external disturbances. And the robustness and chattering reduction will be discussed in the third simulation.

The heading parameters are defined as $\rho = 1031\text{kg/m}^3$, $L = 1.67\text{m}$, $I_{zz} = 4.0548\text{kgm}^2$, $N_{\dot{r}} = -0.00136(\rho L^5/2)\text{kgm}^2$, $N_r = -0.00467(\rho L^4/2)\text{kgm}^2$, $N_{|r|r} = -0.00053(\rho L^5/2)\text{kgm}^2$, $u_{max} = 15\text{Nm}$ and $u_{min} = -12\text{Nm}$. The sliding function is defined by $\lambda = 2$ and controller parameters are used as $\eta = 0.5$ for the first and second simulations and $\eta = 3$ for the third simulation due to the different type of controller. The parameter uncertainties will be defined as $|\alpha| \leq \Omega = 1.2\hat{\alpha}$, $|d| = |4\sin(5t)| \leq D = 4$; $|a - \hat{a}| \leq \Delta_a = 0.8\hat{a}$ and $\left|b - \hat{b}\right| \leq \Delta_b = 0.8\hat{b}$. Here, $\hat{a} = \frac{N_{|r|r}}{I_{zz} - N_{\dot{r}}}$; $\hat{b} = \frac{N_r}{I_{zz} - N_{\dot{r}}}$; $\hat{\alpha} = I_{zz} - N_{\dot{r}}$. The inertial term has 20% uncertainty while other hydrodynamic terms have 80% uncertainty. This assumption is suitable because the inertia part can be measured by the pendulum table while the hydrodynamic term is usually estimated by the CFD method. Therefore, the uncertainty of the hydrodynamic terms should be greater than that of the inertia part. In this case, it is 20% for α and 80% for both a and b.

3.6.1 Simulation 1

In this simulation, there are no parameter uncertainties and disturbances in the heading dynamic. It means that the parameters are known perfectly and disturbance $d = 0$ in Eq. (19) for checking the operation of the combination

of TOT and SMC control. The tracking controller successfully drive the dynamics to track the TOT trajectory and the control input is fully used as the designed boundary between 15Nm and -12Nm in Fig. 21a. Position, velocity and acceleration track the TOT trajectory very well in Fig. 21b, c and d. This result proves that the combination of the SMC and TOT trajectories has a good tracking performance. However, in the real application, the system parameters are estimated inaccurately and the environmental disturbances always exist. Therefore, to verify the proposed trajectory and controller, the second and third simulation will be performed with parameter uncertainties and external disturbances.

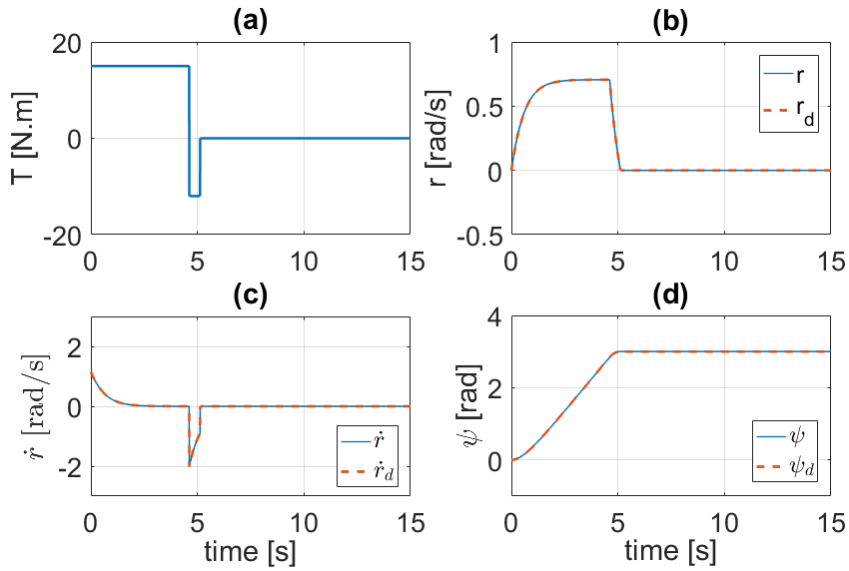

Fig. 21 TOT trajectory and SMC without uncertainties.
(a) torque input, (b) angular velocity, (c) angular acceleration, and (d) angle curves as the function of time

3.6.2 Simulation 2

This simulation will use the TOT trajectory with the tracking controller of SMC with the parameter uncertainty and disturbance. A wave-formed disturbance is simulated to affect the dynamics from 10s to 12s. This setup

will let us analyze the effect of parameter uncertainty and disturbance easily. The tracking performance of this simulation is shown in Fig. 22. Due to the parameter uncertainty, there are chattering phenomenon in control input and acceleration in Fig. 22a and Fig. 22c. From 0s to 10s, only parameter uncertainties exist, so that the control input and acceleration chattering do not have any specified shape. On the other hand, from 10s to 12s, the general pattern in the acceleration is waveform due to the presence of the wave-formed disturbance. And this behavior can also be seen in the sliding surface in Fig. 23 with the wave-formed chattering between 10s and 12s.

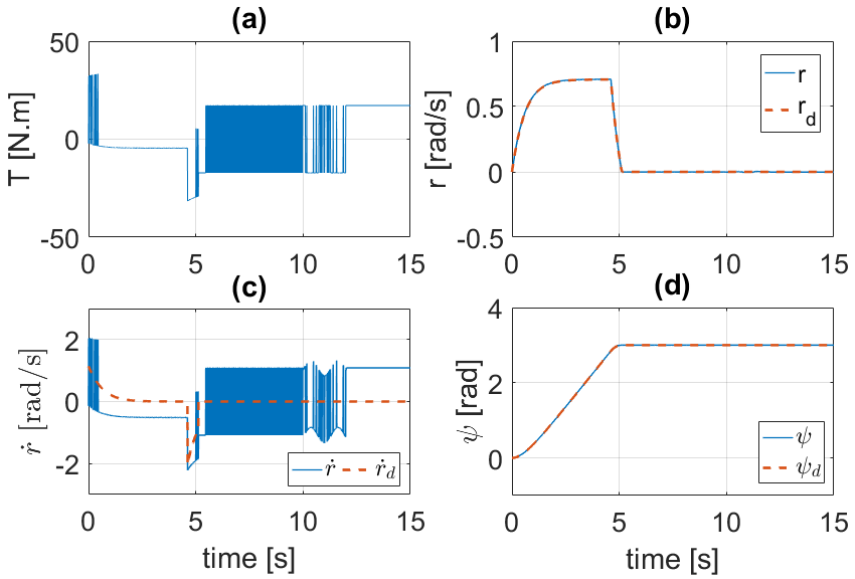

Fig. 22 TOT trajectory and SMC with uncertainties and disturbances.
(a) torque input, (b) velocity, (c) acceleration, and (d) angle position curves as the function of time

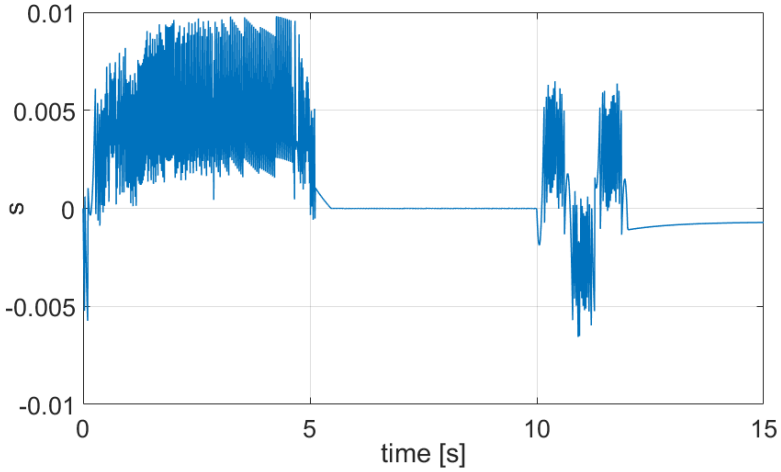

Fig. 23 Sliding surface in SMC as a function of velocity and position errors

3.6.3 Simulation 3

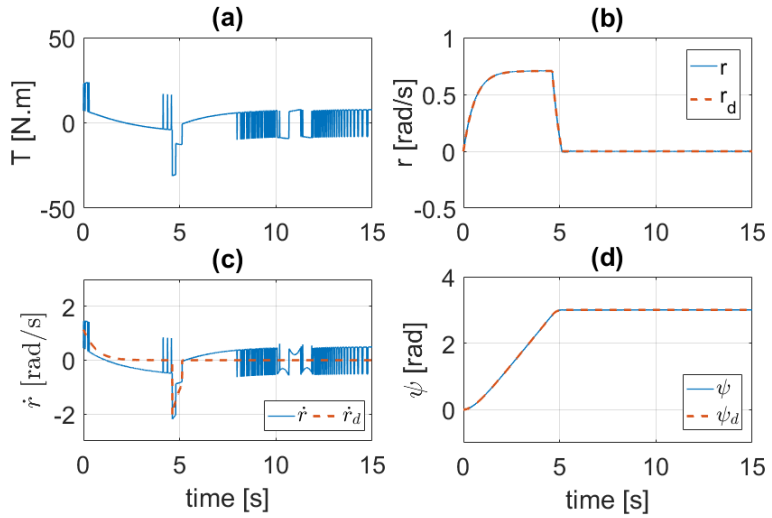

Fig. 24 TOT trajectory and ST-SMC with uncertainties and disturbances. (a) torque input, (b) angular velocity, (c) angular acceleration, and (d) angle curves

With the same condition as the second simulation, the tracking controller of ST-SMC is applied to the heading dynamics. The chattering phenomenon can be reduced by using saturation function for sliding function s. However, this method will affect the tracking error due to the saturation function. In this

study, the high-order switching technique is used. With this ST-SMC, the chattering problem will be improved while the tracking error still has the same quality as the SMC case.

In Fig. 24, the chattering phenomenon is reduced significantly in control input compared with that in Fig. 22. Moreover, the sliding quantity in Fig. 25 is kept under 0.01, which is the same as the sliding quantity in Fig. 23. Therefore, the ST-SMC has improved the performance of tracking control in terms of reducing the chattering problem while keeping the same tracking error.

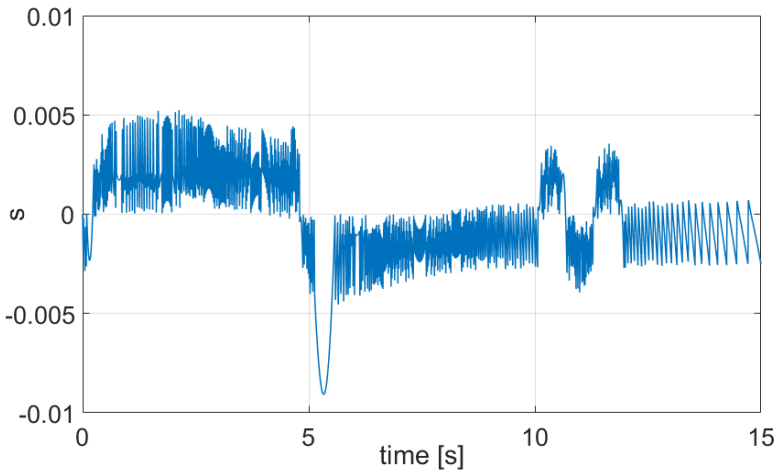

Fig. 25 Sliding surface in ST-SMC as a function of velocity and position errors

Chapter 4. Time-optimal trajectory for heaving motion control using buoyancy engine and propeller individually

4.1. Heave dynamics and TOT

The depth control is a challenging task for RHUG due to the slow speed of the buoyancy engine. In this chapter, a TOT trajectory for the heaving control of RHUG will be proposed based on the speed of the buoyancy engine and the saturation of the buoyancy engine and thrusters. The heave dynamics can be described with two first order differential systems as (130). Here, $a = m - Z_{\dot{w}}$; $b = -Z_{|w|w}$; f is the control force acting on the vehicle in heave motion.

$$\begin{aligned} a\dot{w} + b|w|w &= f \\ \dot{z} &= w \end{aligned} \tag{130}$$

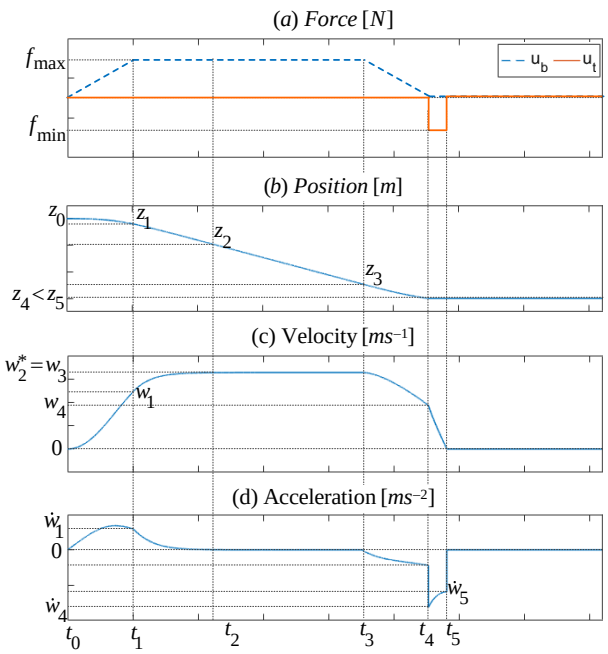

Fig. 26 TOT trajectory for depth dynamic of HUG

The heaving motion control strategy for this RHUG system can be illustrated as Fig. 26a. The dashed blue line is the buoyancy force by the buoyancy engine where the up-slope means the compressing rate of air in the cylinder and down-slope means the expending rate. And the solid orange line represents the designed force for the thrusters. Some terms are defined in Table 5 for the TOT trajectory.

Table 5 Definition of TOT trajectory in heave dynamics

Parameter	Description
f_{max}	Maximum force
f_{min}	Minimum force
z_0	Initial depth
z_5	Desired depth
w_{d1}	The first segment in velocity trajectory
w_{d2}	The second segment in velocity trajectory
w_{d3}	The third segment in velocity trajectory
w_{d4}	The fourth segment in velocity trajectory
w_{d5}	The fifth segment in velocity trajectory
z_{d1}	The first segment in position trajectory
z_{d2}	The second segment in position trajectory
z_{d3}	The third segment in position trajectory
z_{d4}	The fourth segment in position trajectory
z_{d5}	The fifth segment in position trajectory
$\dot{w}_{\mathrm{d1}}$	The first segment in acceleration trajectory
$\dot{w}_{\mathrm{d2}}$	The second segment in acceleration trajectory
$\dot{w}_{\mathrm{d3}}$	The third segment in acceleration trajectory
$\dot{w}_{\mathrm{d4}}$	The fourth segment in acceleration trajectory
$\dot{w}_{\mathrm{d5}}$	The fifth segment in acceleration trajectory

The control force u_b is the net buoyancy force exerted by the buoyancy engine. And u_t is the thruster force generated by four propellers. In the UG system, the buoyancy engine is used for descending with small energy consumption. And the thruster force is only used when the vehicle glides near to the target depth, and for keeping the RHUG at the desired depth. By switching between two forces, the RHUG can be controlled to reach exactly

to the desired depth. The thruster force should be used after the vehicle achieves the neutral buoyancy.

In the RHUG system, the rate of the buoyancy force can be expressed as c_{max} for the increasing speed and c_{min} for the decreasing speed. Therefore, the buoyancy force that induces the RHUG system during the depth control is formulated as $c_{max}(t-t_0)$ and $c_{min}(t-\alpha)$. Here, t_0 and α are the initial time for descending motion and neutral condition respectively. Then, there are five periods of time needed to be defined clearly, as shown in Fig. 26. The first segment is from t_0 to t_1, the dynamics of this period can be referred to (131). And it is noted that $t_1 = t_0 + \frac{f_{max}}{c_{max}}$. The dynamics equation of the second and third segments can be formulated as (132) from t_1 to t_2 and from t_2 to t_3 respectively. The dynamics of the fourth and fifth segments can be established as (133) and (134) respectively. By solving all dynamics below, one can define the TOT trajectory of the RHUG system for the pure depth plant. However, this concept is only used for the deep operation because the RHUG should reach the maximum heave velocity as described in Fig. 26d. In other words, this case can be expressed by the condition of $z_5 \geq (z_2 - z_0) + (z_4 - z_3)$. This assumption is suitable for RHUG because the desired depth is normally set at several hundreds of meters.

$$a\dot{w}_d + bw_d^2 = c_{max}(t-t_0) \tag{131}$$

$$a\dot{w}_d + bw_d^2 = f_{max} \tag{132}$$

$$a\dot{w}_d + bw_d^2 = c_{min}(t-\alpha) \tag{133}$$

$$a\dot{w}_d + bw_d^2 = f_{min} \tag{134}$$

4.2. Analytical solution of heave dynamics with buoyancy and thruster force individually

4.2.1 First segment with positive rate

$$a\dot{w}_{d1} + bw_{d1}^2 = c_{max}(t - t_0) \tag{135}$$

In this first segment, the heave dynamics is shown in (135). If the variable w_{d1} is defined as $\frac{a}{b}\frac{\dot{y}}{y}$, then Eq. (135) can be rewritten as (136). The final equation in (136) is the Airy function, and it can be solved using the alternative function y as described in (137).

$$\begin{aligned} &\frac{a^2}{b}\left(\frac{\ddot{y}}{y} - \frac{\dot{y}^2}{y^2}\right) + \frac{a^2\dot{y}^2}{by^2} = c_{max}(t - t_0) \\ &\Leftrightarrow \frac{a^2}{b}\frac{\ddot{y}}{y} = c_{max}(t - t_0) \end{aligned} \tag{136}$$

$$y(t) = a_0 y_0(t) + a_1 y_1(t) \tag{137}$$

The components of function $y(t)$ can be defined as (138), (139) and (140).

$$y_0(t) = 1 + \frac{\sigma_1(t - t_0)^3}{6} + \frac{\sigma_1^2(t - t_0)^6}{180} + \frac{\sigma_1^3(t - t_0)^9}{12960} \tag{138}$$

$$y_1(t) = (t - t_0) + \frac{\sigma_1(t - t_0)^4}{12} + \frac{\sigma_1^2(t - t_0)^7}{504} + \frac{\sigma_1^3(t - t_0)^{10}}{45360} \tag{139}$$

$$\sigma_1 = \frac{bc_{max}}{a^2} \tag{140}$$

Once the function $y(t)$ is defined, its first and second derivative can be shown as (141) and (142) respectively.

$$\dot{y}(t) = a_0\dot{y}_0(t) + a_1\dot{y}_1(t) \tag{141}$$

$$\ddot{y}(t) = a_0\ddot{y}_0(t) + a_1\ddot{y}_1(t) \tag{142}$$

Then, the velocity trajectory can be formulated by the alternative function y as (143). And the acceleration trajectory can be obtained by taking the derivative of the velocity trajectory, as shown in (144). Finally, the position trajectory can be shown in (145) with the constant C_0 defined as (146).

$$w_{d1} = \frac{a}{b}\frac{\dot{y}}{y} \tag{143}$$

$$\dot{w}_{d1} = \frac{a}{b}\left(\frac{\ddot{y}}{y} - \frac{\dot{y}^2}{y^2}\right) \tag{144}$$

$$z_{d1} = \frac{a}{b}ln|y| + C_0 \tag{145}$$

$$C_0 = z_0 - \frac{a}{b}ln|a_0p_1 + a_1p_2| \tag{146}$$

where, $p_1 = y_0(t_0)$; $p_2 = y_1(t_0)$; $p_3 = \dot{y}_0(t_0)$; $p_4 = \dot{y}_1(t_0)$; $a_0 = 1$; $a_1 = -\frac{p_3}{p_4}a_0$.

4.2.2 Second segment with maximum input

$$a\dot{w}_{d2} + bw_{d2}^2 = f_{max} \tag{147}$$

The dynamics of the second segment is with the maximum input, as formulated in (147). The dynamics is solved for a closed-form solution in [33]. The results in that paper can be rewritten as (148), (149) and (150).

$$w_{d2} = \frac{2\sqrt{f_{max}/b}}{1 + e^{\frac{2}{a}\sqrt{bf_{max}}(t+C_1)}} - \sqrt{\frac{f_{max}}{b}} \tag{148}$$

$$\dot{w}_{d2} = \frac{4f_{max}}{a} \frac{e^{-\frac{2}{a}\sqrt{bf_{max}}(t+C_1)}}{\left(1 + e^{-\frac{2}{a}\sqrt{bf_{max}}(t+C_1)}\right)^2} \tag{149}$$

$$z_{d2} = \frac{a}{b} ln\left(1 + e^{\frac{2}{a}\sqrt{bf_{max}}(t+C_1)}\right) - \sqrt{\frac{f_{max}}{b}} t + C_2 \tag{150}$$

The formulas of the constants C_1 and C_2 are different from the work in [33] due to the different input geometries. For this dissertation, the author will calculate C_1 and C_2 at the time t_1, as shown in (151) and (152).

$$C_1 = \frac{-a}{2\sqrt{bf_{max}}} ln\left(\frac{2\sqrt{f_{max}/b}}{w_1 + \sqrt{f_{max}/b}} - 1\right) - t_1 \tag{151}$$

$$C_2 = z_1 - \frac{a}{b} ln\left(1 + e^{\frac{2}{a}\sqrt{bf_{max}}(t_1+C_1)}\right) + \sqrt{\frac{f_{max}}{b}} t_1 \tag{152}$$

4.2.3 Third segment with constant velocity

$$a\dot{w}_{d3} + bw_{d3}^2 = f_{max} \tag{153}$$

The desired depth for the underwater glider is typically several hundred meters. So, the constant velocity in the heave motion will be achieved for deep sea UGs. In other words, the third segment always exists. This segment has the dynamics specified in (153). The constant velocity in this segment is equal to w_2^*, or $w_3 = w_2^*$. And the position trajectory can be calculated by (154) with the boundary constant C_3 as (155).

$$z_{d3} = w_3 t + C_3 \tag{154}$$

$$C_3 = z_2 - w_2 t_2 \tag{155}$$

4.2.4 Fourth segment with negative rate

$$a\dot{w}_{d4} + bw_{d4}^2 = c_{min}(t - \alpha) \tag{156}$$

When the RHUG goes near to the desired depth, this segment will deal with when the net buoyancy force starts to decrease to zero. The delay of the buoyancy engine is specified in (157). The solution of this segment dynamics is the same as subsection 4.4.2.2. But the notation will be changed to distinguish it from the previous segments. Here, the alternative function $k(t)$ will be used to compute the trajectory.

$$\alpha = t_3 - \frac{f_{max}}{c_{min}} \tag{157}$$

The velocity trajectory can be solved as (158). Using the derivative of the velocity trajectory, the acceleration trajectory of this segment can be obtained as (159). And the position trajectory is found as (160) with the boundary condition as (161).

$$w_{d4} = \frac{a}{b}\frac{\dot{k}}{k} \tag{158}$$

$$\dot{w}_{d4} = \frac{a}{b}\left(\frac{\ddot{k}}{k} - \frac{\dot{k}^2}{k^2}\right) \tag{159}$$

$$z_{d4} = \frac{a}{b} ln|k| + C_4 \tag{160}$$

$$C_4 = z_0 - \frac{a}{b} ln|a_0 p_1 + a_1 p_2| \tag{161}$$

where,
$k(t) = n_0 k_0(t) + n_1 k_1(t)$; $y_0(t) = 1 + \frac{\sigma_4 (t-\alpha)^3}{6} + \frac{\sigma_4^2 (t-\alpha)^6}{180} + \frac{\sigma_4^3 (t-\alpha)^9}{12960}$;
$y_1(t) = (t-\alpha) + \frac{\sigma_1 (t-\alpha)^4}{12} + \frac{\sigma_1^2 (t-\alpha)^7}{504} + \frac{\sigma_1^3 (t-\alpha)^{10}}{45360}$; $\sigma_4 = \frac{b c_{min}}{a^2}$;
$\dot{k}(t) = n_0 \dot{k}_0(t) + n_1 \dot{k}_1(t)$; $\ddot{k}(t) = a_0 \ddot{k}_0(t) + a_1 \ddot{k}_1(t)$.

4.2.5 Fifth segment with minimum input

$$a\dot{w}_{d5} + b w_{d5}^2 = f_{min} \tag{162}$$

In the final segment, the thruster force will be used to make the vehicle achieve the desired depth in the shortest time. The dynamics of this segment can be written as (162). And this dynamics solution is a part of the work introduced in [33], and it will be rewritten as (163), (164) and (165) for the velocity, acceleration and position trajectory respectively.

$$w_{d5} = \sqrt{\frac{-f_{min}}{b}} tan\left(-\frac{\sqrt{-b f_{min}}}{a} (t + C_5) \right) \tag{163}$$

$$\dot{w}_{d5} = \frac{f_{min}}{a} \frac{1}{cos^2\left(-\frac{\sqrt{-b f_{min}}}{a} (t + C_5) \right)} \tag{164}$$

$$z_{d5} = \frac{a}{b} ln\left| cos\left(-\frac{\sqrt{-b f_{min}}}{a} (t + C_5) \right) \right| + C_6 \tag{165}$$

However, the constant C_5 and C_6 will be computed at time t_4 as formulated in (166) and (167).

$$C_5 = \frac{-a}{\sqrt{-bf_{min}}} arctan\left(\frac{w_4}{\sqrt{\frac{-f_{min}}{b}}}\right) - t_4 \tag{166}$$

$$C_6 = z_4 - \frac{a}{b} ln\left|cos\left(-\frac{\sqrt{-bf_{min}}}{a}(t_4 + C_5)\right)\right| \tag{167}$$

4.3. Time-optimal trajectory for depth motion

It is assumed that the buoyancy engine has the maximum force f_{max} and the thruster has the minimum force f_{min}. And the net buoyancy force generated by the buoyancy engine has the maximum rate c_{max} and the minimum rate c_{min}.

The solution of TOT trajectory for buoyancy engines and thrusters in the individual dynamics can be derived by solving the heave dynamics for t_1, t_2, t_3, t_4, t_5. In this system, $t_1 = t_0 + \frac{f_{max}}{c_{max}}$ and $t_4 - t_3 = \frac{f_{min}}{c_{min}}$ due to the delay of the buoyancy force. The given information is defined as $t_0 = 0$, $w_0 = 0$, $\dot{w}_0 = 0$, z_0, w_5, $\dot{w}_5$, z_5.

4.3.1 Find z_1, w_1 and $\dot{w}_1$

Some parameters should be defined as $p_1 = y_0(t_0)$; $p_2 = y_1(t_0)$; $p_3 = \dot{y}_0(t_0)$; $p_4 = \dot{y}_1(t_0)$; $p_5 = \ddot{y}_0(t_0)$; $p_6 = \ddot{y}_1(t_0)$; $q_1 = y_0(t_1)$; $q_2 = y_1(t_1)$; $q_3 = \dot{y}_0(t_1)$; $q_4 = \dot{y}_1(t_1)$; $q_5 = \ddot{y}_0(t_1)$; $q_6 = \ddot{y}_1(t_1)$; $l_1 = k_0(t_3 - t_4)$; $l_2 = k_1(t_3 - t_4)$; $l_3 = \dot{k}_0(t_3 - t_4)$; $l_4 = \dot{k}_1(t_3 - t_4)$; $l_5 = \ddot{k}_0(t_3 - t_4)$; $l_6 = \ddot{k}_1(t_3 - t_4)$; $h_1 = k_0(0)$; $h_2 = k_1(0)$; $h_3 = \dot{k}_0(0)$; $h_4 = \dot{k}_1(0)$; $h_5 = \ddot{k}_0(0)$; $h_6 = \ddot{k}_1(0)$; $t_3 - t_4 = \frac{f_{max}}{c_{min}}$.

$$\begin{cases} w_{d1}(t_0) = w_0 \\ \dot{w}_{d1}(t_0) = \dot{w}_0 \\ z_{d1}(t_0) = z_0 \end{cases}$$

$$\Leftrightarrow \begin{cases} \dot{y}_0(t_0) = 0 \\ \ddot{y}_0(t_0) = 0 \\ \frac{a}{b} ln|y(t_0)| + C_0 = z_0 \end{cases}$$

$$\Leftrightarrow \begin{cases} a_0 p_3 + a_1 p_4 = 0 \\ a_0 p_5 + a_1 p_6 = 0 \\ C_0 = z_0 - \frac{a}{b} \ln |a_0 p_1 + a_1 p_2| \end{cases} \tag{168}$$

$$\Leftrightarrow \begin{cases} a_1 = -\frac{p_3}{p_4} a_0 \\ a_0 p_5 + a_1 p_6 = 0 \\ C_0 = z_0 - \frac{a}{b} \ln |a_0 p_1 + a_1 p_2| \end{cases}$$

From the above, a set of constraints can be defined as (168) for the initial conditions of w_0, $\dot{w}_0$ and z_0. From this set, the constant C_0 can be found and the relationship of a_0 and a_1 can be established.

By initializing the arbitrary parameter, $a_0 = 0$, Eq. (120) can be solved as below.

$$a_1 = -\frac{p_3}{p_4} a_0 \tag{169}$$

$$C_0 = z_0 - \frac{a}{b} \ln |a_0 p_1 + a_1 p_2| \tag{170}$$

$$z_1 = \frac{a}{b} \ln|a_0 q_1 + a_1 q_2| + C_0 \tag{171}$$

$$w_1 = \frac{a}{b}\left(\frac{a_0 q_3 + a_1 q_4}{a_0 q_1 + a_1 q_2}\right) \tag{172}$$

$$\dot{w}_1 = \frac{a}{b}\left(\frac{a_0 q_5 + a_1 q_6}{a_0 q_1 + a_1 q_2} - \frac{(a_0 q_3 + a_1 q_4)^2}{(a_0 q_1 + a_1 q_2)^2}\right) \tag{173}$$

Once the first boundary is solved, then other unknowns can be easily calculated in the following steps from 4.3.2 to 4.3.3.

4.3.2 Find t_2, z_2, w_2 and $\dot{w}_2$

The boundary constants C_1 and C_2 can be calculated based on w_1 as above and the given time t_1.

$$C_1 = \frac{-a}{2\sqrt{b f_{max}}} ln\left(\frac{2\sqrt{f_{max}/b}}{w_1 + \sqrt{f_{max}/b}} - 1\right) - t_1 \tag{174}$$

$$C_2 = z_1 - \frac{a}{b} ln\left(1 + e^{\frac{2}{a}\sqrt{b f_{max}}(t_1 + C_1)}\right) + \sqrt{\frac{f_{max}}{b}}\, t_1 \tag{175}$$

Due to the non-zero argument in the logarithmic function, w_{2c} is defined as (176). And t_2 is computed in (177) using w_{2c} instead of w_2. The small error in this conversion is acceptable.

$$w_{2c} = \varepsilon\sqrt{\frac{f_{max}}{b}} \quad (\varepsilon \approx 1) \tag{176}$$

$$t_2 = t_{2c} = \frac{-a}{2\sqrt{b f_{max}}} ln\left(\frac{2\sqrt{f_{max}/b}}{w_{2c} + \sqrt{f_{max}/b}} - 1\right) - C_1 \tag{177}$$

Once the time t_2 is defined, all trajectories at the time t_2 can be organized as (178), (179) and (180).

$$z_2 = \frac{a}{b} ln\left(1 + e^{\frac{2}{a}\sqrt{bf_{max}}(t_{2c}+C_1)}\right) - \sqrt{\frac{f_{max}}{b}}\, t_{2c} + C_2 \tag{178}$$

$$w_2 = \frac{2\sqrt{f_{max}/b}}{1 + e^{\frac{2}{a}\sqrt{bf_{max}}(t_{2c}+C_1)}} - \sqrt{\frac{f_{max}}{b}} \tag{179}$$

$$\dot{w}_2 = \frac{4f_{max}}{a} \frac{e^{-\frac{2}{a}\sqrt{bf_{max}}(t_{2c}+C_1)}}{\left(1 + e^{-\frac{2}{a}\sqrt{bf_{max}}(t_{2c}+C_1)}\right)^2} \tag{180}$$

4.3.3 Find w_3, z_4 and w_4

It is noted that the trajectories of TOT cannot be solved in order from the first segment to the fifth segment. So, the trajectories in the fourth segment will be defined before the third and fifth segments. The constant C_3 is defined as (181) with the information of the second segment. And then, the constant velocity in the third segment can be computed as (182).

$$C_3 = z_2 - w_2 t_2 \tag{181}$$

$$w_3 = \sqrt{\frac{f_{max}}{b}} \tag{182}$$

The velocity at the time t_4 can be found as (183).

$$w_4 = \frac{-\frac{a}{b} l_3 + l_1 w_3}{l_4 - \frac{b}{a} l_2 w_3} \tag{183}$$

The position trajectory at the time t_4 is estimated by choosing the approximation of χ ($\chi \approx 0, \chi > 0$). The arbitrary constant n_0 and n_1 of the Airy solution in the function $k(t)$ can be estimated as (185) and (186).

$$\beta = \frac{b}{a} w_4 \tag{184}$$

$$n_0 = \frac{\sqrt{\chi}}{\sqrt{l_1 l_5 + \beta l_2 l_5 + \beta l_1 l_6 + \beta^2 l_2 l_6 - l_3^2 - \beta^2 l_4^2 - 2\beta l_3 l_4}} \tag{185}$$
$$(\chi \approx 0, \chi > 0)$$

$$n_1 = \beta n_0 \tag{186}$$

Next, the distance from t_3 to t_4 can be computed as (187).

$$\Delta z_{43} = \frac{a}{b} ln \left| \frac{n_0 h_1 + n_1 h_2}{n_0 l_1 + n_1 l_2} \right| \tag{187}$$

And the distance from t_4 to t_5 can be calculated as (188).

$$\Delta z_{54} = \frac{a}{b} ln \sqrt{1 - \frac{w_4^2}{f_{min}/b}} \tag{188}$$

Finally, the position trajectory at the time t_4 can be defined as (189) based on the distance Δz_{54}.

$$z_4 = z_5 - \Delta z_{54} \tag{189}$$

4.3.4 Find z_3, t_3 and t_4

Once z_4 is known, the constant C_4 and the position at the time t_3 can be computed as (190) and (191).

$$C_4 = z_4 - ln|n_0 h_1 + n_1 h_2| \tag{190}$$

$$z_3 = \frac{a}{b} ln|n_0 l_1 + n_1 l_2| + C_4 \tag{191}$$

And the time t_3 can be found as (192) based on z_3 and C_3.

$$t_3 = \frac{z_3 - C_3}{w_3} \tag{192}$$

Then, the time t_4 is equal to the summation of the time t_3 and the delay of the buoyancy engine, as shown in (193).

$$t_4 = t_3 + \frac{f_{max}}{c_{max}} \tag{193}$$

4.3.5 Find α and t_5

The constant delay α in the fourth segment can be defined as (194) using the time t_3. And finally, the time t_5 can be computed based on the boundary constant C_5, as shown in (195) and (197).

$$\alpha = t_3 - \frac{f_{max}}{c_{min}} \tag{194}$$

$$C_5 = \frac{-a}{\sqrt{-bf_{min_3}}}\ arctan\left(\frac{w_4}{\sqrt{-f_{min}/b}}\right) - t_4 \tag{195}$$

$$C_6 = z_5 \tag{196}$$

$$t_5 = -C_5 \tag{197}$$

The time t_2, t_3, t_4 and t_5 of TOT trajectory are shown in (177), (192), (193) and (197). Therefore, if the reference for depth control is designed as the TOT trajectory, the control input will be the same as the input design in Fig. 26.

4.4. Sliding mode control for heave dynamics

The heave dynamics is recalled as

$$a\dot{w} + b|w|w = u + d$$
$$\dot{z} = w \tag{198}$$

where u is the control input, d is the bounded disturbance. In the control design, the hydrodynamic coefficients of the heave dynamics are assumed to be known. Therefore, the controller just deals with the bounded disturbance d. A sliding mode control will be designed for the heave dynamics using saturation function as below.

The sliding surface s is constructed as (199), a function of depth error and heave velocity error. Here, λ is the positive weight between position and velocity error.

$$s = (w - w_d) + \lambda(z - z_d) \tag{199}$$

The control law for u can be described as

$$u = \hat{b}w|w| + \hat{a}\dot{w}_d - \lambda\hat{a}(w - w_d) - Ksat\left(\frac{s}{\phi}\right) \tag{200}$$

where $\hat{a}$ and $\hat{b}$ are the parameter estimation for a and b, ϕ is the boundary layer for sliding surface and K can be design as

$$K = \Delta_b w^2 + \Delta_a|\dot{w}_d - \lambda(w - w_d)| + D + \eta a_{max} \tag{201}$$

where Δ_a is the magnitude of uncertainty of parameter a, Δ_b is the magnitude of uncertainty of parameter b, D is the bound of the external disturbance d, η is a small positive scalar, and a_{max} is the possible maximum of a.

With the above SMC, the tracking control of TOT can be robust to the external bounded disturbance. In the next simulation, the TOT and SMC will be combined to verify the tracking performance.

4.5. Computer simulation

The main purpose of this simulation is to verify the TOT trajectory and its control input. Therefore, it is assumed that the parameters of pure depth plant are perfectly known. Here, $a = 50.5\text{kg}$; $b = 10\text{kg}$; $f_{max} = 3.43\text{N}$ (net buoyancy force); $f_{min} = -10\text{N}$ (including the resulting force composed by thruster force and pitch angle). One more important parameter of buoyancy engine is the rate of buoyancy force $c_{max} = -c_{min} = \frac{f_{max}}{20}\text{N/s}$, then the period for reaching the maximum force from zero is 20s. For further observation, the disturbance can be added into dynamics as $d = 0.2\sin(\frac{2t}{\pi})$. This disturbance can be used to verify that the control input for the TOT trajectory can oscillate around the predefined input with the same amount of disturbance magnitude. The sliding mode control using saturation function is used in this depth control simulation. The detailed design of this controller is similar to the previous chapter.

4.5.1. Simulation 1

The desired depth is set from the water surface to 40m, so $z_0 = 0$ and $z_5 = 40\text{m}$. To find the profile of the TOT trajectory, Eq. (177), (192), (193) and (197) are used to find t_2, t_3, t_4 and t_5 respectively. In this simulation, $\text{t}_2 = 63.5238$, $\text{t}_3 = 66.1899$, $\text{t}_4 = 86.1899$ and $\text{t}_5 = 87.7597$.

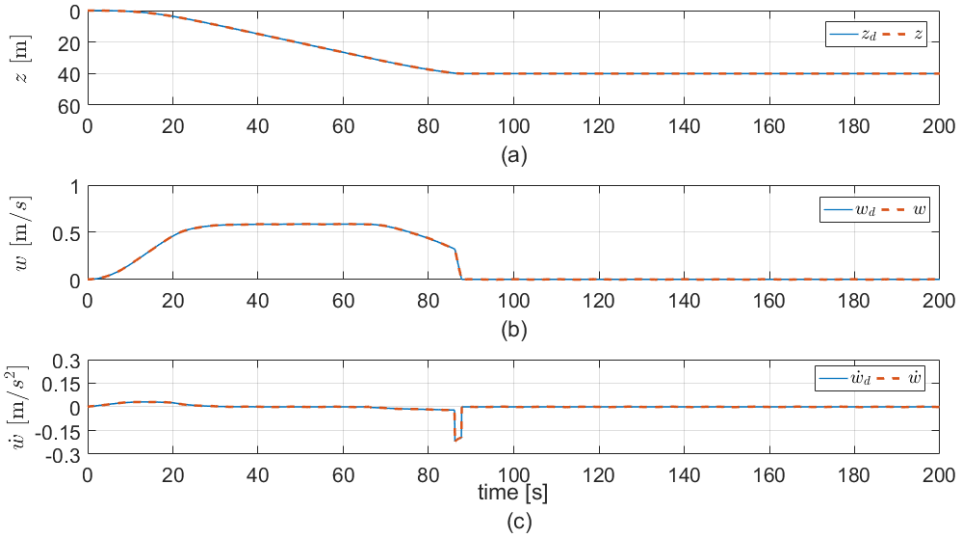

Fig. 27 Tracking performance of TOT trajectory without disturbance

In Fig. 27, the actual value of the position, velocity and acceleration track the TOT trajectory very well. The heave velocity reaches the maximum value of 0.587m/s at t_2 in Fig. 27b. The heave acceleration rose from 0 to 0.031m/s^2 and then dropped to 0m/s at t_2. From t_2 to t_4, the net buoyancy force will decrease to zero to make the vehicle become neutrally buoyant, and the thruster will be used from t_4 to t_5. The buoyancy force decreases from 3.43N to 0N in 20s, this change reduces the heave velocity to 0.32m/s and the heave acceleration to -0.22m/s^2. The duty of the thruster is to bring the velocity and acceleration to zero at $t_5$in Fig. 27b and c. Finally, the control input of the thruster will be kept at zero after a very short time operation in Fig. 29b. At this time, the depth of the vehicle is controlled at 40m with the minimum time of 87.8s using 3.43N buoyancy force and -10N thrust. The designer can use this simulation for checking their capacity design of the buoyancy engine and thruster force whether the settling time is satisfied the requirements.

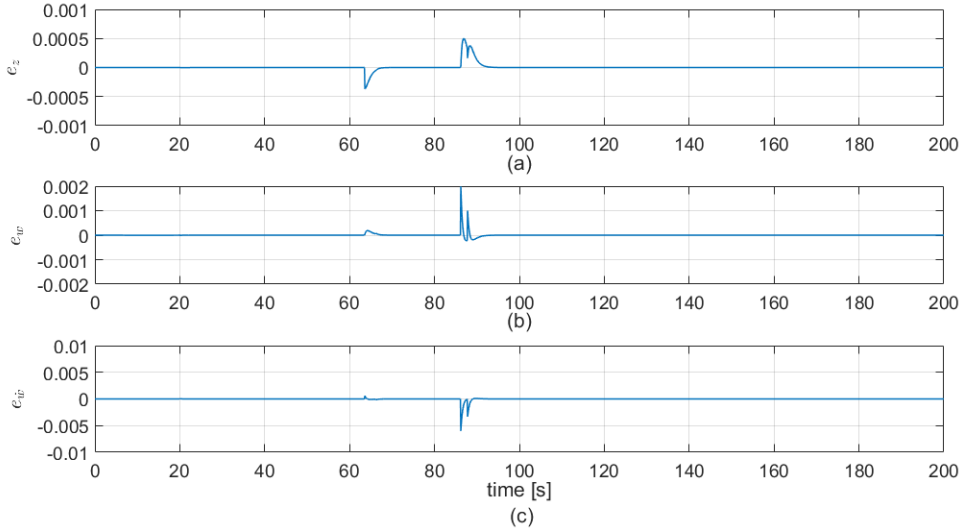

Fig. 28 Tracking error without disturbance in position, velocity and acceleration

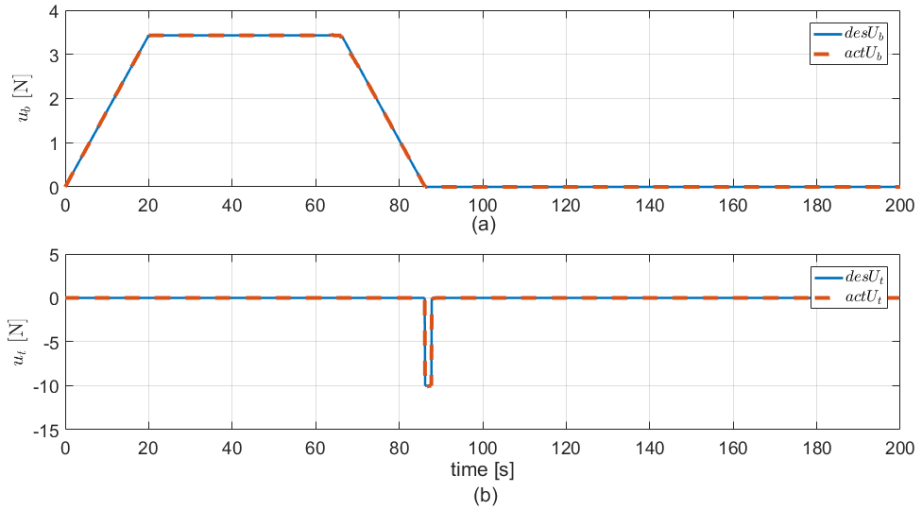

Fig. 29 Control input for TOT trajectory in the depth control without disturbance

The sharp change in acceleration and velocity causes the tracking error increase from t_4 to t_5. The tracking errors rose to 5×10^{-4}m in the position error, 2×10^{-3} m/s in the velocity error and -6×10^{-3} m/s^2 in the

acceleration error. And then, all errors remain at zero at the end of the TOT trajectory in Fig. 28.

The actual control input is the same as the pre-design input in Fig. 29. If the parameters of heave dynamics are the same as the actual system, then the control input using TOT trajectory will be kept under the limit of the buoyancy engines and thrusters. While fully using the maximum force of the buoyancy engines and thrusters, the shortest arrival time of depth control can be achieved.

4.5.2. Simulation 2

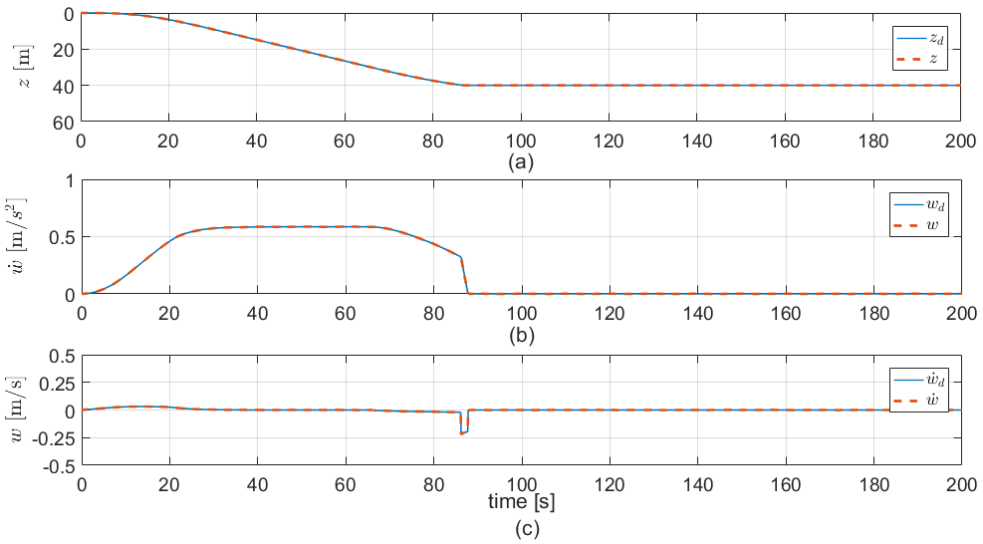

Fig. 30 Tracking performance of TOT trajectory with disturbance

The disturbance $d = 0.2\sin(\frac{2t}{\pi})$ with waveform is added into the heave dynamics. The tracking performance of the TOT trajectory is still good in Fig. 30. However, the tracking error is degraded due to the saturation function in sliding mode control for chattering elimination. The position error is kept under 0.002m, the velocity error is controlled under 0.002m/s and the acceleration error is under 0.006m/s2.

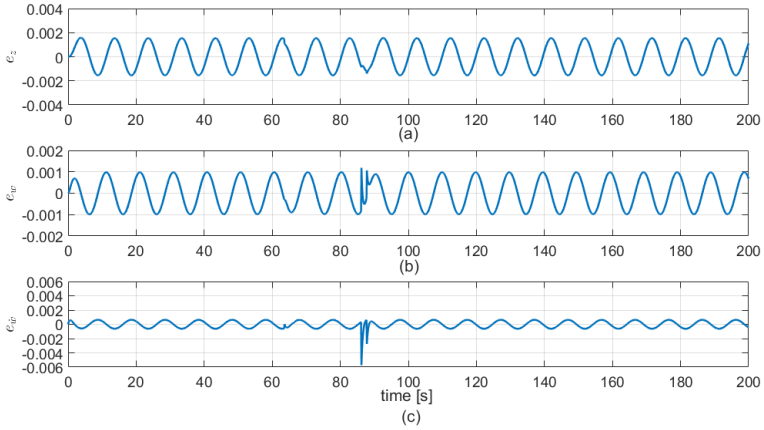

Fig. 31 Tracking error with disturbance in position, velocity and acceleration

The most important result is shown in Fig. 32. Due to the disturbance, the control input oscillated around the pre-defined input for TOT trajectory. And the deviation of the actual input is equal to the magnitude of the disturbance. In this simulation, the buoyancy force oscillated from 3.22N to 3.64N while the desired input is 3.43N in Fig. 32a. The average value of actual buoyancy force can be estimated as 3.43N, which is the same as pre-defined input, and the buoyancy force has a deviation of 0.2N, which is equal to the magnitude of disturbance $d = 0.2\sin(\frac{2t}{\pi})$. The same phenomenon can be observed in Fig. 32b for the thrust force after completing the TOT trajectory.

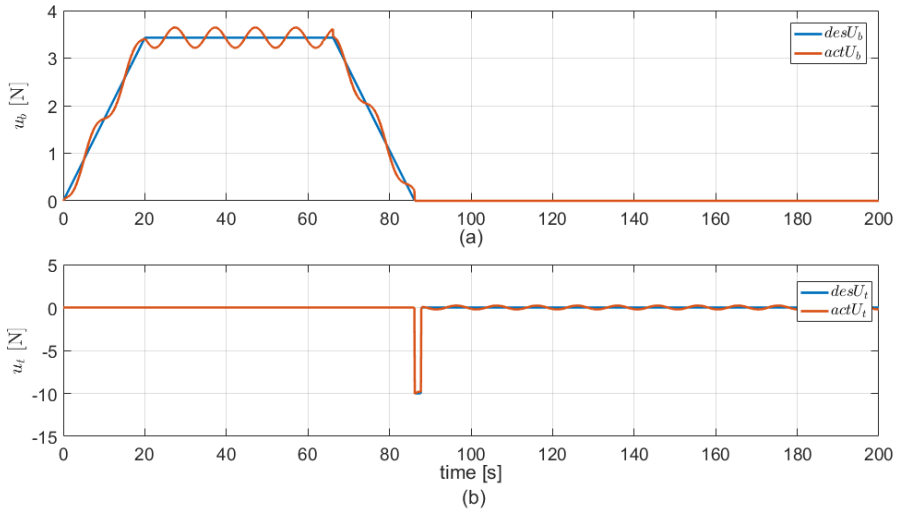

Fig. 32 Control inputs for TOT trajectory with disturbance effect

A robust depth control algorithm with the proposed TOT was studied and simulated with a good tracking performance under the external bounded disturbances. The robust action from sliding mode control using saturation function can keep the tracking error very small in the presence of disturbances. The control effort can track the designated input very well under the disturbance. And the magnitude of the deviation in the control effort is equal to the bound of the disturbance.

Chapter 5. Experimental study of direct adaptive control along TOT for heading motion

5.1. Motivation

In the real world, the parameter and its uncertainty bound cannot be estimated exactly as in the previous assumption. Therefore, another powerful controller should be investigated for further improvement in TOT tracking control. In this chapter, the robust adaptive control will be presented under the assumption that there are unknown parameters and bounded external disturbances.

The weakness of sliding mode control was that the real parameters of the system should be in the pre-defined bounds. If the real parameters are not in these bounds, the stability of the dynamics with sliding mode control cannot be preserved. Especially, for the underwater vehicle model, the hydrodynamics coefficients cannot be estimated correctly, and then the pre-defined bounds should be increased with trials and errors. Therefore, control gains of the sign or saturation function should be increased following the increase of the parameter bounds. This point makes sliding mode control unsuitable for control application of an underwater vehicle.

On the other hand, the adaptive control is stable for all dynamics with the structured model. For this reason, the experimental study of TOT trajectory using robust adaptive control will be carried out for heading control of the developed RHUG in this chapter.

5.2. Composition of RHUG

Fig. 33 Side view of the developed RHUG

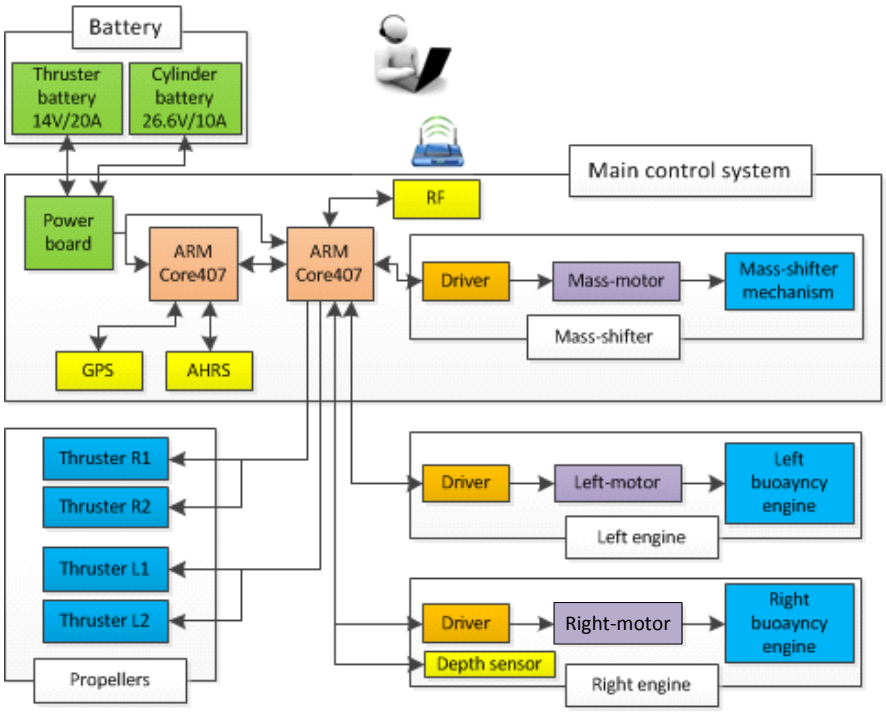

Fig. 34 Hardware diagram of RHUG

The RHUG in Fig. 33 will be used for the TOT trajectory experiment. The control processors are ARM Core407 boards, as shown in Fig. 34. The power systems are developed with two batteries of 14V/20A and 26.6V/10A for thrusters and motors respectively. The power board will distribute 5V to

MCUs, GPS, AHRS, and RF module. The motors from the mass-shifter, left buoyancy, and right buoyancy blocks will use the voltage of 26.6V from the batteries. The depth sensor also uses 26.6V directly from the batteries. The thrusters are fed by 14V power directly from the batteries. Therefore, only one DC-DC board required for this structure is from 26.6V to 5V.

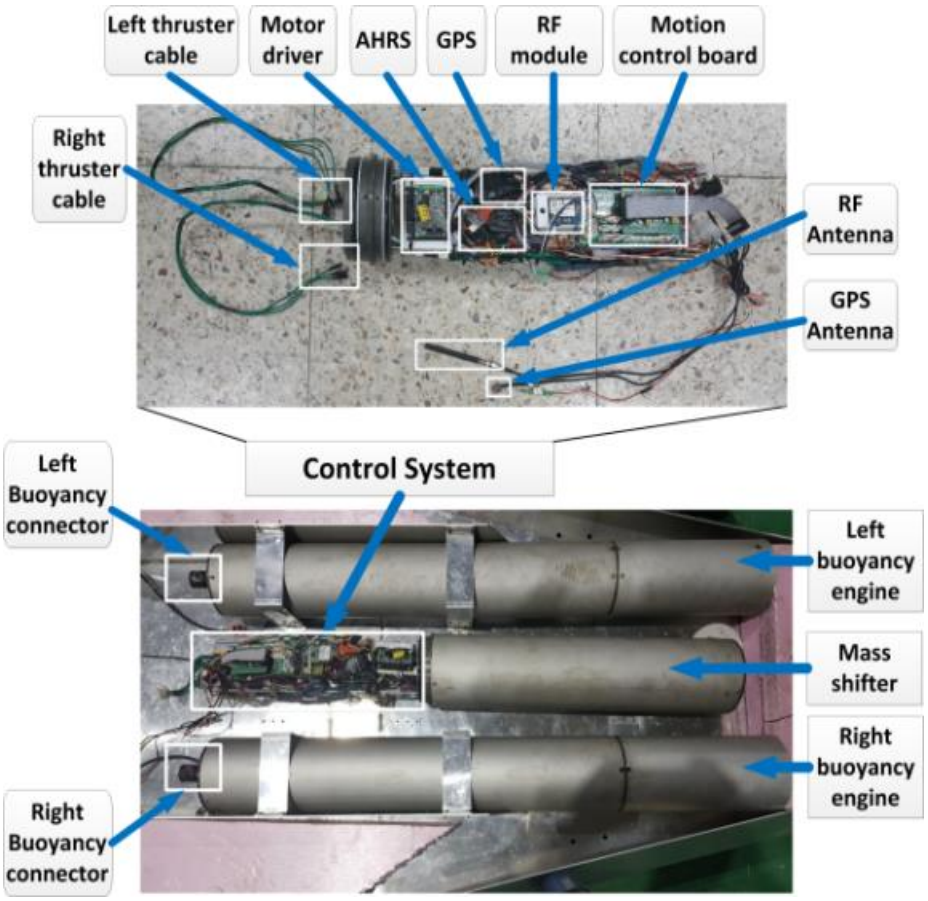

Fig. 35 Hardware design of the developed RHUG

In Fig. 35, three blocks are shown inside the covers of the vehicle. Two side blocks are the left and right buoyancy engines, which will compress and enlarge the volume of the air inside the cylinders. The middle block contains the control system and the moving mass in the mass-shifter mechanism. In the control system, its components are GPS, AHRS, RF module, motion

control board, navigation board, RF antenna, GPS antenna, motor driver, and thruster ESCs (electronic speed controller). The mechanical components of the mass-shifter and buoyancy engine are shown in Fig. 36 and Fig. 37 respectively.

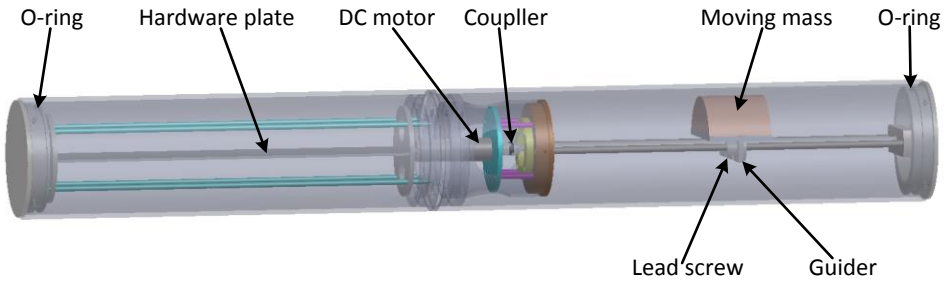

Fig. 36 Mass-shifter design

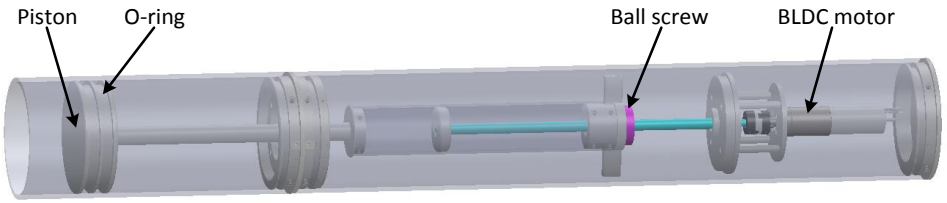

Fig. 37 Buoyancy engine design

The control diagram of RHUG is shown in Fig. 38 with three sub-controllers which are heading control, pitching control and glide up/down. The controller for the heading is adaptive control, as shown in Fig. 39, for the unknown parameters of heading dynamics. The glide up/down controller is used for the purpose of descending and ascending with two buoyancy engines. And the pitching control is used for regulating the pitch angle using a moving mass inside the mass-shifter block.

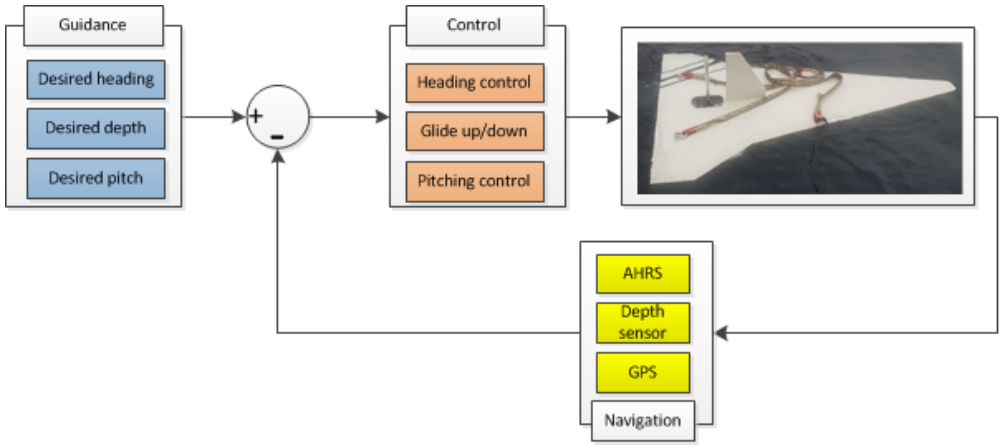

Fig. 38 The control diagram of RHUG

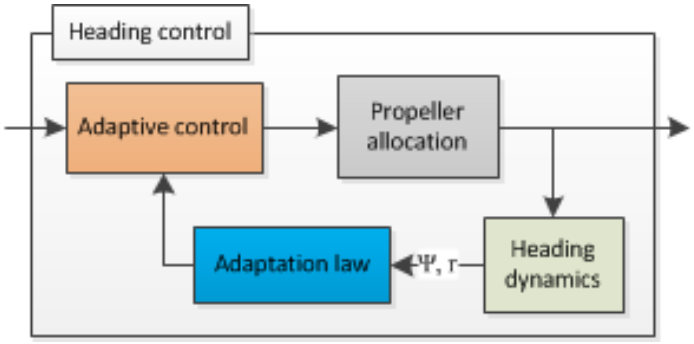

Fig. 39 Adaptive heading control

The adaptive control will calculate the required torque and feed to the propeller allocation system. Due to the fast response of thrusters, the static thruster model is used for torque allocation. Using the static model in (11), the input signal of the thruster with the required torque can be computed easily with three linear functions. The AHRS sensor will be used to measure the heading angle ψ and the yaw rate r. The heading adaptive control and adaptation in Fig. 39 will be explained in the next subsection.

5.3. Robust adaptive control for heading dynamics

The heading dynamics of RHUG can be written as

$$\begin{aligned} \dot{\psi} &= r \\ (I_{zz} - N_{\dot{r}})\dot{r} &= N_r r + N_{|r|r}|r|r + \tau_r + d \end{aligned} \tag{202}$$

where τ_r is the control input, d is the disturbance with zero-mean waveform. The heading error and yaw rate error can be defined as

$$e_1 = \psi - \psi_d \tag{203}$$

$$e_2 = r - r_d \tag{204}$$

The sliding surface s can be designed as

$$s = e_2 + \lambda e_1 \tag{205}$$

where λ is the weight between two errors, e_1 and e_2. The Lyapunov function is choosen as

$$V_2 = \frac{1}{2} a s^2 + \frac{1}{2} \tilde{a}_2^T P_2^{-1} \tilde{a}_2 \tag{206}$$

where $a = I_{zz} - N_{\dot{r}} > 0$; $\tilde{a}_2 = \hat{a}_2 - a_2$ is the estimation error of system parameter, and P_2 is a positive diagonal matrix. Then, the derivative of V_2 can be expanded as

$$\dot{V}_2 = as(\dot{e}_2 + \lambda \dot{e}_1) + \hat{a}_2^T P_2^{-1} \tilde{a}_2 \tag{207}$$

The error dynamics in the derivative of Lyapunov function can be replaced by the heading dynamics and it can be rewritten as

$$\dot{V}_2 = s\left(-br - cr|r| + a\left(\ddot{\psi}_d + \lambda e_2\right) + d + \tau_r\right) + \hat{a}_2^T P_2^{-1} \tilde{a}_2 \tag{208}$$

where $b = N_r$, $c = N_{r|r|}$. The dynamics in $\dot{V}_2$ can be linearly parameterized as

$$Y_2 a_2 = -br - cr|r| + a\left(\ddot{\psi}_d + \lambda e_2\right) \tag{209}$$

where $Y_2 = [r \quad r|r| \quad \ddot{\psi}_d + \lambda e_2]$ and $a_2 = [-b \quad -c \quad a]^T$. The derivative of the Lyapunov function can be rewritten as

$$\dot{V}_2 = s(Y_2 a_2 + d + \tau_r) + \hat{a}_2^T P_2^{-1} \tilde{a}_2 \tag{210}$$

Therefore, the control input τ_r canbe designed as

$$\tau_r = -Y_2 \hat{a}_2 - \hat{d} - k_3 s - k_4 sat\left(\frac{s}{\phi}\right) \tag{211}$$

where $\hat{d}$ is the mean of the external disturbance and it is zero, k_3 is the positive gain for sliding surface, k_4 is the gain for the saturation function and should be design later. By substituting τ_r into $\dot{V}_2$, the derivative of Lyapunov function can be obtained as

$$\dot{V}_2 = -k_3 s^2 + s Y_2 \tilde{a}_2 + \left(d - \hat{d}\right) - k_4 sat\left(\tfrac{s}{\phi}\right) + \hat{a}_2^T P_2^{-1} \tilde{a}_2 \tag{212}$$

From here, the adaptation law can be formulated as

$$\dot{\hat{a}}_2 = -P_2^T Y_2^T s \tag{213}$$

With this adaptation law, the relating equation of $\dot{V}_2$ can be obtained as

$$\dot{V}_2 \leq -k_3 s^2 + \left|d - \hat{d}\right| - k_4 sat\left(\frac{s}{\phi}\right) \tag{214}$$

To make the right-hand side negative definite, the control gain k_4 should be designed as

$$k_4 \geq \left|d - \hat{d}\right| + \eta \tag{215}$$

where η is a small positive scalar. Using the condition in (215), one can prove that the derivative of Lyapunov function V_2 is negative definite (N.D), as shown in (216).

$$\dot{V}_2 \leq -k_3 s^2 \tag{216}$$

5.4. Computer simulation

In Fig. 40, the performance of TOT tracking control is quite good with reasonable tracking error. The dashed blue line is the actual heading angle, and the solid red line is the TOT trajectory. And the zero convergence is achieved for both position and velocity graphs. The overshoot in position tracking control using adaptive control can be adjusted by tuning the control gain k_1. The smaller the control gain k_1 is, the smaller the position overshoot will be.

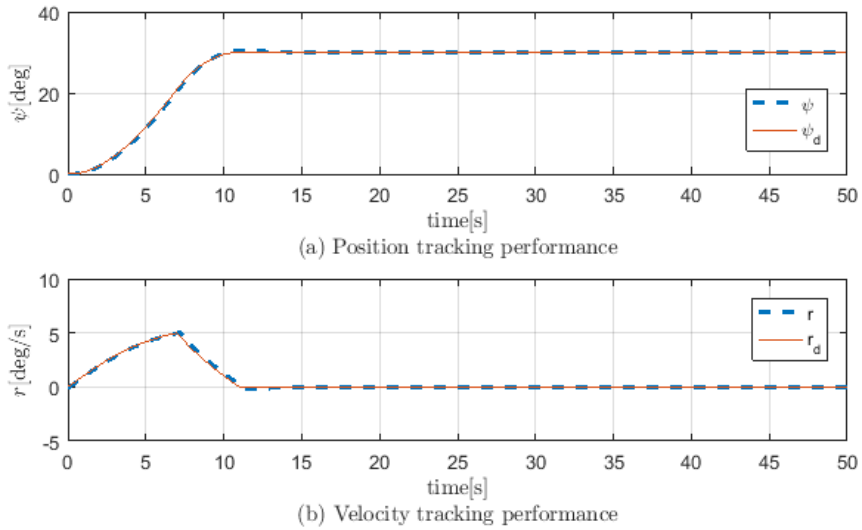

(a) Position tracking performance

(b) Velocity tracking performance

Fig. 40 Performance of TOT trajectory with adaptive control

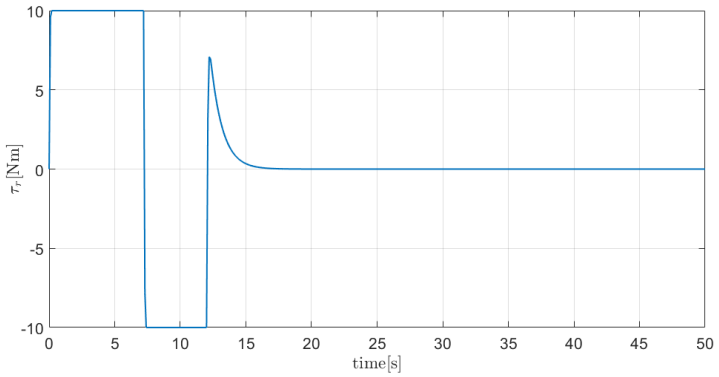

Fig. 41 Control input for TOT trajectory

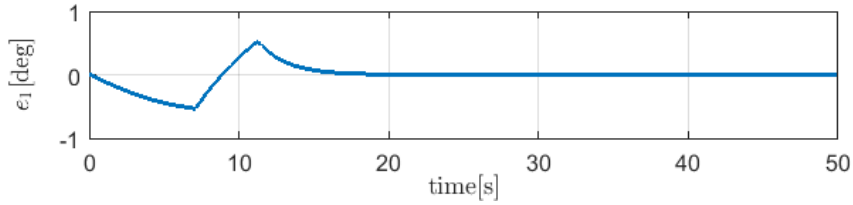

(a) Position error

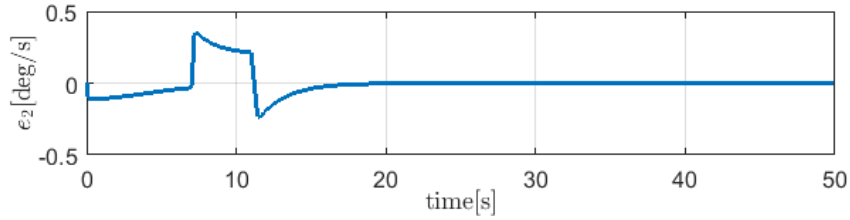

(b) Velocity error

Fig. 42 Tracking error of adaptive control

With the TOT concept in chapter 2, the control input will use maximum force and then minimum force. This concept is similar to Fig. 41, but the control input of adaptive control is much smoother than the sliding mode control, and it can operate without the knowledge of parameter bounds. But sliding mode control will need the bounds of all parameters, and chattering problem should be managed well.

Moreover, the bigger the parameter bounds are, the larger the control input of SMC will be. Therefore, the saturation of the actuator in SMC should be calculated well so that it does not exceed the actual input limit. And it is still undergoing research of many control designers nowadays. This adaptive control showed that the control input is in the range of pre-defined bounds between -10Nm to 10Nm while tracking the TOT trajectory.

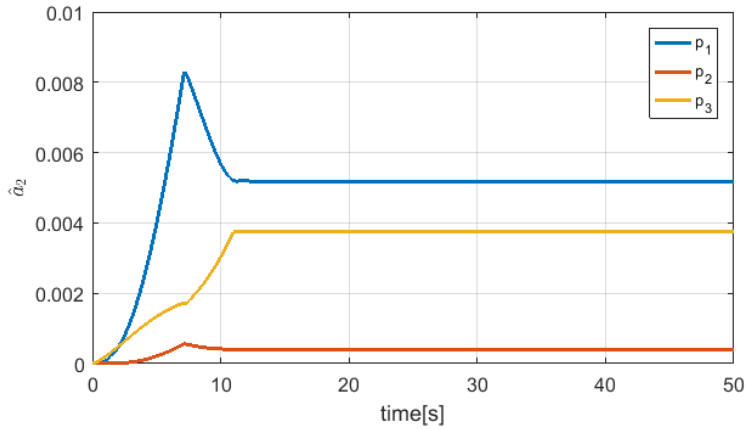

Fig. 43 Parameter adaptation

The tracking error has the good zero convergence as shown in Fig. 42 for both position and velocity errors. The tracking error in Fig. 42 is much bigger than that of Fig. 23, but it is accepted with 1 deg and 0.5 deg/s for position and velocity tracking error respectively. After the TOT trajectory, the tracking errors are converged to zero.

Finally, the zero convergence can be verified again by the parameter adaptation in Fig. 43. Three estimated parameters are constant as time tends to infinity. It is noted that the first and second parameters are used in the nonlinear hydrodynamic term, and the third parameter is the inertia term.

This adaptive heading control will be applied to the real platform of RHUG with the same control law and adaptation. And the TOT trajectory is also tested in this platform with the heading parameters of REMUS. Here, $N_{\dot{r}} = -4.88kgm^2/rad$; $N_r = 0$; $N_{rr} = -94kgm^2/rad^2$; $I_{zz} = 50kgm^2$; $-10Nm \leq \tau_r \leq 10Nm$. The next subsection will show the heading experiment and the tuning process of adaptive control gains.

5.5 Experiment

5.5.1 First experiment with $k_1 = 2.5, k_2 = 30$

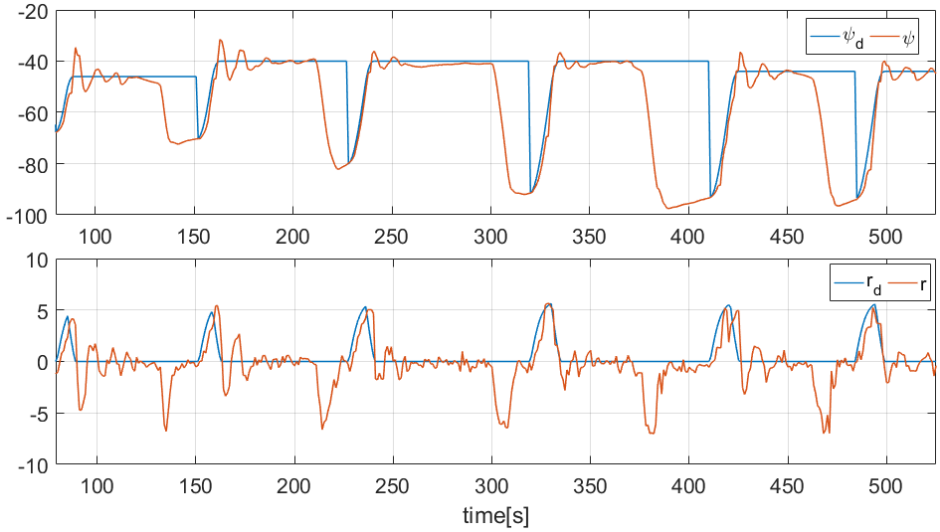

Fig. 44 TOT tracking performance in the first experiment

The vehicle was tested in a swimming pool, and the goal of the experiment was to find the best control gains for TOT tracking controller. The vehicle will be released at around $-80°$, and the TOT was fed to the adaptive controller with the desired heading angle of $-40°$ and $-44°$. After six times of testing, the result is shown in Fig. 44 and Fig. 45.

The control gains for the first experiment will be defined as $k_1 = 2.5, k_2 = 30$. The tracking performance of TOT with these gains is shown in Fig. 44. With this value of k_1, the controller has a good tracking performance with the TOT. But after finishing the TOT trajectory, the oscillating phenomenon appeared with a big overshoot in position performance. This phenomenon can be also observed in the control input τ_r in Fig. 45. This problem is caused by the big gain of k_1, so in the next experiment the control gain k_1 was decreased but keeping the value of k_2.

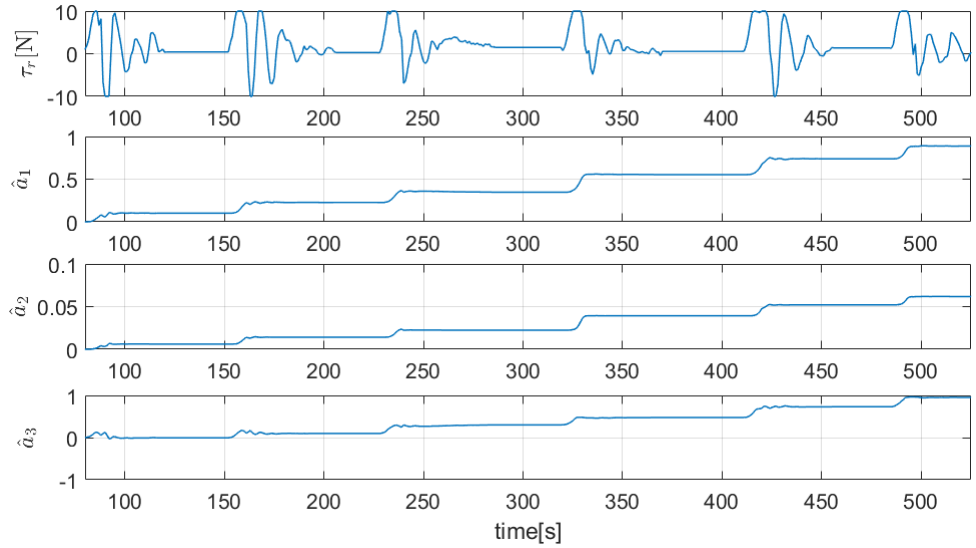

Fig. 45 Control inputs and parameter adaptation in the first experiment

The estimated parameters of the adaptation law can be seen in Fig. 45. Despite the oscillating response in position tracking, the estimation still can achieve constant values after tracking the TOT trajectory.

5.5.2 Second experiment with $k_1 = 2, k_2 = 30$

It was similar to the previous test, the desired heading angle is set at $-44°$. The heading control is tested four times in the swimming pool. The result of this second test is shown in Fig. 46 and Fig. 47.

The control gain k_1 was decreased to 2 instead of 2.5 in the first experiment. And the improvement can be seen in Fig. 46 with a small overshoot and damped oscillating tracking. However, the actual curve is quite slower than the TOT trajectory. Then another change of control gains should be decided. And to make the tracking performance better, the control gain k_2 should be increased dramatically.

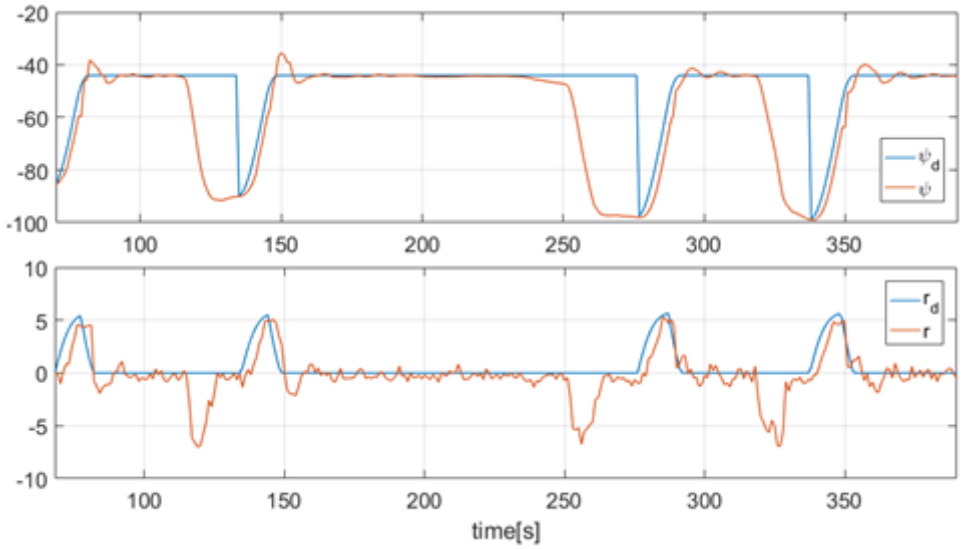

Fig. 46 TOT tracking performance in the second experiment

In Fig. 47, the control input and adaptation of the second experiment is presented. After reducing k_1, the better steady state performance can be observed in the control input. At first, the control input will be increase to the maximum value, 10Nm. When the actual heading gets near to the final desired angle, the control input significantly decreases near to the minimum value of -10Nm. And when the TOT trajectory reaches the desired angle, the control input oscillates around the zero point.

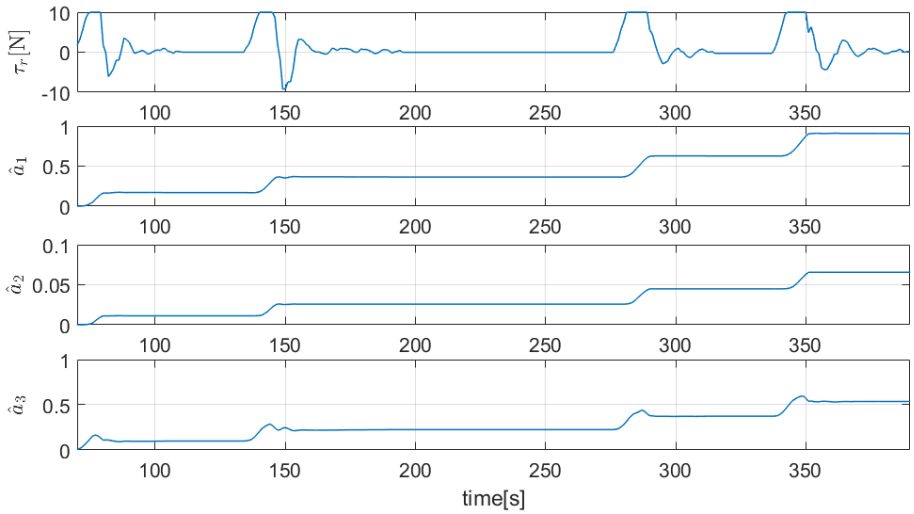

Fig. 47 Control inputs and parameter adaptation in the second experiment

The estimated parameters are shown in Fig. 47. The parameter changed to the constant value four times representing four tests of heading control. This figure showed that with these control gains, the system has a good zero convergence.

5.5.3 Third experiment with $k_1 = 2, k_2 = 50$

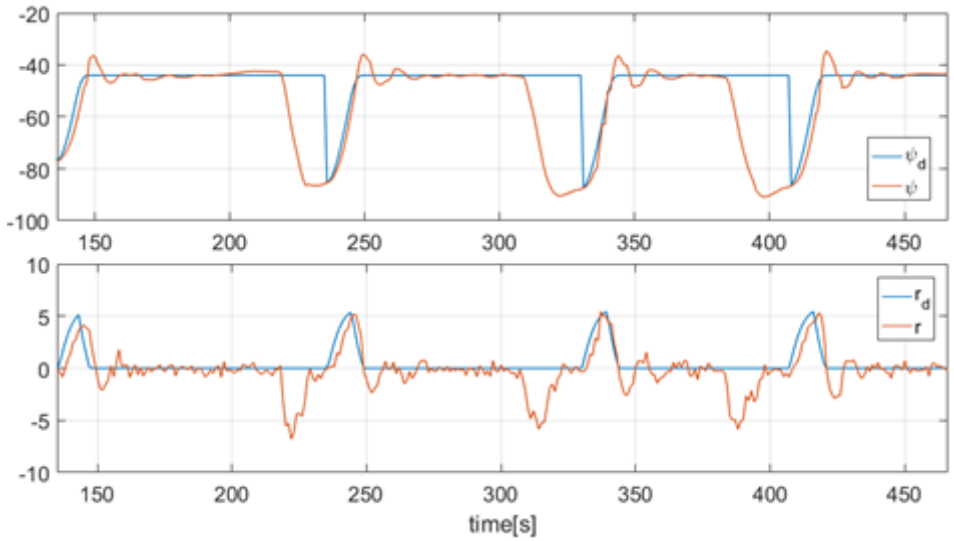

Fig. 48 TOT tracking performance in the third experiment

In the third test, the condition was set as the same as the second test except that k_2 is set at 50. The desired heading angle is $-44°$ and the initial angle is around $-80°$. The heading control was also conducted four times. The result of the third test is shown in Fig. 48 and Fig. 49.

In Fig. 48, the tracking performance is better than the second experiment, but the overshoot of the third test is bigger than that of the second test. However, this overshoot is damped quickly, and it has better tracking compared to the second test. Moreover, the control input in this experiment is

better than that of the first experiment. Therefore, the final gain is chosen as the same as the second experiment.

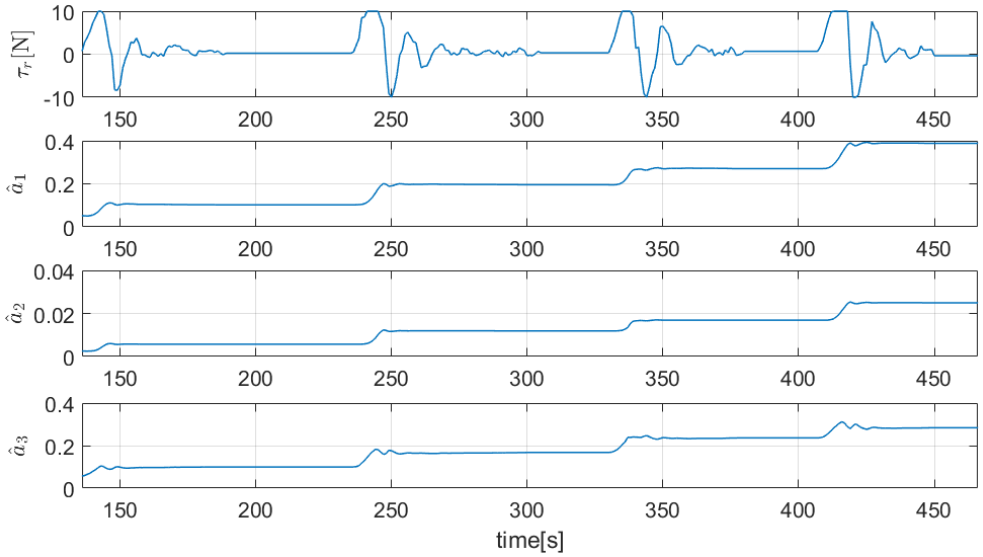

Fig. 49 Control inputs and parameter adaptation in the third experiment

To confirm the good performance of the final control gains, one more test was conducted with the desired heading angle of $-44°$, and the result is shown in Fig. 50 and Fig. 51. The blue line is the TOT trajectory, and the red line is the actual heading angle. The overshoot of this experiment is about $8°$, and it is quickly damped to zero. Both position and velocity have reasonable tracking errors.

The control input is the first curve in Fig. 51. It rises to a maximum value and then decreases to the minimum value before settling around zero. The control input is not perfectly rectangular as the TOT concept due to the parameters used to design the TOT trajectory may not be the true values of the tested platform. However, the control input using the adaptive control is much smoother than that of the SMC control. Before going to zero, the control input has a significant rise due to the overshoot in the position tracking.

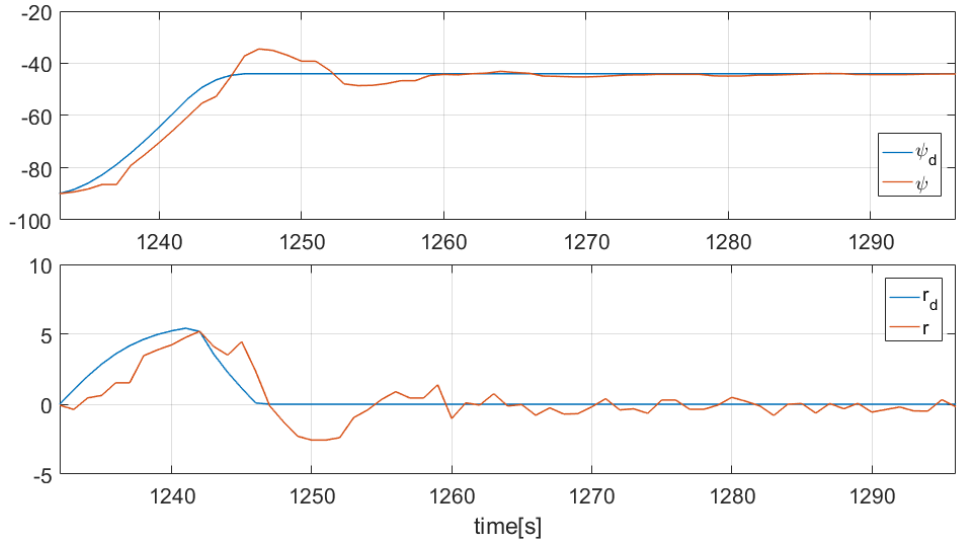

Fig. 50 TOT trajectory performance with final gains

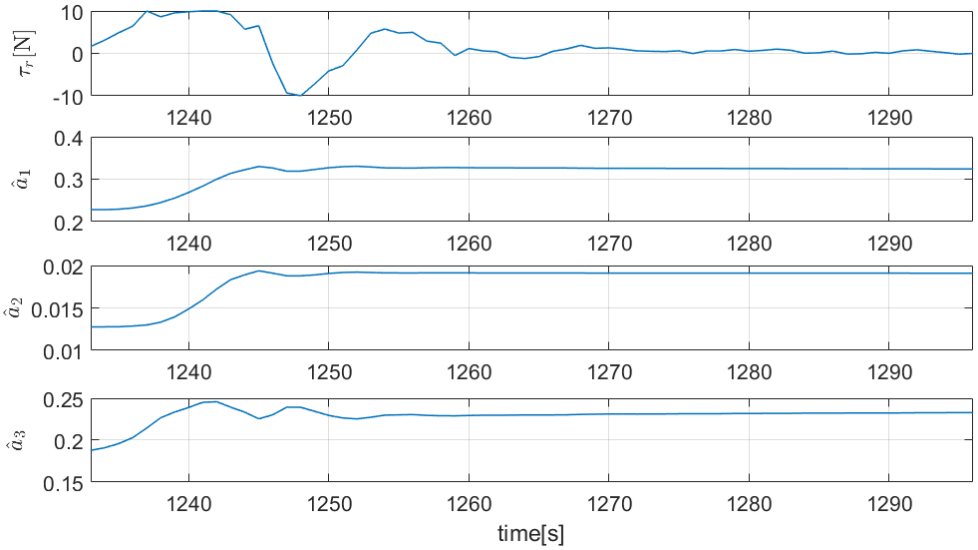

Fig. 51 Control input and parameter estimation with final gains

Three estimations are presented in Fig. 51. And the estimated parameters also have a good convergence to the constant value. Here, $\hat{a}_1$ represents the parameter N_r, $\hat{a}_2$ is the estimation of the parameter $N_{|r|r}$, and $\hat{a}_3$ means the inertial term $(I_{zz} - N_{\dot{r}})$. They did not converge to the true value because of the richness of the reference. In adaptive control theory, if the reference for

the adaptive control has adequate richness, the estimated parameter will converge to the true parameter. And to solve this problem, there are many undergoing studies about the learning-based adaptive control for finding the true parameters.

In this work, the TOT trajectory for the heading dynamics is successfully tested using the adaptive control technique. Smoother control input is realized in this experiment compared to chapter three. And the implementation of TOT trajectory using this adaptive control did not require knowledge about the bounds of parameters while the SMC control needs that information in advance to design the control law. Therefore, with the TOT trajectory, the adaptive control is better than the SMC control in the practical aspect.

Chapter 6. Robust adaptive control design for vertical motion

6.1. Dynamics of vertical plane

The vertical dynamics can be rewritten as (217). The definition of variables and parameters can be seen in subsection 2.3.

$$
\begin{aligned}
&\dot{x} = u\cos\theta + w\sin\theta \\
&\dot{z} = -u\sin\theta + w\cos\theta \\
&\dot{\theta} = q \\
(m - X_{\dot{u}})\dot{u} &= -mz_g\dot{q} + mx_g q^2 - mwq + Z_{\dot{w}}wq + X_{uu}u^2 \\
&\quad + X_{ww}w^2 + X_{uw}uw - (W - B)\sin\theta + \tau_w\sin\theta \\
&\quad + \tau_u + \tau_{eu} \\
(m - Z_{\dot{w}})\dot{w} &= \left(mx_g + Z_{\dot{q}}\right)\dot{q} + mz_g q^2 + muq - X_{\dot{u}}uq + Z_{uu}u^2 \\
&\quad + Z_{uw}uw + Z_{ww}w^2 + Z_{www}w^3 + (W - B)\cos\theta \\
&\quad + \tau_w\cos\theta + \tau_{ew} \\
\left(I_{yy} - M_{\dot{q}}\right)\dot{q} &= -mz_g\dot{u} + \left(mx_g - M_{\dot{w}}\right)\dot{w} - mz_g qw - Z_{\dot{w}}wu \\
&\quad - Z_{\dot{q}}qu + X_{\dot{u}}uw + M_{uu}u^2 + M_{uw}uw + M_{ww}w^2 \\
&\quad + M_{www}w^3 - \left(z_g W - z_b B\right)\sin\theta \\
&\quad - \left(x_g - x_b B\right)\cos\theta + \tau_q + \tau_{eq}
\end{aligned}
\tag{217}
$$

The vertical motion is extremely important for the RHUG system because the gliding motion is the key technology of this system. These dynamics including surge, heave, and pitching motions can be rewritten as (217). For

the glider system, the parameters of the dynamics cannot be estimated exactly, and some parameters cannot be measured directly, such as the center of buoyancy and gravity, and moment of inertia. Moreover, those parameters can be changed during the operation of the buoyancy engines and moving mass in Eq. (15), (16) and (18). Therefore, the adaptation law should be designed to overcome the parameter change in this system. RHUG system is strongly influenced by environmental disturbances such as waves and currents. Hence, a robust control technique should be applied to this controller.

There have been many studies on adaptive control for underwater vehicles over the last two decades. However, only a few authors could perform adaptive control with good experimental results. The bound-estimation adaptive control was developed in [54], and the experiment result of depth control was presented with reasonable tracking error. The position and heading adaptive PD control were applied to an ROV system in [55], and the superior performance was presented in adaptive PD control over the conventional PD control under the uncertainties of cable forces and mechanical connection between the ROV and underwater structure. In these two papers, the authors designed the adaptive control just for fully actuated underwater robot, and this controller cannot be applied to underactuated systems.

In this chapter, the robust adaptive control will be designed for underactuated vertical dynamics with unknown parameters of hydrodynamic and bounded disturbances. There are three kinds of actuators which are buoyancy engine, moving mass and thrusters. However, the buoyancy engine is used as a two-mode actuator with backward and forward motions for gliding down and up respectively. So that the dynamics has three degrees of

freedom and only two control inputs, which are τ_u and τ_q. An underactuated system like RHUG cannot use the adaptive control for controlling pitch angle and speed without decoupling these dynamics. Therefore, the RHUG dynamics can be only controlled using backstepping technique for pitch and speed control. The robust adaptive controls for pitch angle and speed control will be presented separately in the following sections.

6.2. Adaptive sliding-mode control for pitch motion

The third and fifth equation in (217) can be rewritten as (218) in the pitch control system with two subsystems 1 and 2. Subsystem 1 is the kinematic of pitch motion, which is the pitch velocity and can be measured by the gyro sensor. The second subsystem is the acceleration of pitch angle and can be simplified as a function f_2 and inertia term m_{33}. It is noted that there are 4 state variables which are u, w, q and θ involved in this function.

$$\begin{aligned} &\text{System 1:} && \dot{\theta}=q \\ &\text{System 2:} && m_{33}\dot{q}=f_2\left(\dot{v},v,\eta\right)+\tau_q+\tau_{eq} \end{aligned} \tag{218}$$

where, $m_{33} = I_{yy} - M_{\dot{q}}$; $f_2 = -mz_g\dot{u} + \left(mx_g - M_{\dot{w}}\right)\dot{w} - mz_g qw - Z_{\dot{w}}wu - Z_{\dot{q}}qu + X_{\dot{u}}uw + M_{uu}u^2 + M_{uw}uw + M_{ww}w^2 + M_{www}w^3 - \left(z_gW - z_bB\right)sin\theta - \left(x_gW - x_bB\right)cos\theta.$

The error of this system can be defined as

$$\begin{cases} e_1=\theta-\theta_d \\ e_2=q-q_d \end{cases} \tag{219}$$

The error dynamics $\dot{e}_1$ can be derived as (220) with the presence of the virtual control q_d. To stabilize this error dynamic, the control law for virtual control q_d can be designed as $q_d = \dot{\theta}_d - k_1 e_1$ with positive control gain ($k_1 > 0$).

$$\dot{e}_1=\dot{\theta}-\dot{\theta}_d=q-\dot{\theta}_d=e_2-\dot{\theta}_d+q_d \tag{220}$$

Then, this error dynamics can be derived as $\dot{e}_1 = -k_1 e_1 + e_2$. Therefore, the derivative of the virtual control can be easily shown as (221) in the function of two errors and the desired value of pitch angular acceleration.

$$\dot{q}_d=\ddot{\theta}_d+k_1^2 e_1-k_1 e_2 \tag{221}$$

For direct Lyapunov stability, the Lyapunov candidate is chosen as (223) with three components. The first two terms are error magnitude and the third term is the magnitude of adaptation error. By deriving the derivative of the Lyapunov function, the control law for τ_q can be established as (225) using the adaptation law, error stabilizer, disturbance estimation and sliding mode control. In the practical, the disturbance can be modeled as the zero mean function such as a sinusoidal function or random function.

$$m_{33}\dot{e}_2=m_{33}\dot{q}-m_{33}\dot{q}_d=f_2-m_{33}\dot{q}_d+\tau_q \tag{222}$$

$$V_2=\frac{1}{2}e_1^2+\frac{1}{2}m_{33}e_2^2+\frac{1}{2}\tilde{a}_2 P_2^{-1}\tilde{a}_2 \tag{223}$$

$$\dot{V}_2=-k_1 e_1^2+e_1 e_2+e_2(-Y_2 a_2+\tau_q+\tau_{eq})+\dot{\hat{a}}^T P_2^{-1}\tilde{a}_2 \tag{224}$$

$$\tau_q=Y_2\hat{a}_2-k_2 e_2-e_1-\tau_{eq}-k_{2\Delta}sat(\frac{e_2}{\phi_2}) \tag{225}$$

Here,

$Y_2 a_2 = -f_2 + m_{33}\dot{q}_d$; $\tilde{a}_2 = \hat{a}_2 - a_2$;

$Y_2 = [\dot{u}\ \dot{w}\ qw\ qu\ wu\ u^2\ w^2\ w^3\ sin\theta\ cos\theta\ \dot{q}_d]$;

$a_2 = [(-mz_g)\ (mx_g - M_{\dot{w}})\ (-mz_g)\ (-Z_{\dot{w}} - X_{\dot{u}} + M_{uw})\ (-Z_{\dot{q}})\ (M_{uu})$

$(M_{ww})\ (M_{www})\left(-z_gW + z_bB\right)\left(-x_gW + x_bB\right)\ (-m_{33})]^T$ and $P_2 = I_{11\times 11}$.

The sliding surface is chosen as $s = e_2$ and it is presented in the control law under the saturation function as described in Fig. 52.

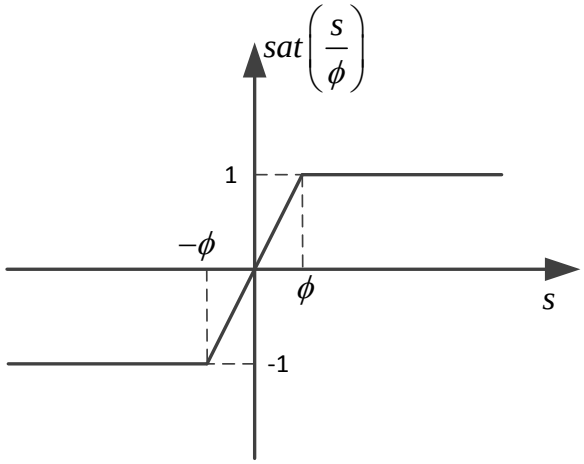

Fig. 52 Saturation function

By choosing the adaption law as $\dot{\hat{a}} = -P_2 Y_2^T e_2$, it will compensate the term $e_2 Y_2 \tilde{a}_2$ in the derivative function of V_2 as (226). The stability can be proved as followings under the condition of $k_{2\Delta} \geq \left|\tau_{eq} - \hat{\tau}_{eq}\right|$ as shown in (227).

$$\dot{V}_2 = -k_1 e_1^2 - k_2 e_2^2 - k_{2\Delta} e_2 sat(\frac{e_2}{\phi_2}) + e_2(\tau_{eq} - \hat{\tau}_{eq}) + e_2 Y_2 \tilde{a}_2 + \dot{a}_2 P_2^{-1} \tilde{a}_2 \tag{226}$$

$$\begin{aligned} \dot{V}_2 &= -k_1 e_1^2 - k_2 e_2^2 - k_{2\Delta} e_2 sat(\frac{e_2}{\phi_2}) + e_2(\tau_{eu} - \hat{\tau}_{eu}) \\ &\leq -k_1 e_1^2 - k_2 e_2^2 - k_{2\Delta}\left|e_2\right| + \left|\tau_{eu} - \hat{\tau}_{eu}\right|\left|e_2\right| \\ &\leq -k_1 e_1^2 - k_2 e_2^2 \quad \text{(N.D)} \end{aligned} \tag{227}$$

6.3. Adaptive sliding-mode control for surge motion

$$\text{System 3: } m_{11}\dot{u} = f_3\left(\dot{v}, v, \eta\right) + \tau_w \sin\theta + \tau_u \tag{228}$$

The surge dynamics can be formulated as (228). Here, $m_{11} = m - X_{\dot{u}}$; $f_3 = -mz_g\dot{q} + mx_g q^2 - (m - Z_{\dot{w}})wq + X_{uu}u^2 + X_{ww}w^2 + X_{uw}uw - (W - B)sin\theta$. The speed control does not include the kinematic equation because the control objective is to make $u \to u_d$ as $t \to \infty$. The function also includes four state variables which are u, w, q and θ. The variables u and w can be measured by DVL sensor, and AHRS sensor can provide the pitch angle θ and pitch angular rate q. The error definition for speed control is e_3 as (229), and the error dynamics can be derived as (230), and then the Lyapunov function for designing control law can be formulated as (231).

$$e_3 = u - u_d \tag{229}$$

$$m_{11}\dot{e}_3 = m_{11}(\dot{u} - \dot{u}_d) = f_3 + \tau_w \sin\theta + \tau_u - m_{11}\dot{u}_d \tag{230}$$

$$V_3 = \frac{1}{2}m_{11}e_3^2 + \frac{1}{2}\tilde{a}_3^T P_3^{-1}\tilde{a}_3 \tag{231}$$

To derive the control law from Lyapunov function, the derivative of V_3 should be derived with the presence of the system dynamic, as shown in (232). By the regressive vector Y_3, $\dot{V}_3$ can be rewritten as (233). Here, $Y_3 a_3 = -(f_3 + \tau_w sin\theta - m_{11}\dot{u}_d)$; $Y_3 = [\dot{q}\ q^2\ wq\ u^2\ w^2\ uw\ sin\theta\ \dot{u}_d]$; $a_3 = [(-mz_g)\ \ (mx_g)\ \ (-m + Z_{\dot{w}})\ \ (X_{uu})\ \ (X_{ww})\ (X_{uw})\ (-B + W)\ (-m_{11})]^T$ and $P_3 = I_{8\times 8}$.

$$\dot{V}_3 = e_3(f_3 + \tau_w \sin\theta - m_{11}\dot{u}_d + \tau_u + \tau_{eu}) + \tilde{a}_3 P_3^{-1}\tilde{a}_3 \tag{232}$$

$$\dot{V}_3 = e_3(-Y_3 a_3 + \tau_u + \tau_{eu}) + \tilde{a}_3 P_3^{-1}\tilde{a}_3 \tag{233}$$

To make $\dot{V}_3$ less than or equal zero, control input τ_u should be designed as (234). The first term is the adaptation result to estimate the unknown nonlinear part, and the second term is added to create the negative term with

speed error. The third term is the estimated magnitude of external disturbance (normally chosen as zero), and the final term is robust action with saturation function for chattering-free sliding mode control.

$$\tau_u = Y_3 \hat{a}_3 - k_3 e_3 - \hat{\tau}_{eu} - k_{3\Delta} sat\left(\frac{e_3}{\phi_3}\right) \tag{234}$$

$$\dot{V}_3 = -k_3 e_3^2 - k_{3\Delta} sat(\frac{e_3}{\phi_3}) e_3 + e_3(\tau_{eu} - \hat{\tau}_{eu}) + e_3 Y_3 \tilde{a}_3 + \dot{a}^T P_3^{-1} \tilde{a}_3 \tag{235}$$

By using the above control law, $\dot{V}_3$ can be rewritten as (235) and it can be easily shown to be stable by (236) using direct Lyapunov theory.

$$\begin{aligned} \dot{V}_3 &= -k_3 e_3^2 - k_{3\Delta} sat(\frac{e_3}{\phi_3}) e_3 + e_3(\tau_{eu} - \hat{\tau}_{eu}) \\ &\le -k_3 e_3^2 - k_{3\Delta} \left|e_3\right| + \left|e_3\right| \left\|\tau_{eu} - \hat{\tau}_{eu}\right| \\ &\le -k_3 e_3^2 \quad \text{(N.D)} \end{aligned} \tag{236}$$

6.4. LOS and PI depth-keeping guidance

The inertial navigation system (INS) can be used to feed the position of the vehicle while the vehicle operates underwater. Therefore, if the INS system is available, the LOS guidance for depth control can be used with two constraints as (237) and (238) for solving the LOS point (x_{los}, z_{los}) in Fig. 53.

$$(z_{los} - z)^2 + (x_{los} - x)^2 = (nL_{pp})^2 \tag{237}$$

$$\frac{z_{los} - z_{k-1}}{x_{los} - x_{k-1}} = \frac{z_k - z_{k-1}}{x_k - x_{k-1}} \tag{238}$$

$$\theta_d = \text{atan2}(z_{los} - z, x_{los} - x) \tag{239}$$

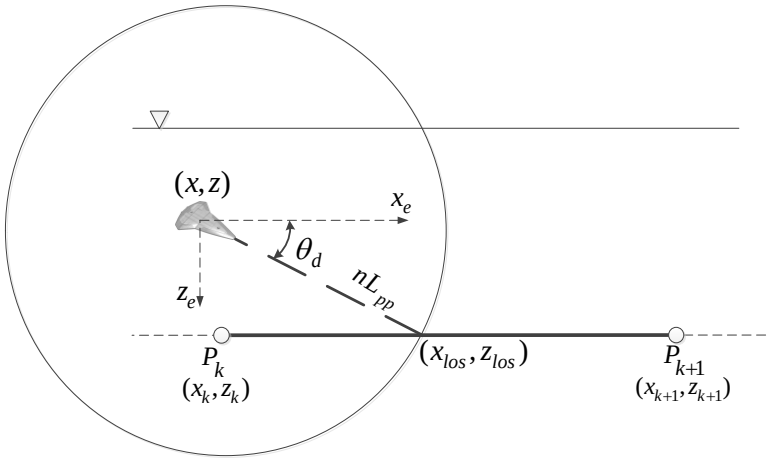

Fig. 53 LOS depth-keeping guidance

And then, the desired pitch angle can be calculated as (239) in the range from $-90°$ to $90°$. In practice, the range can be restricted from $-45°$ to $45°$ for safety purposes.

$$\theta_d = k_p(z_d - z) + k_i \int_{t_0}^{t} (z_d - z)dt \tag{240}$$

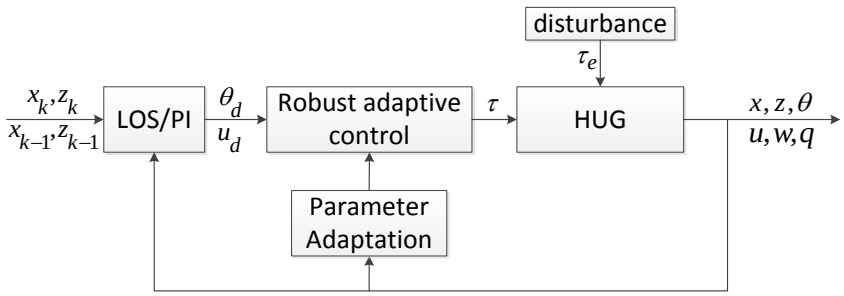

Fig. 54 Scheme for depth keeping control

In the case of lacking the position sensor, the vehicle can use PI-guidance for depth control and only depth information is required in (240) where, k_p is the proportional gain and k_i is the integral gain. To verify the proposed control scheme, the simulation of depth control will be explained in the next subsection.

6.5. Computer simulation

6.5.1 Simulation 1

The gliding motion of RHUG will be simulated using the pitch controller as designed above. RHUG will dive to 200m and switch its motion to ascending toward the surface. The desired pitch angle is assigned at $-30°$ and $30°$ for descending and ascending motion. The hydrodynamic coefficients are obtained from Table 3, and the model parameters are collected in Table 6. Here, R_c is the cylinder radius; L is the RHUG length, which is used to calculate the dimensional hydrodynamic coefficients; L_b is the length of the cylinder. From this parameter, the maximum of the net buoyancy force can be estimated as 20.25N. So that, the saturation of τ_w will be in the range from -20.25N to 20.25N. For the environmental disturbance, $|\tau_e| = [2 \; -1 \; 2]^T$ and $\tau_e = |\tau_e| sin(\frac{t}{2\pi})$.

After modeling the RHUG in 3D design, the center of gravity is estimated by SOLIDWORKS in Fig. 55. The pink coordinate is the inertia tensor. The origin is the center of gravity, and there are three inertia tensor, which are I_{xx}, I_{yy} and I_{zz}. In order to get this result, each component should be weighted and their gravity center is estimated in advance, and then that information will be input in SOLIDWORKS. It is noted that Ox_0 in 3D design is Oy_0 in the simulation, Oy_0 in 3D design is Ox_0 in the simulation, and Oz_0 in 3D design is in opposite direction with Oz_0 in the simulation.

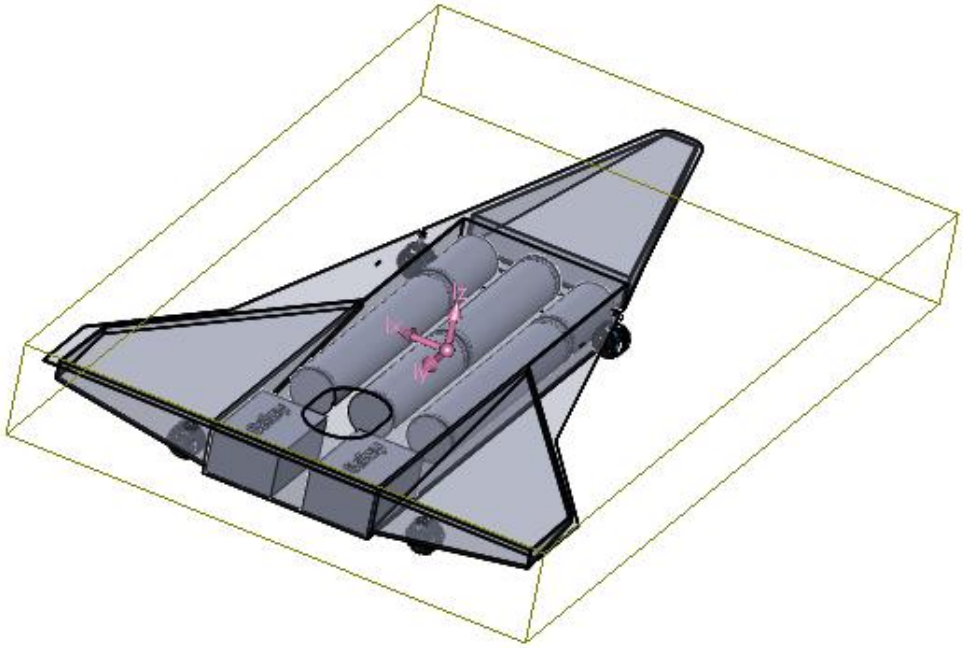

Fig. 55 Center of gravity in 3D design by SOLIDWORKS

Center of Mass (user-overridden): (meters)
X = 0.00
Y = -0.16
Z = 0.01

Principal axes of inertia and principal moments of inertia: (kilograms * square meter
Taken at the center of mass.

Ix = (0.00, 1.00, 0.00)	Px = 0.00
Iy = (-1.00, 0.00, 0.00)	Py = 0.00
Iz = (0.00, 0.00, 1.00)	Pz = 0.00

Moments of inertia: (kilograms * square meters)
Taken at the center of mass and aligned with the output coordinate system.

Lxx = 0.00	Lxy = 0.00	Lxz = 0.00
Lyx = 0.00	Lyy = 0.00	Lyz = 0.00
Lzx = 0.00	Lzy = 0.00	Lzz = 0.00

Moments of inertia: (kilograms * square meters)
Taken at the output coordinate system.

Ixx = 2.67	Ixy = 0.00	Ixz = 0.00
Iyx = 0.00	Iyy = 0.01	Iyz = -0.13
Izx = 0.00	Izy = -0.13	Izz = 2.66

Fig. 56 Moment of inertia in 3D design by SOLIDWORKS

Therefore, moment of inertia I_{yy} is equal to I_{xx} in Fig. 56. In Fig. 55, vector I_{xx} point to the sway direction, so I_{xx} in 3D design is I_{yy} in the simulation. In Fig. 56, the coordinate of center of gravity is $x_g = 0.16m$ and $z_g = -0.01m$. Other parameters of RHUG model can be seen in Table 6.

Table 6 Model parameters

Parameter	Value	Parameter	Value
R_c	0.065 m	x_g	0.16m
L	2.4 m	z_g	-0.01m
m	107 kg	x_b	0m
I_{yy}	2.67 kgm^2	z_b	0m
m_m	3.62 kg	L_b	0.13m

The gliding motion is simulated using the Runge-Kutta 4th method, and the trajectory of one cycle of glide is shown in Fig. 57. The coordinate of RHUG is simulated by the blue line, and the orientation of RHUG is represented by the yellow triangle in Fig. 57. The desired depth for switching to the ascending mode is set at 200m depth.

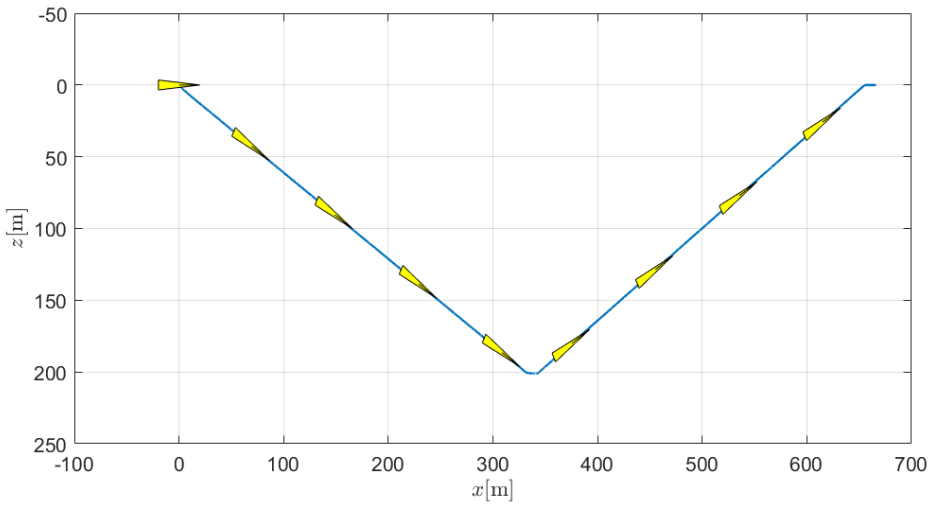

Fig. 57 One cycle of gliding

In the gliding motion, only pitch control is required. The desired pitch is assigned as $-30°$ for descending and $30°$ for ascending. Due to the slow motion of pistons in the buoyancy engine, at the desired depth of 200m, the

desired angle is set at 0°, and when the buoyant condition is positive, it will change to 30° for resurfacing motion. The performance of pitch control is shown in Fig. 58c. The solid blue line is the actual pitch angle, and the red dashed line is the desired pitch angle. It can be seen that at the first time, the desired angle is $-30°$ for gliding down, and when RHUG glides to 200m, the desired angle is changed to $0°$. And then, if the net buoyancy force is negative or $(W - B) < 0$, the desired angle will be set at 30° for gliding up to the sea surface. The pitch control has a good performance despite the presence of the bounded disturbance as described above.

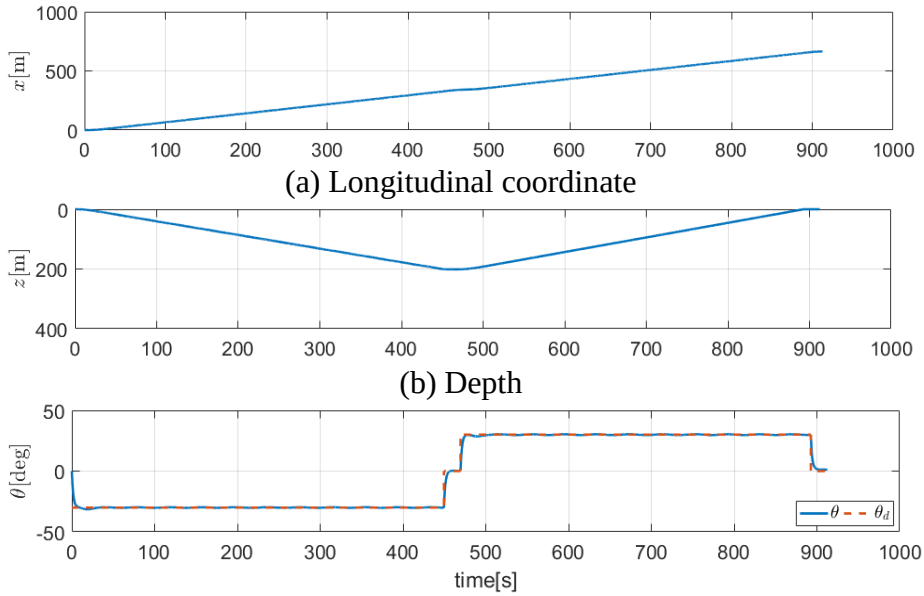

(a) Longitudinal coordinate

(b) Depth

(c) Pitch control

Fig. 58 Pitch control performance

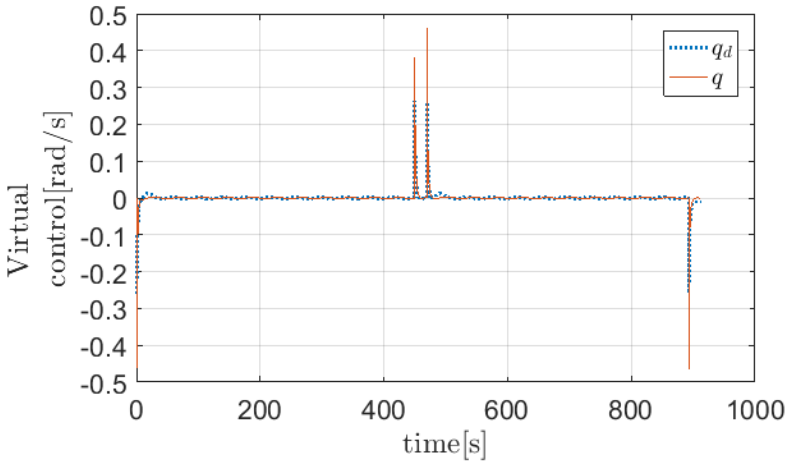

Fig. 59 Virtual control input

In the backstepping technique, it is important to verify the tracking performance of the virtual input q_d. In Fig. 59, the blue dot line represents the designed virtual control input, and the solid red curve is the actual pitch rate. This figure showed that the tracking performance of virtual control has a good tracking in the presence of the external disturbance.

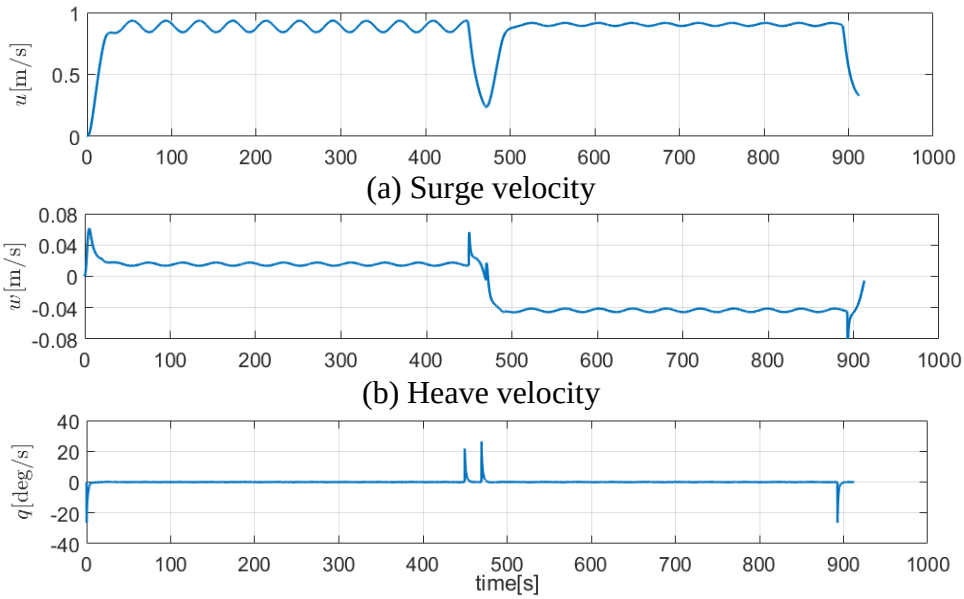

(a) Surge velocity

(b) Heave velocity

(c) Pitch angular rate

Fig. 60 Body-fixed velocities

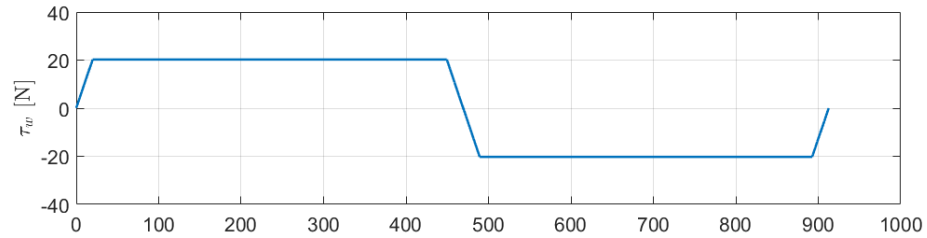

(a) Net buoyancy force

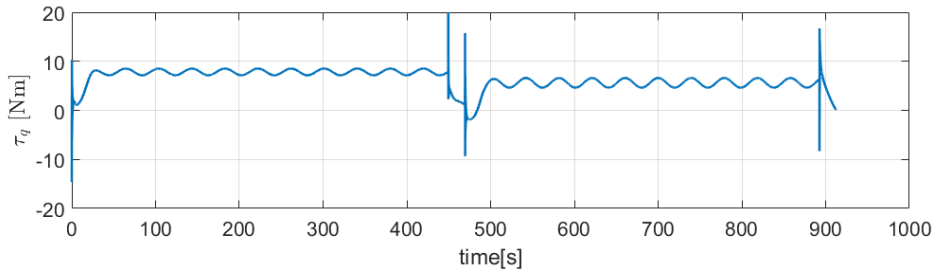

(b) Heave velocity

Fig. 61 Control input

The body-frame velocities of RHUG are presented in Fig. 60. The surge velocities increase near to 1m/s in the descending motion and fall to 0.2m/s at the desired depth and then rise again near to 1m/s in the ascending motion. During the descending time, the heave velocity is positive and has an equilibrium point of around 0.015m/s. It has a negative value in the ascending motion with an equilibrium value of around -0.04m/s. In Fig. 60c, the pitch angular velocity is similar to the red curve in Fig. 59. But in this figure, the unit of pitch rate is degree per second.

The control inputs of the buoyancy engine and moving mass are shown in Fig. 61. The net buoyancy force slowly increases to 20.25N in the descending motion and decreases to -20.25N in the resurfacing motion, as shown in Fig. 61a. The pitch error has the waveform curve and it is under 0.4deg, as shown in Fig. 62.

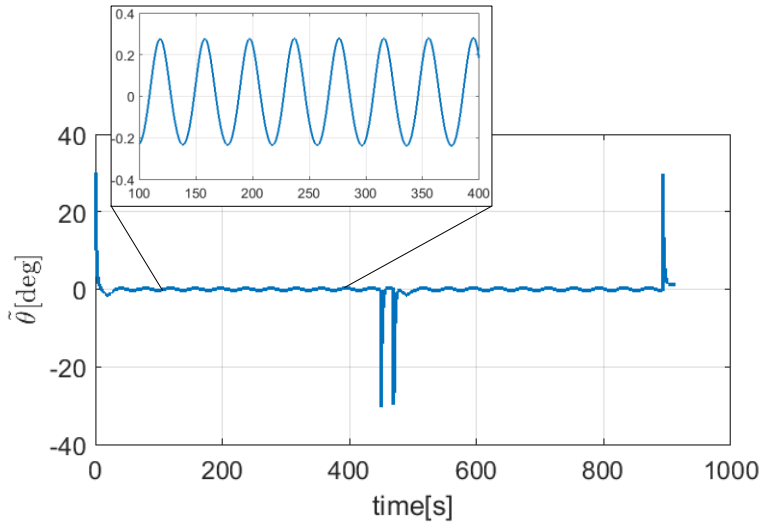

Fig. 62 Pitch control error

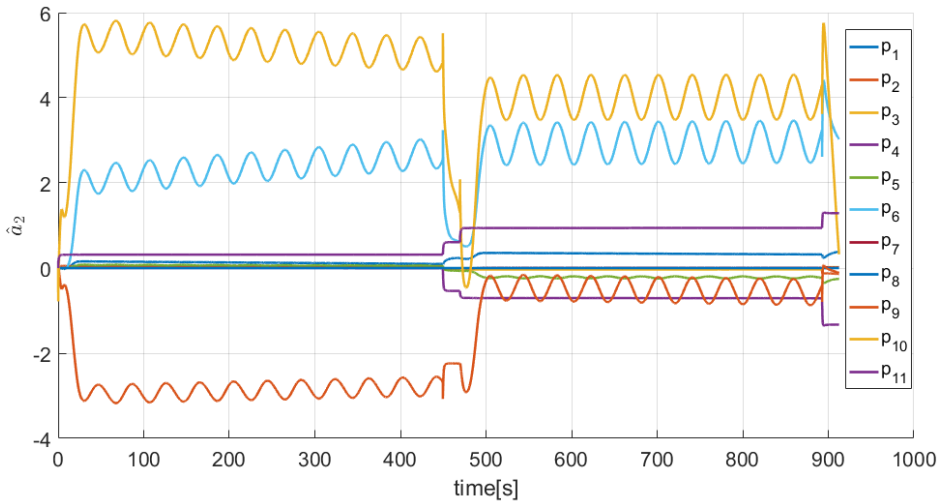

Fig. 63 Parameter adaptation

With the adaptation in Fig. 63, it is shown that the estimated parameters in the 6th, 9th and 10th position of the estimated vector $\hat{a}_2$ have the significant waveform pattern compared to other estimated parameters. The 6th estimated parameter is for M_{uu}, the 9th estimated parameter is for $(-z_g W + z_b B)$, and the 10th estimated parameter is for $(-x_g W + x_b B)$.

6.5.2 Simulation 2

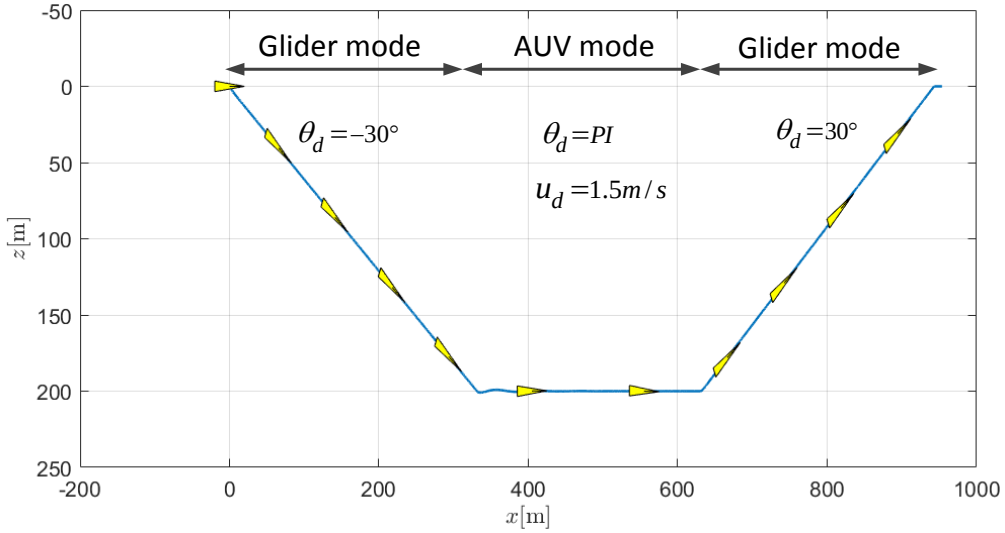

Fig. 64 Depth control performance with uncertainty and disturbance

The depth control of RHUG can be formed in three tasks. The first task is descending motion using the buoyancy engine and moving mass without the thruster force. In this task, the desired pitch angle is set at $-30°$ in Fig. 65. When it glides down to the desired depth, the speed control and PI guidance are the second task. In this simulation, the surge speed is regulated at 1.5m/s, and the desired pitch angle is decided by the PI guidance. It is noted that the net buoyancy force should be neutral to reduce the required force for speed and pitch control in the desired depth. The last task is resurfacing after traveling a certain distance (300m in this simulation in Fig. 64). This task is similar to the first operation, but the desired pitch angle is fixed at $30°$ to glide up. The position of the vehicle is assumed to be unavailable so PI guidance is the suitable choice for this scenario.

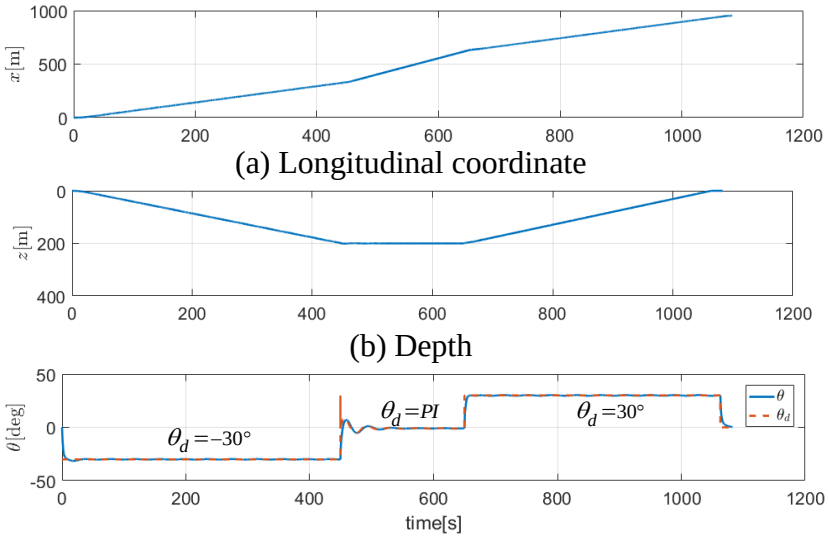

(a) Longitudinal coordinate

(b) Depth

(c) Pitching performance in depth control

Fig. 65 Tracking performance of pitch control

The hydrodynamic coefficients are shown in Table 3 using the CFD method, and it is used for this simulation. The parameters of the model are illustrated in Table 6. For the environmental disturbance, $|\tau_e| = [2 - 1\ 2]^T$ and$\tau_e = |\tau_e| sin(\frac{t}{2\pi})$. And the desired depth for this simulation is still 200m.

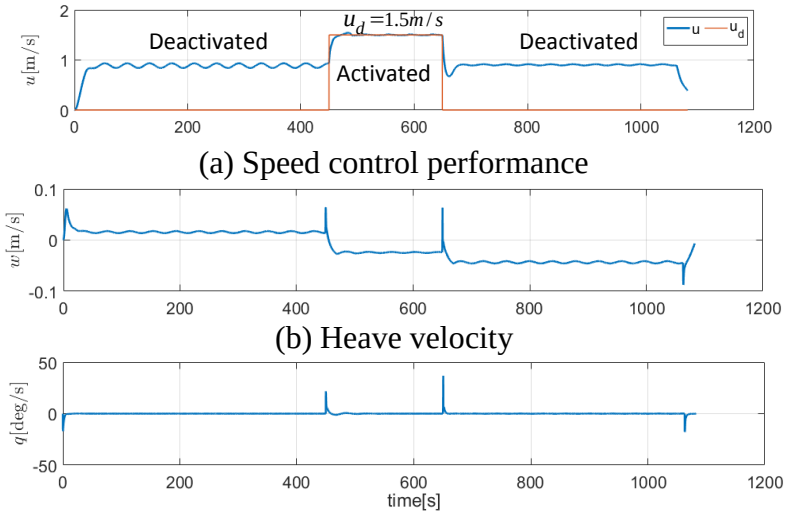

(a) Speed control performance

(b) Heave velocity

(c) Pitch velocity

Fig. 66 Speed control performance

The simulation uses the Runge-Kutta 4th order method for simulating the vertical dynamics of RHUG. From 0s to 450s, the RHUG glides down with $\theta_d = -30°$ as shown in Fig. 65c. When it reaches 200m depth, this vehicle will accomplish longitudinal distance of 330m in Ex axis, as shown in Fig. 65a. In the second task, it will complete the 300m distance at the constant speed of 1.5m/s. The PI guidance will be used to calculate the desired pitch angle following Eq. (240). From 450s to 650s, it moves from 330m to 630m in the Ex axis at the desired depth of 200m. The timer is used to know the distance of the vehicle at 200m, and after a period of 200s, it will get into the third task of ascending. The PI guidance and speed control will be deactivated and the desired pitch angle is set at 30° in Fig. 65c. After reaching the water surface, the vehicle achieves a distance of 943m distance in the longitudinal coordinate.

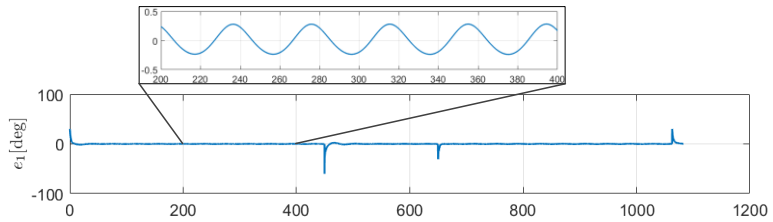

(a) Pitch angle error

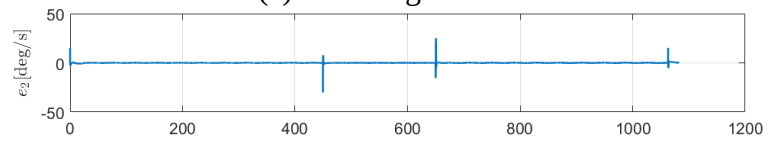

(b) Virtual control error

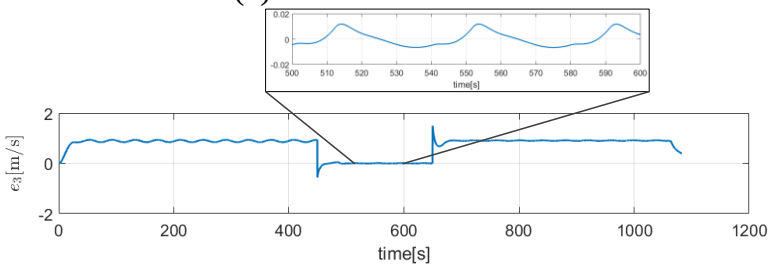

(c) Speed control error in the desired depth

Fig. 67 The tracking errors from 3 sub-controllers

In Fig. 65c, the pitch angle is the blue line, and the desired angle is the red dash line. It can be seen that the actual angle follows the desired angle very well despite the effect of disturbance with less than 0.5° error in Fig. 67a. And in Fig. 66a, the performance of speed control is shown. The blue line is the actual surge speed, and the red line is the desired speed, which is 1.5m/s in the period of the second task. It is shown that the error of speed control is improved and converges to zero at the end of the task. The speed error is less than 0.02m/s and can be seen in Fig. 67c. The behavior of heave and pitch angular velocities are shown in Fig. 66b and Fig. 66c.

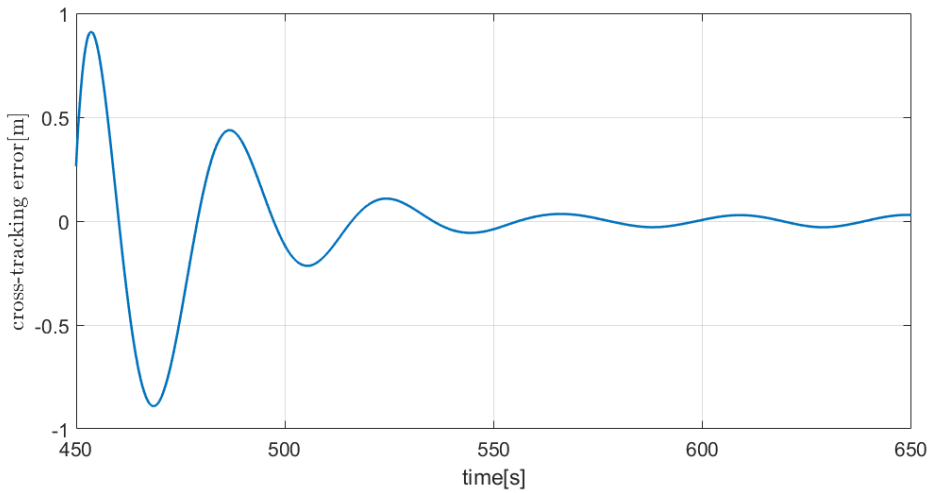

Fig. 68 Cross-tracking error in depth control

In Fig. 68, the depth error with PI guidance is plotted. The guidance gains are adjusted as $k_p = 10$ and $k_i = 0.1$. With the PI guidance, the depth value is only needed for keeping the vehicle at the desired depth. This guidance is very practical, and it also has a good performance with less than 0.1m error in this simulation. Fig. 68 illustrates the zero convergence of the PI guidance from 1m to 0.06m in the cross-tracking error.

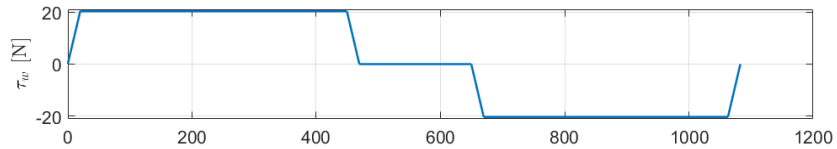

(a) Net buoyancy force

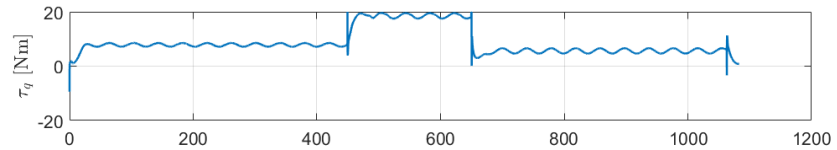

(b) Moment induced by moving mass

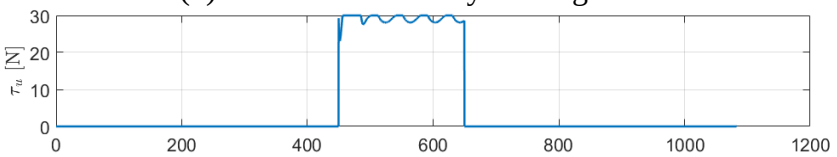

(c) Thruster force during the depth control

Fig. 69 Control inputs from robust adaptive control

In Fig. 69, the control inputs are very smooth, and with these control laws, the required forces are calculated without the knowledge of hydrodynamic coefficients and vehicle parameters. In Fig. 69a, the net buoyancy force is controlled in three different levels for three tasks. Increasing to 20.25N is for descending, falling to 0N is for the cruising task and decreasing to -20.25N is for the ascending motion. The required moment of mass-shifter for pitching control is shown in Fig. 69b. The saturation of this mass-shifter is designed with the range between -20Nm and 20Nm. The control force of the thruster for 1.5m/s speed regulator is under 30N saturation, as shown in Fig. 69c.

There are eleven parameters needed to be estimated for pitch control, and eight parameters required for speed control in Fig. 70 and Fig. 71 respectively.

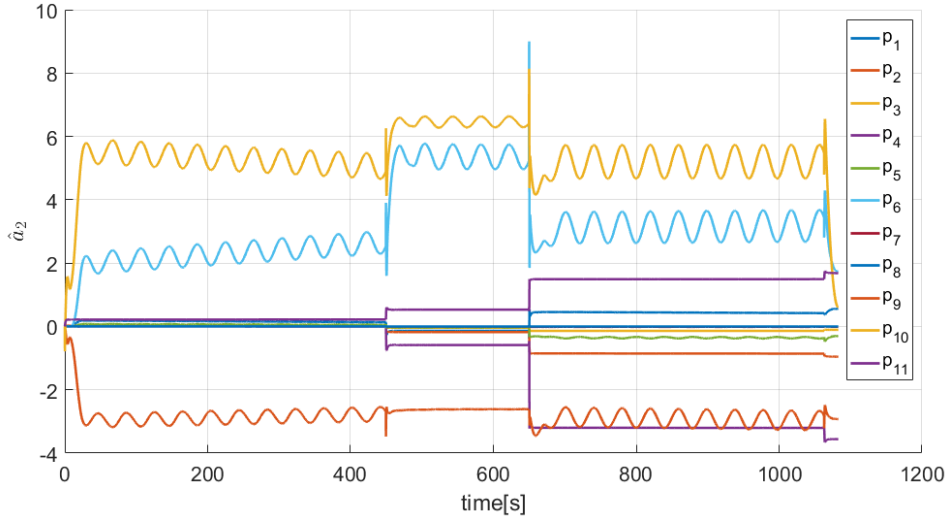

Fig. 70 Pitch parameter adaptation

Here,

$$a_2 = [(-mz_g)\,(mx_g - M_{\dot{w}})\,(-mz_g)\,(-Z_{\dot{w}} - X_{\dot{u}} + M_{uw})\,(-Z_{\dot{q}})\,(M_{uu})\,(M_{ww})\,(M_{www})\,(-z_gW + z_bB)\,(-x_gW + x_bB)\,(-m_{33})]^T;$$

$$a_3 = [(-mz_g)\;\;(mx_g)\;\;(-m + Z_{\dot{w}})\;\;(X_{uu})\;\;(X_{ww})\,(X_{uw})\,(-B + W)\,(-m_{11})]^T.$$

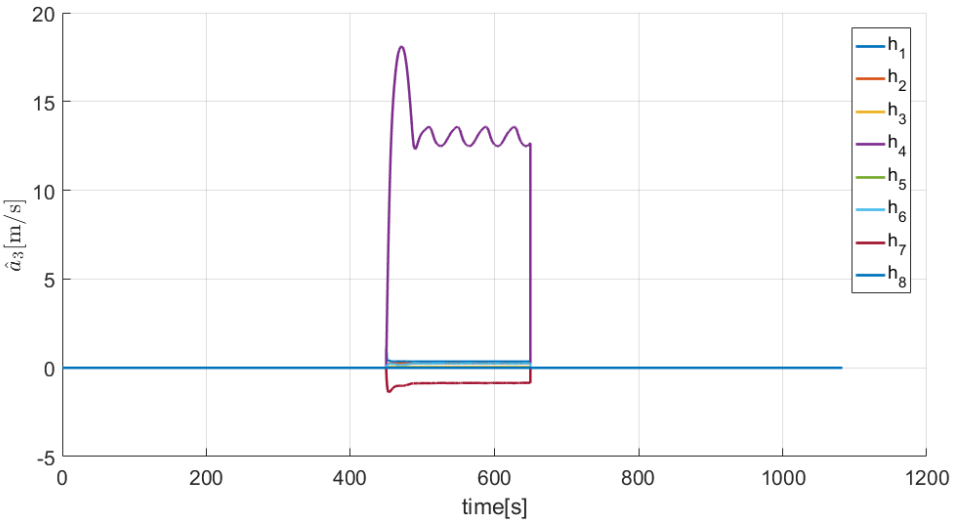

Fig. 71 Speed parameter adaptation

The estimated parameters for M_{uu}, $\left(-z_g W + z_b B\right)$ and $\left(-x_g W + x_b B\right)$ in vector a_2 are sensitive to the environmental disturbance while the estimation of X_{uu} in vector a_3 is adapted with the sinusoidal behavior.

Chapter 7. Conclusion

A new hull design of the hybrid underwater glider with ray shape was proposed for faster gliding speed and longer duration. The model of RHUG was separated into heading dynamics and vertical dynamics. The hardware of RHUG was designed and constructed for the TOT experiments and the sea trials. And the analytical solutions of two dynamics were formulated in the explicit function of time.

To design the time-optimal trajectory, a closed-form solution of the heading dynamics with linear and quadratic damping was formulated. A robust control algorithm with TOT for heading dynamics was simulated with a good tracking performance considering parameter uncertainties and bounded disturbances. For tracking the TOT trajectory, the ST-SMC not only had a small tracking error but also reduced the chattering phenomenon in the control input.

Also, an analytical solution of TOT for heave dynamics using a hybrid actuation of buoyancy and thruster forces was proposed individually. A robust depth control with the proposed TOT was simulated with a good tracking performance in the presence of bounded disturbances.

To implement the TOT and identify the unknown parameters of the developed RHUG, the experiment for tracking the TOT using direct adaptive control was conducted, and it showed a stable tracking performance and a constant convergence of unknown parameters. Moreover, a zero convergence of tracking error using adaptive control was confirmed in the experiment.

The gliding motion and depth control of the RHUG was simulated using the hydrodynamics coefficients from CFD analysis. In the gliding motion, a proposed robust adaptive control for pitch control had a reliable performance

with consideration of unknown parameters and bounded disturbances. And in the simulation of depth control, the robust adaptive control combined with PI guidance had a good performance of tracking the desired depth against unknown parameters and external bounded disturbances.

Reference

[1] B. Claus, Bachmayer, R., & Cooney, L., "Analysis and development of a buoyancy-pitch based depth control algorithm for a hybrid underwater glider," in *IEEE/OES Autonomous Underwater Vehicles*, 2012, pp. 1-6.

[2] D. C. Webb, P. J. Simonetti, and C. P. Jones, "SLOCUM: An underwater glider propelled by environmental energy," *IEEE Journal of oceanic engineering*, vol. 26, pp. 447-452, 2001.

[3] J. Sherman, R. E. Davis, W. Owens, and J. Valdes, "The autonomous underwater glider" Spray"," *IEEE Journal of Oceanic Engineering*, vol. 26, pp. 437-446, 2001.

[4] S. A. Jenkins, D. E. Humphreys, J. Sherman, J. Osse, C. Jones, N. Leonard, J. Graver, R. Bachmayer, T. Clem, and P. Carroll, "Underwater glider system study," 2003.

[5] E. O. Rogers, J. Genderson, W. S. Smith, G. F. Denny, and P. J. Farley, "Underwater acoustic glider," in *IGARSS 2004. 2004 IEEE International Geoscience and Remote Sensing Symposium*, 2004, pp. 2241-2244.

[6] S. Wang, C. Xie, Y. Wang, L. Zhang, W. Jie, and S. J. Hu, "Harvesting of PEM fuel cell heat energy for a thermal engine in an underwater glider," *Journal of power sources*, vol. 169, pp. 338-346, 2007.

[7] A. Alvarez, A. Caffaz, A. Caiti, G. Casalino, L. Gualdesi, A. Turetta, and R. Viviani, "Folaga: A low-cost autonomous underwater vehicle combining glider and AUV capabilities," *Ocean Engineering*, vol. 36, pp. 24-38, 2009.

[8] M. Nakamura, W. Koterayama, M. Inada, K. Marubayashi, T. Hyodo, H. Yoshimura, and Y. Morii, "Disk-type underwater glider for virtual mooring and field experiment," *International Journal of Offshore Polar Engineering*, vol. 19, 2009.

[9] M. Arima, N. Ichihashi, and Y. Miwa, "Modelling and motion simulation of an underwater glider with independently controllable main wings," in *Oceans 2009-Europe*, 2009, pp. 1-6.

[10] N. A. A. Hussain, T. M. Chung, M. R. Arshad, R. Mohd-Mokhtar, and M. Z. Abdullah, "Design of an underwater glider platform for shallow-water applications," *International Journal of Intelligent Defence Support Systems*, vol. 3, pp. 186-206, 2010.

[11] B. Claus, R. Bachmayer, and C. D. Williams, "Development of an auxiliary propulsion module for an autonomous underwater glider,"

Journal of Engineering for the Maritime Environment, pp. 255-266, 2010.

[12] S. Phoemsapthawee, M. Le Boulluec, J.-M. Laurens, and F. o. Deniset, "Numerical Study on Hydrodynamic Behavior of an Underwater Glider," in *International Conference on Offshore Mechanics and Arctic Engineering*, 2011, pp. 521-526.

[13] A. Wolek, J. Burns, C. Woolsey, J. Quenzer, L. Techy, and K. Morgansen, "A maneuverable, pneumatic underwater glider," in *2012 Oceans*, 2012, pp. 1-7.

[14] 박요섭, T. A. L. S.-J. 이신제, T. A. L. Y.-K. 이용국, 정섬규, 장남도, and T. A. L. H.-W. 이하웅, "수중 글라이더를 이용한 동해 횡단 사례 보고," vol. 17, 05/31 2012.

[15] K. Isa, M. R. Arshad, and S. Ishak, "A hybrid-driven underwater glider model, hydrodynamics estimation, and an analysis of the motion control," *Ocean Engineering,* vol. 81, pp. 111-129, 2014.

[16] S. Peng, C. Yang, S. Fan, S. Zhang, P. Wang, and Y. Chen, "Hybrid underwater glider for underwater docking: modeling and performance evaluation," *Marine Technology Society Journal,* pp. 112-124, 2014.

[17] C. Yang, S. Peng, and S. Fan, "Performance and stability analysis for ZJU Glider," *Marine Technology Society Journal,* pp. 88-103, 2014.

[18] F. Liu, Y. Wang, W. Niu, Z. Ma, and Y. Liu, "Hydrodynamic performance analysis and experiments of a hybrid underwater glider with different layout of wings," in *OCEANS 2014 - TAIPEI*, 2014, pp. 1-5.

[19] I. Abbasi, S. S. A. Ali, M. Ovinis, and W. Naeem, "Adaptive identification of underwater glider using U-model for depth and pitch control under hydrodynamic disturbances," *Jurnal Teknologi* pp. 113-118, 2015.

[20] J. Busquets-Mataix, J. V. Busquets-Mataix, and D. Busquets-Mataix, "Combined Gas-Fluid Buoyancy System for Improved Attitude and Maneuverability Control for Application in Underwater Gliders," *IFAC-PapersOnLine,* vol. 48, pp. 281-287, 2015.

[21] C. Sun, B. Song, and P. Wang, "Parametric geometric model and shape optimization of an underwater glider with blended-wing-body," *International Journal of Naval Architecture and Ocean Engineering,* vol. 7, pp. 995-1006, 2015.

[22] S.-K. Jeong, H.-S. Choi, J.-H. Bae, S.-S. You, H. S. Kang, S.-J. Lee, J.-Y. Kim, D.-H. Kim, and Y.-K. Lee, "Design and control of high speed unmanned underwater glider," *INTERNATIONAL JOURNAL*

OF PRECISION ENGINEERING AND MANUFACTURING-GREEN TECHNOLOGY, vol. 3, pp. 273-279, 2016.

[23] M. Y. Javaid, M. Ovinis, F. B. M. Hashim, A. Maimun, Y. M. Ahmed, and B. Ullah, "Effect of wing form on the hydrodynamic characteristics and dynamic stability of an underwater glider," *International Journal of Naval Architecture and Ocean Engineering,* vol. 9, pp. 382-389, 2017.

[24] Y. Wang, Y. Zhang, M. Zhang, Z. Yang, and Z. Wu, "Design and flight performance of hybrid underwater glider with controllable wings," *International Journal of Advanced Robotic Systems,* pp. 1-12, 2017.

[25] B. R. Page, S. Ziaeefard, A. J. Pinar, and N. Mahmoudian, "Highly Maneuverable Low-Cost Underwater Glider: Design and Development," *IEEE Robotics and Automation Letters,* vol. 2, pp. 344-349, 2017.

[26] T. W. O. Putri, U. Latifa, R. Bambang, and E. M. I. Hidayat, "Modelling and Identification of Underwater Glider for Heading Angle Correction," *International Journal of Modeling and Optimization,* vol. 7, pp. 65-69, 2017.

[27] U. Latifa, T. W. O. Putri, B. R. Trilaksono, and E. M. I. Hidayat, "Modelling, identification, and simulation of autonomous underwater glider in longitudinal plane for control purpose," in *2017 2nd International Conference on Control and Robotics Engineering (ICCRE)*, 2017, pp. 140-144.

[28] F. Leccese, M. Cagnetti, S. Giarnetti, E. Petritoli, I. Luisetto, S. Tuti, R. Đurović-Pejčev, T. Đorđević, A. Tomašević, V. Bursić, V. Arenella, P. Gabriele, A. Pecora, L. Maiolo, E. D. Francesco, G. S. Spagnolo, R. Quadarella, L. Bozzi, and C. Formisano, "A Simple Takagi-Sugeno Fuzzy Modelling Case Study for an Underwater Glider Control System," in *2018 IEEE International Workshop on Metrology for the Sea; Learning to Measure Sea Health Parameters (MetroSea)*, 2018, pp. 262-267.

[29] J. Pablo Orozco Muniz and T. Salgado Jimenez, "VBS design and modelling for a coastal underwater glider," in *OCEANS 2018 MTS/IEEE Charleston*, 2018, pp. 1-7.

[30] M. Chyba, N. E. Leonard, and E. D. Sontag, "Time-Optimal Control for Underwater Vehicles," *IFAC Proceedings Volumes,* vol. 33, pp. 117-122, 2000.

[31] M. Chyba, T. Haberkorn, R. N. Smith, and S. K. Choi, "Design and implementation of time efficient trajectories for autonomous underwater vehicles," *Ocean Engineering,* vol. 35, pp. 63-76, 2008.

[32] B. Rhoads, I. Mezić, and A. C. Poje, "Minimum time heading control of underpowered vehicles in time-varying ocean currents," *Ocean Engineering,* vol. 66, pp. 12-31, 2013.
[33] M. B. Loc, H.-S. Choi, S.-S. You, and T. N. Huy, "Time optimal trajectory design for unmanned underwater vehicle," *Ocean Engineering,* vol. 89, pp. 69-81, 2014.
[34] C. A. Woolsey and N. E. Leonard, "Moving mass control for underwater vehicles," in *Proceedings of the 2002 American Control Conference (IEEE Cat. No.CH37301)*, 2002, pp. 2824-2829 vol.4.
[35] K. D. Do, Z. P. Jiang, and J. Pan, "Robust adaptive path following of underactuated ships," *Automatica,* vol. 40, pp. 929-944, 2004.
[36] K. D. Do, J. Pan, and Z. P. Jiang, "Robust and adaptive path following for underactuated autonomous underwater vehicles," *Ocean Engineering,* vol. 31, pp. 1967-1997, 2004.
[37] P. Bhatta and N. E. Leonard, "Nonlinear gliding stability and control for vehicles with hydrodynamic forcing," *Automatica,* vol. 44, pp. 1240-1250, 2008.
[38] L. Lapierre and B. Jouvencel, "Robust Nonlinear Path-Following Control of an AUV," *IEEE Journal of Oceanic Engineering,* vol. 33, pp. 89-102, 2008.
[39] F. Tatone, M. Vaccarini, and S. Longhi, "Modeling and Attitude Control of an Autonomous Underwater Glider," *IFAC Proceedings Volumes,* vol. 42, pp. 217-222, 2009.
[40] K. Asakawa, K. Watari, M. Nakamura, and T. Hyakudome, "Pitch Control Performance of an Underwater Glider for Long-term Virtual Mooring," in *The Twenty-fourth International Ocean and Polar Engineering Conference*, Busan, Korea, 2014, p. 7.
[41] F. Rezazadegan, K. Shojaei, F. Sheikholeslam, and A. Chatraei, "A novel approach to 6-DOF adaptive trajectory tracking control of an AUV in the presence of parameter uncertainties," *Ocean Engineering,* vol. 107, pp. 246-258, 2015.
[42] J. Cao, J. Cao, B. Yao, and L. Lian, "Dynamics and adaptive fuzzy turning control of an underwater glider," in *OCEANS 2015 - Genova*, 2015, pp. 1-7.
[43] K. Asakawa, T. Hyakudome, Y. Ishihara, and M. Nakamura, "Heading-control tests of an underwater glider for virtual mooring," in *OCEANS 2015 - Genova*, 2015, pp. 1-4.
[44] I. Abraham and J. Yi, "Model predictive control of buoyancy propelled autonomous underwater glider," in *2015 American Control Conference (ACC)*, 2015, pp. 1181-1186.
[45] D. Song, L. Yao, Z. Wang, and L. Han, "Pitching Angle Control Method of Underwater Glider Based on Motion Compensation," in

2015 International Conference on Computational Intelligence and Communication Networks (CICN), 2015, pp. 1548-1551.

[46] B. Claus and R. Bachmayer, "Energy optimal depth control for long range underwater vehicles with applications to a hybrid underwater glider," *Journal Autonomous Robots*, vol. 40, pp. 1307-1320, 2016.

[47] M. Mat-Noh, M. R. Arshad, R. Mohd-Mokhtar, and Q. Khan, "Back-stepping integral sliding mode control (BISMC) application in a nonlinear autonomous underwater glider," in *2017 IEEE 7th International Conference on Underwater System Technology: Theory and Applications (USYS)*, 2017, pp. 1-6.

[48] M. Mat-Noh, M. R. Arshad, and R. Mohd-Mokhtar, "Nonlinear control of autonomous underwater glider based on super-twisting sliding mode control (STSMC)," in *2017 7th IEEE International Conference on System Engineering and Technology (ICSET)*, 2017, pp. 71-76.

[49] S. D., G. T., W. H., C. Z., and Z. L., "Pitch angle active disturbance rejection control with model compensation for underwater glider," in *Intelligent Robotics and Applications. ICIRA 2017. Lecture Notes in Computer Science*, 2017.

[50] Z. Huang, Y. Liu, H. Zheng, S. Wang, J. Ma, and Y. Liu, "A self-searching optimal ADRC for the pitch angle control of an underwater thermal glider in the vertical plane motion," *Ocean Engineering*, vol. 159, pp. 98-111, 2018.

[51] Z. Su, M. Zhou, F. Han, Y. Zhu, D. Song, and T. Guo, "Attitude control of underwater glider combined reinforcement learning with active disturbance rejection control," *Journal of Marine Science and Technology*, pp. 1-19, 2018.

[52] H. Sang, Y. Zhou, X. Sun, and S. Yang, "Heading tracking control with an adaptive hybrid control for under actuated underwater glider," *ISA Transactions*, vol. 80, pp. 554-563, 2018.

[53] T. I. Fossen, *Guidance and control of ocean vehicles*. New York: Wiley, 1994.

[54] T200 thruster. Available: https://www.bluerobotics.com/store/thrusters/t100-t200-thrusters/t200-thruster/

[55] J. Yuh and J. Nie, "Application of non-regressor-based adaptive control to underwater robots: experiment," *Computers Electrical Engineering*, vol. 26, pp. 169-179, 2000.

Acknowledgment

First and foremost, I would like to express my sincere thanks to my supervisor, Prof. Hyeung-Sik Choi, for his invaluable advice, guidance, and motivation throughout this research. Furthermore, he always gives me the best of mental and material conditions to help me complete my study and research.

I want to show my gratitude to members of my dissertation committee: Prof. Sam-Sang You, Prof. Joon-Young Kim, Prof. Sung-Wook Lee, and Prof. Jong-Rae Cho for their helpful comments and suggestions to complete this dissertation.

I want to say thank you to all members of KIAL Laboratory and Vietnamese students in KMOU University for all scientific discussions and helps when I studied in KIAL Lab.

Last but not least, I appreciate my fathers, my mothers, my brothers, and especially my wife for their unconditional love, encouragement, and sympathy for me during this journey.

Ngoc-Duc Nguyen

KMOU, Busan, South Korea